

Die approbierte Originalversion dieser Dissertation ist an der Hauptbibliothek der Technischen Universität Wien aufgestellt (<http://www.ub.tuwien.ac.at>).

The approved original version of this thesis is available at the main library of the Vienna University of Technology (<http://www.ub.tuwien.ac.at/englweb/>).

Dissertation



TECHNISCHE
UNIVERSITÄT
WIEN
VIENNA
UNIVERSITY OF
TECHNOLOGY

Aging and Gas Filtration Studies in the ATLAS Transition Radiation Tracker

**ausgeführt zum Zwecke der Erlangung des Doktorgrades der
technischen Wissenschaften unter der Leitung von**

Ao. Univ. Prof. Dr. Herbert Störi

Institut für Allgemeine Physik

**eingereicht an der Technischen Universität Wien
Technisch-Naturwissenschaftliche Fakultät**

von

Dipl.-Ing. Gerald Sprachmann

**Matrikelnummer: 9513102
9103 Diex
Austria**

Wien, Mai 2006

Acknowledgements

I would like to express my sincere thanks to several people who supported me in the development of this thesis. First and foremost, I'm grateful for all the support and motivation of my supervisor from the University of Technology in Vienna, Dr. Herbert Störi. I appreciate his interest in my work, as well as his advice and patience as this thesis evolved. He was always available when I had questions and I especially would like to thank him for his clear, efficient and fast help whenever it was needed. His creative and innovative ideas helped to make this work to a success. He is truly one of the most outstanding and impressive supervisor that I ever worked with.

I am also delighted to acknowledge the ATLAS-TRT Group at CERN, who have dedicated their time, support and assistance to me, making my stay in this group a pleasant experience. I especially would like to thank:

Dr. Fido Dittus, my group supervisor for guiding me through my work, for his support and for always keeping his door open for my questions, requests and problems.

Dr. Serguei Konovalov for kindly supervising my work in the laboratory and for his support throughout my time at CERN. Without his help, advices and ideas this thesis couldn't have been completed.

Dr. Anatoli Romaniouk for some interesting discussions and for the opportunity to work with his team.

Many thanks to Dr. Armin Hansel and his team from the University of Innsbruck (Institut für Ionenphysik), who provided us measurements with the PTR-MS.

This work is supported by the Austrian “Ministerium für Wissenschaft, Bildung und Kultur”.

Abstract

The Transition Radiation Tracker (TRT) is one of three particle tracking detectors of the ATLAS Inner Detector whose goal is to exploit the highly exciting new physics potential at CERN's next accelerator, the so-called Large Hadron Collider (LHC). The TRT consists of 370000 straw proportional tubes of 4 mm diameter with a 30 micron anode wire, which will be operated with a Xe/CO₂/O₂ gas mixture at a high voltage of approximately 1.5 kV. This detector enters a new area that requires it to operate at unprecedented high rates and integrated particle fluxes. Full functionality of the detector over the lifetime (10 years) of the experiment is demanded. Aging of gaseous detectors is a term for the degradation of detector performance during exposure to ionizing radiation. This phenomenon involves very complex physical and chemical processes that are induced by pollution originating from very small amounts of silicon-based substances in some components of the gas system. This work presents a review of previous aging studies and manifestations as well as a short introduction to wire chamber operations. The origin of the aging causing impurities is diverse and includes outgassing from assembly materials, contamination of the detector during the assembly process and the gas system itself. Systematic studies on this topic have been carried out. Techniques for wire deposit and gas analyses, which allow the identification of the origin and the composition of hazardous impurities, are specified. Aging test results from laboratory experiments and from the systematic component validation procedure are summarized and the dependence of wire aging on certain chamber operation parameters discussed. The specific wire deposition mechanisms are extremely complex but a qualitative approach can be obtained from similarities with processes in plasma chemical vapor deposition. Accordingly, the plasma chemical processes and deposition mechanism of organosilicon compounds in an ionizing environment are described in detail. A useful guideline to avoid aging problems in the TRT gas system is provided. In addition a cleanness specification for the detector components and the assembly procedure is detailed. Different gas purification principles (cryogenic distillation, catalytic conversion, adsorption) that will meet the requirements for the TRT gas system are explained. In order to carry out gas purification studies and concentration measurements, a constant organosilicon source has been developed. The concentration level of common polluted gas components could be identified as well as a maximum expectable impurity level in the TRT gas system. The successful adsorption of organosilicon compounds from a carrier gas by a packed bed adsorber has been demonstrated and the adsorption capacity of different adsorbent materials was examined.

Kurzfassung

ATLAS ist ein Universalexperiment für den zukünftigen Large Hadron Collider (LHC) am CERN, welches es ermöglichen wird, in neue Gebiete der Elementarteilchenphysik vorzudringen. Der Übergangsstrahlungsspurdetektor (engl. TRT, Transition Radiation Tracker) ist der äußerste von drei Subdetektoren des ATLAS Inner Detektor. Der TRT besteht aus 370000 Proportionalröhren von 4 mm Durchmesser mit einem dünnem 30 μm Anodendraht. Der Detektor wird mit dem Gasgemisch Xe/CO₂/O₂ bei einer Hochspannung von ungefähr 1500 kV betrieben. Die volle Funktionsfähigkeit des Detektors über die Lebenszeit (10 Jahre) des Experiments ist gefordert. Aging von Gasdetektoren ist ein Begriff unter dem man die Verringerung der Detektorleistung unter dem Einfluss von ionisierender Strahlung versteht. Dieses Phänomen impliziert komplizierte chemische und physikalische Prozesse, welche durch die Verunreinigung von extrem kleinen Mengen an organischen Siliziumverbindungen in einigen Komponenten des Gassystems hervorgerufen werden. Diese Arbeit präsentiert eine Rückschau auf frühere Aging Studien und Manifestationen wie auch eine kurze Einführung in die Arbeitsweise von Drahtkammern. Die Quelle der Aging verursachenden Verunreinigungen ist divers und beinhaltet Ausgasen von Systemkomponenten, Verunreinigung des Detektors während dem Zusammenbau und dem Gassystem selbst. Systematische Studien zu diesem Thema wurden durchgeführt. Weiters sind Techniken zur Analyse der Anodenablagerungen und zur Gasanalyse näher beschrieben. Dies ermöglicht die Bestimmung der Zusammensetzung und der Herkunft der gefährlichen Verunreinigungen. Aging Testergebnisse von Laborexperimenten und von der systematischen Bauteilvalidierung sind zusammengefasst und die Abhängigkeit des Ablagerungsprozesses von speziellen Drahtkammerbetriebsparametern wird diskutiert. Die spezifischen Ablagerungsprozesse auf der Drahtoberfläche sind extrem komplex. Eine qualitative Annäherung kann durch Ähnlichkeiten mit Prozessen in „Plasma Chemical Vapor Deposition“ erzielt werden. Dementsprechend werden die plasmachemischen Prozesse und Ablagerungsmechanismen von organischen Silikonverbindungen in einer ionisierenden Umgebung im Detail beschrieben. Eine nützliche Richtlinie um Aging Probleme im TRT zu vermeiden wurde erstellt. Zusätzlich ist eine Reinheitsspezifikation für die Detektorbauteile und den Zusammenbau des Detektors gegeben. Verschiedene Gasreinigungsprinzipien (cryogenic distillation, catalytic conversion, adsorption), welche die Anforderungen für das TRT Gassystem erfüllen sind beschrieben. Für die Durchführung der Adsorbentests und Konzentrationsmessungen wurde eine konstante Silikonquelle entwickelt. Das Konzentrationsniveau von üblich verunreinigten Bauteilen konnte bestimmt werden, wie auch die maximal zu erwartende Verunreinigung in dem TRT Gas System. Die erfolgreiche Abscheidung von organischen Silikonverbindungen aus dem Trägergas mit Festbettadsorbentien konnte aufgezeigt werden. Zusätzlich wurde die Adsorptionskapazität von verschiedenen Adsorbentien bestimmt.

Contents

1	Introduction	1
1.1	<i>Wire Chambers</i>	1
1.1.1	Ionization Detectors	1
1.1.2	Applications	2
1.1.3	Aging	2
1.2	<i>CERN, ATLAS and the TRT Particle Detector</i>	2
1.2.1	CERN	2
1.2.2	The accelerator complex	3
1.2.3	The Experiments at the LHC	5
1.2.3.1	ATLAS	6
1.2.3.2	CMS	6
1.2.3.3	ALICE	6
1.2.3.4	LHCb	6
1.2.3.5	TOTEM	7
1.2.4	The ATLAS experiment	7
1.2.4.1	The Inner Detector	10
1.2.5	The Transition Radiation Tracker (TRT)	11
1.2.5.1	Choice of Material	16
1.2.5.2	Choice of Gas	17
1.2.5.3	Aging Problems of the TRT	20
1.2.5.4	Etching of Silicon Deposits with CF_4	21
1.3	<i>Previous Aging Studies</i>	21
1.3.1	Introduction	21
1.3.2	Aging Phenomena	22
1.3.3	Anode Aging	23
1.3.4	Cathode Aging	24
1.3.5	Outgassing of Materials	25
2	Wire Chamber Theory	27
2.1	<i>Introduction</i>	27
2.2	<i>Interactions of Particles with Matter</i>	27
2.2.1	Detection of Charged Particles	28
2.2.2	Detection of Photons	29
2.2.3	Drift and Diffusion of Charges in Gases	30
2.3	<i>Measurement of Ionization</i>	33
2.3.1	Ionization Chambers	33
2.3.2	Proportional Counters	34
2.4	<i>Measurements of Position</i>	39
2.4.1	Multiwire Proportional Chamber	39
2.5	<i>Particle Identification</i>	40
2.5.1	Transition Radiation Detectors	40
3	Plasma Chemistry of Organosilicon Compounds	42
3.1	<i>Introduction</i>	42
3.2	<i>Chemical Precursors – Organosilicon Compounds</i>	43
3.3	<i>Thermodynamics, Kinetics and Mass Transport</i>	44
3.4	<i>Gas Phase Reactions forming Intermediate Species</i>	46
3.4.1	Formation of Intermediate Species	46
3.4.2	Plasma Chemical Processes	48

3.5	<i>Deposition Mechanisms</i>	50
4	Technology of Gas Separation	51
4.1	<i>Introduction</i>	51
4.2	<i>Composition and Thermodynamic Data of Impurities</i>	51
4.3	<i>Purification Principles for Volatile Organic Compounds</i>	53
4.3.1	Cryogenic Distillation	53
4.3.2	Catalytic Conversion	53
4.3.3	Adsorption.....	55
4.4	<i>Gas Separation by Adsorption Processes</i>	55
4.4.1	Fundamentals of Adsorption.....	55
4.4.2	Characterization of Adsorbents	56
4.4.3	Adsorption Equilibrium.....	58
4.4.4	Adsorption Kinetics	61
4.4.5	Adsorption Dynamics	62
4.4.6	Mass Balance of Packed Beds	63
4.4.7	Flow Distribution and Pressure Drop in Packed Beds.....	65
4.4.8	Guideline for Dimensioning of Packed Beds	68
4.4.9	Organosilicon Adsorption on Zeolites	69
5	Deposit and Gas Analysis	73
5.1	<i>Deposit Analysis</i>	73
5.2	<i>Gas Analysis</i>	75
5.2.1	Introduction to the PTR-MS Instrument	75
5.2.2	PTR-MS Measurements	78
5.3	<i>Chemical Analysis</i>	82
5.3.1	Introduction to Infrared Spectroscopy.....	82
5.3.2	Instrumentation	82
5.3.3	Sample Preparation	83
5.3.4	Interpretation of IR Spectra.....	84
5.3.5	IR Measurements.....	87
6	Systematic Component Validation Procedure	91
6.1	<i>Optimization of the Aging Test Procedure</i>	91
6.2	<i>Systematic Component Validation</i>	94
6.3	<i>Principles and Guidelines</i>	95
6.3.1	Detector Assembly Procedure	96
7	Concentration Measurements and Filter Development with a constant Si-Source	98
7.1	<i>Constant Silicon Source</i>	98
7.1.1	Introduction	98
7.1.2	HMDS as Representative for Real Impurities	98
7.1.3	Gas Flow through Capillaries.....	99
7.1.4	Test Setup with Constant Silicon Source.....	102
7.2	<i>Concentration Measurements with the Constant Si Source</i>	103
7.3	<i>Filter Studies</i>	105
7.3.1	Catalytic Conversion of Objectionable Impurities Measured with the PTR-MS.....	105
7.3.2	Adsorption Measurements with an Aeronex Standard Filter	108
7.3.3	Adsorption Measurements with Self-Made Filters	111
7.3.3.1	Zeolite Packed Bed Adsorber	112
7.3.3.2	TIMIS Packed Bed Adsorber	114
7.3.4	Summary of the Adsorption Measurements	116
7.4	<i>Maintenance</i>	118
8	Summary	119
9	Conclusions	122

A	Pressure Drop of Aeronex Standard Filters.....	123
B	Filter Assembly in the TRT active Gas System	126
C	Aging Test Station	128
	Bibliography.....	130
	Nomenclature.....	135
	Curriculum Vitae.....	137

List of Figures

Figure 1: The CERN accelerator complex.....	4
Figure 2: Three dimensional cut-away view of the ATLAS detector.....	9
Figure 3: Three dimensional view of the ATLAS Inner Detector.....	11
Figure 4: The Transition Radiation Tracker (TRT) of the ATLAS experiment.....	13
Figure 5: End view of the TRT barrel, which is made.....	13
Figure 6: End-Cap wheel of the TRT.....	14
Figure 7: A multilayer film (left) is used to produce the straw tubes by winding two tapes of film on a precision mandrel (top right). Four carbon fibers strips on the outside reinforce the straw (bottom right) [25].....	15
Figure 8: SEM picture from the wire surface quality control (left) and wire diameter variations (right) [25].....	15
Figure 9: Straw high-voltage and signal connection scheme [25].....	15
Figure 10: Photon absorption length of argon, krypton and xenon.....	18
Figure 11: Electron drift velocity versus energy for the gas mixtures Xe-CO ₂ -O ₂ and Xe-CF ₄ -CO ₂ [26].....	19
Figure 12: Electron drift velocity versus the radial position in the straw for the gas mixtures Xe-CO ₂ -O ₂ and Xe-CF ₄ -CO ₂ [26].....	19
Figure 13: Distance from operating voltage to point of high-voltage breakdown in.....	20
Figure 14: Some examples for wire aging.....	24
Figure 15: Collision cross-section for electrons in argon as a function of electron energy ϵ [37].....	32
Figure 16: Drift velocities for electrons in argon-methane mixtures [37].....	33
Figure 17: Electric field distribution in a straw tube [38].....	35
Figure 18: Temporal and spatial development of an electron avalanche [38].....	37
Figure 19: Characterization of modes of operation of cylindrical gas detectors [38].....	38
Figure 20: Electric field lines in a multiwire proportional.....	40
Figure 21: Illustration of the production of transition radiation at boundaries [34].....	41
Figure 22: Typical electron energy distribution in a plasma [22].....	47
Figure 23: Chemical Structure of PMDS.....	52
Figure 24: Chemical Structure of HMDS.....	52
Figure 25: Vapor Pressure of HMDS calculated with Antoine Parameters.....	52
Figure 26: Fundamental terms of adsorption.....	56
Figure 27: Graphical form of the Langmuir isotherm where $b_3 > b_2 > b_1$ [62].....	60
Figure 28: Adsorption process between gas phase molecules and adsorbent.....	60
Figure 29: Graphical form of the BET isotherm [62].....	61
Figure 30: Mass transfer zone in a packed bed adsorber.....	63
Figure 31: Movement of the MTZ through the packed bed and breakthrough.....	65
Figure 32: Typical radial void fraction distribution in packed beds.....	67
Figure 33: Calculated and measured pressure drop of a zeolite packed bed.....	68
Figure 34: Zeolite Framework Structure [61].....	70
Figure 35: Faujasite unit cell viewed along $\{111\}$ [61].....	71
Figure 36: Faujasite 12-ring viewed along $\{111\}$ [61].....	71
Figure 37: Zeolite Beads [88].....	72
Figure 38: SEM picture of a clean anode wire surface.....	74
Figure 39: SEM picture of an anode wire surface with Si deposits.....	74
Figure 40: EDX spectrum of the wire surface shown in Figure 39.....	75
Figure 41: Principle structure of the PTR-MS with its 3 subsections: ion source, flow drift tube, ion detection system (QMS / SEM) [68].....	77
Figure 42: Mass spectrum of a stainless steel tube at ~ 30 °C.....	80

Figure 43: Mass spectrum of a stainless steel tube with a rotameter attached at initial stages of heating (~60 °C).....	81
Figure 44: Mass spectrum of a stainless steel tube with a rotameter attached after about 20 hours of heating at ~60 °C.....	81
Figure 45: Illustration of a typical FTIR spectrometer [70].....	83
Figure 46: Infrared spectrum of a silicon oil [69].....	86
Figure 47: Infrared spectrum of the Dow Corning grease Molycote 111 [72].....	88
Figure 48: Infrared spectrum of a sample prepared by hexane solubilization of substances present in a stainless steel pipe (reference number #1045) [73].....	89
Figure 49: Infrared spectrum of hexamethyldisiloxane (C ₆ H ₁₈ OSi ₂) [49].....	89
Figure 50: Aging test setup.....	92
Figure 51: Aging rate dependency versus the gas mixtures: Ar-CO ₂ , Ar-CO ₂ -O ₂ , Xe-CO ₂ -O ₂	92
Figure 52: Aging rate dependency versus the gas flow rate in the straw (gas flow velocity).....	93
Figure 53: Aging rate dependency versus the current density per straw.....	93
Figure 54: Aging test with a non-clean rotameter.....	95
Figure 55: Measured and calculated argon flow rate through a 2 μm capillary as a function of the applied pressure.....	101
Figure 56: Measured and calculated argon flow rate through a 5 μm capillary as a function of the applied pressure.....	101
Figure 57: Measured and calculated argon flow rate through a 10 μm capillary as a function of the applied pressure.....	102
Figure 58: Illustration of a test setup with constant silicon source for concentration measurements and filter development studies.....	103
Figure 59: Aging rate at different impurity concentrations produced with a constant HMDS source.....	104
Figure 60: Mass spectrum of a stainless steel tube.....	106
Figure 61: Mass spectrum of a non-clean rotameter.....	107
Figure 62: Mass spectrum with a catalytic converter connected in series between the rotameter outlet and the PTR-MS inlet.....	107
Figure 63: Aging test with an AERONEX standard filter connected in series between a constant HMDS source and an irradiated prototype.....	109
Figure 64: Outline drawing of the AERONEX purifier type CE-35KF-A-4R [86].....	110
Figure 65: Breakthrough curves for a complex gas mixture with a zeolite Na-ZSM-5/180 packed bed adsorber – LEFT: mixture without water, RIGHT: mixture with water [87].....	110
Figure 66: Aging test with a self-made zeolite filter connected in series between a constant HMDS source and an irradiated prototype.....	114
Figure 67: Aging test with a Self-Made TIMIS filter connected in series between a constant HMDS source and an irradiated prototype.....	116
Figure 68: Press drop curve for the Aeronex Standard Filter type CE-35KF-A-4R with 1 slpm maximum flow rate [86].....	123
Figure 69: Press drop curve for the Aeronex Standard Filter type CE-500KF-A-4R with 60 slpm maximum flow rate [86].....	124
Figure 70: Press drop curve for the Aeronex Standard Filter type CE-2500KF-A-4R with 300 slpm maximum flow rate [86].....	124
Figure 71: Press drop curve for the Aeronex Standard Filter type CE-10MF-A-8Y with 1000 slpm maximum flow rate [86].....	125
Figure 72: TRT active gas system overview [91].....	127
Figure 73: TRT active gas system – piping and instrumentation diagram of the purification module [91].....	127
Figure 74: Straw prototype with three TRT straws connected in parallel.....	128
Figure 75: Straw prototype adjustment in the aging test station.....	129
Figure 76: Aging Test Station.....	129

List of Tables

Table 1: Some selected machine and beam parameters.....	5
Table 2: G-Values from plastics irradiated at 20 °C in air.....	17
Table 3: Partial list of materials tested for outgassing. For a few substances.....	26
Table 4: Thermal velocity u , diffusion coefficient D^+ , mobility μ^+ and the mean free path λ	32
Table 5: Dissociation and ionization energies for some selected gases [22].....	47
Table 6: Some selected TRT gas system parameters.....	52
Table 7: Thermodynamic data of some organosilicon compounds.....	53
Table 8: Minimum temperatures for initiation.....	54
Table 9: Atlas of zeolite framework types [61].....	70
Table 10: Natural isotopic abundances of Si and C.....	77
Table 11: Proton affinities of various volatile organic compounds [63].....	78
Table 12: Detailed absorption table of bonds in organosilicon molecules [70].....	87
Table 13: Chemical composition of the Dow Corning grease Molycote 111.....	90
Table 14: Recommendations for materials to be used in the TRT detector and gas systems.....	96
Table 15: Chemical composition of the grease Molycote 111 and the adhesive/sealant RTV 3145.....	99
Table 16: HMDS concentration levels in the main gas line for different flow rates (capillary of 5 cm length and 2 μm diameter, 1 bar argon over-pressure in vessel, 20 °C).....	105
Table 17: Operating parameters of a constant HMDS source for adsorption measurements with an AERONEX purifier type CE-35KF-A-4R.....	110
Table 18: Adsorbent parameters for the AERONEX purifier type CE-35KF-A-4R.....	111
Table 19: Specification table for the AERONEX purifier type CE-35KF-A-4R [86].....	111
Table 20: Examples for flow rates and prices of AERONEX atmospheric pas purifiers [86].....	111
Table 21: Parameters of the self-made zeolite packed bed adsorber.....	112
Table 22: Operating parameters of a constant HMDS source for adsorption measurements with a zeolite packed bed adsorber.....	113
Table 23: Parameters of the self-made TIMIS packed bed adsorber.....	115
Table 24: Operating parameters of a constant HMDS source for adsorption measurements with a TIMIS packed bed adsorber.....	116
Table 25: Summary of the adsorption measurements.....	117
Table 26: Parameters of a zeolite UY8 purifier for the TRT gas system.....	117

1 Introduction

1.1 Wire Chambers

1.1.1 Ionization Detectors

Ionization detectors were the first devices developed for radiation detection. These instruments are based on the direct collection of charged particles (electrons and ions) produced in a gas by passing radiation. The first three basic types of detectors were the ionization chamber, the proportional counter and the Geiger-Mueller counter. These detectors are actually the same device working under different operating parameters and therefore exploiting different phenomena. The basic structure consists of a wire carrying high voltage that crosses through a metal tube whose walls are held at ground potential. Any ionizing particle that passes through the tube causes the flow of a current. This allows it to count particles and in the case of a proportional counter to determine their energy.

For high energy physics experiments it is necessary to designate a particles path. Until the 1970's, the tracking devices were optical and bubble chambers, for example, were used for this purpose in the way that photographs were made and printed. Therefore, an all-electronic device was desired and a breakthrough occurred in 1968 with the invention of the multiwire proportional chamber (MWPC) by Georges Charpak. This is a chamber with many parallel wires arranged as a grid whereby each is acting as an independent proportional counter. If the chamber is put into a homogeneous magnetic field, so that charged particles are led into spiral paths due to the Lorentz force, the direction of the curves can be determined and thereby the particles charge.

The Transition Radiation Tracker (TRT) of the ATLAS experiment at CERN is a MWPC that consists of an array of single proportional counters, where each anode wire is placed in a cylindrical tube which functions as the cathode. The tube is flushed with the gas mixture $Xe/CO_2/O_2$ and a positive voltage, relative to the tube wall, is applied to the anode wire. When a sufficiently energetic charged particle passes through the chamber, it ionizes some of the gas molecules along its path, leaving a thin ionization trail (particle track). The electrons freed by this ionization drift along the electric field lines towards the anode and are multiplied in an avalanche process close to the wire due to the high field ($E \sim 1/r$). Movement of ions and electrons induces a current in the wire, which is read out by an amplifier. Since the velocity of drifting electrons is known, the measured time of drift determines the position of the track relative to the wire. From such measurements on many wires, the track of the detected particle can be completely reconstructed.

1.1.2 Applications

Wire chambers are detectors that were developed for charged particle detection and tracking. The principle of the MWPC was quickly adopted in high energy physics and stimulated a new generation of physics experiments. The main advantage of a MWPC is that large surface areas can be covered economically. Therefore it has been selected for some detector parts of the ATLAS experiment at CERN like the TRT and the Muon Spectrometer.

Since they were invented, other applications such as X-ray imaging devices in diverse fields as astrophysics, crystallography, medicine, etc. have been found.

1.1.3 Aging

Since the introduction of MWPC and their wide use in experiments at high rates, radiation induced degradation could be observed. The study of the complications limiting their lifetime is of high importance because wire chambers are highly sophisticated and expensive instruments. The degradation problems may be loss of gain, reduction of plateau, loss of energy resolution, excessive currents, self-sustained current discharge, sparking, etc. These effects can be caused by coating or other degradation of the cathode and anode surfaces and are combined under the common term *aging*. In this work, aging refers to a decrease of the gas gain due the formation of anode wire surface deposits from impurities in the gas phase. These deposits are the result of chemical reactions occurring in the avalanche plasma near the anode wire. The origin and the composition of the impurities are diverse and include outgassing from assembly materials, contamination of the detector during the assembly process and the gas system itself. Wire chamber lifetime is extremely sensitive to the nature and purity of the working gas mixture. Different additives, trace contaminants and materials used in contact with the gas can have dramatic impacts on the lifetime. A set of general guidelines on how to build and operate gaseous detectors capable to withstand the radiation fluxes over a longer period of time are given in the literature. However, all these methods are not capable of totally preventing the aging process.

1.2 CERN, ATLAS and the TRT Particle Detector

1.2.1 CERN

CERN is the *Organisation Européenne pour la Recherche Nucléaire* (European Organization for Nuclear Research), the world's largest particle physics laboratory situated in Geneva [1]. The convention establishing it was signed on 29 September 1954. From the original 12 signatories of the CERN convention, membership has grown to the present 20 member states. Its main function is to provide the particle accelerators needed

for high energy physics research and numerous experiments have been constructed at CERN by international collaborations to make use of them.

CERN currently employs about 3000 people full-time next to some 6500 visiting scientists and engineers (representing 500 universities and 80 nationalities), about half of the world's particle physics community, work on experiments conducted at CERN. Several important achievements in particle physics have been made using experiments at CERN. These include, but are not limited to:

- The discovery of neutral currents in 1973 at the Gargamelle bubble chamber.
- The discovery of W and Z bosons in 1983 by the UA1 and UA2 experiments.

The 1984 Nobel prize in physics was awarded to Carlo Rubbia and Simon van der Meer for the latter.

The 1992 Nobel prize in physics was awarded to Georges Charpak for his invention and development of particle detectors, in particular the multiwire proportional chamber.

1.2.2 The accelerator complex

The CERN accelerator complex [2] has six main accelerators (see Figure 1):

- Two linear accelerators generating low energy particles for injection into the Proton Synchrotron. One is for protons and the other for heavy ions. These are known as *Linac2* and *Linac3* respectively.
- The *PS Booster* (PSB), which increases the energy of particles generated by the linear accelerators before they are transferred to the other accelerators.
- The 28 GeV *Proton Synchrotron* (PS) built 1959.
- The *Super Proton Synchrotron* (SPS), a circular accelerator with a diameter of 2 kilometers built in a tunnel, which started operation in 1971. Originally it had an energy of 300 GeV which has been upgraded several times. As well as having its own beamlines for fixed-target experiments, it has been operated as a proton-antiproton collider, and for accelerating high energy electrons and positrons which were injected into the *Large Electron Positron* (LEP) collider.
- The *Isotope Separator OnLine DEvice* (ISOLDE) first commissioned in 1967, which was used to study unstable nuclei. Particles are initially accelerated in the PS Booster before entering ISOLDE

The main activities at CERN are currently directed towards the construction of a proton-proton collider working with two counter-rotating beams of protons accelerated to energies of 7 TeV: the *Large Hadron Collider* (LHC) project. The expected start of the LHC project is in 2007. This will use the 27 km circumference circular tunnel previously occupied by LEP which was closed down in November 2000, and the PS/SPS complex to pre-accelerate protons which will be injected into it (see Figure 1). The tunnel is located 100 meters underground, in the region between the Geneva airport and the nearby Jura mountains. Huge efforts are being made also towards the installation of the five experiments CMS, ATLAS, LHCb, TOTEM and ALICE which will be running on the

LHC. Each of them will study particle collisions under a different point of view, and with different technologies (see chapter 1.2.3). The construction of these experiments needs an extraordinary engineering effort. The experiments performed with the LHC will generate vast quantities of computer data, which CERN will stream to laboratories around the world for distributed processing. This will enable scientists to explore an energy regime that is presumed to have existed in the universe 10^{-12} seconds after the big bang (“Electroweak Epoch”) when its temperature was still in the order of 10^{16} Kelvin. More details on design and construction of the LHC can be found in [3] and Table 1 summarizes a few machine and beam related data.

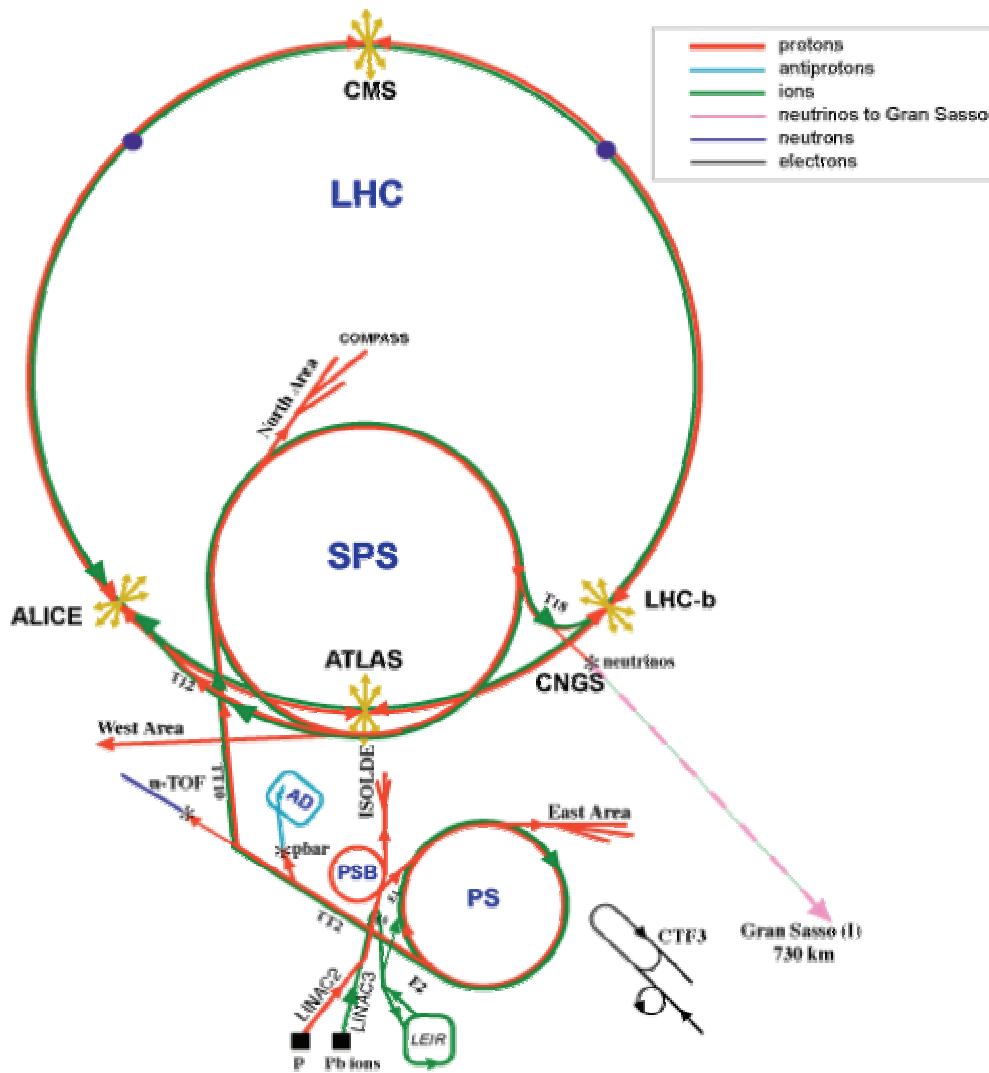


Figure 1: The CERN accelerator complex

Table 1: Some selected machine and beam parameters

Proton energy [TeV]	7
Injection energy [GeV]	450
Dipole field [T]	8.4
Current at nominal field [A]	11850
Luminosity [$\text{cm}^{-2}\text{s}^{-1}$]	10^{34}
Bunch spacing [ns]	25
Particles per bunch [-]	10^{11}
Number of bunches [-]	2808
Bunch length (rms) [cm]	7.5
Inelastic cross-section [mb]	60
Total cross-section [mb]	100
Events per bunch crossing [-]	19
Stored beam energy [MJ]	362
Energy loss per turn [keV]	6.7
Synchrotron radiation power per ring [kw]	3.6

1.2.3 The Experiments at the LHC

The LHC hosts four major experiments, the two large multi-purpose detectors ATLAS and CMS, the heavy-ion experiment ALICE and the B-Physics single-arm spectrometer LHCb. Additionally a small experiment named TOTEM is placed in the region of CMS. While ATLAS and CMS are designed to cover a wide range of physics of the Standard Model and beyond, ALICE, LHCb and TOTEM are rather specialized gaining the ability to optimize the system for their dedicated research area. Detailed information about the Standard Model can be found in [4].

The different experiments along the LHC aim to answer the following questions:

- What is mass?
- What is the origin of mass of particles? (In particular, does the Higgs Boson exist?)
- What is the origin of mass of baryons? (By creating the quark-gluon plasma one will test the non-perturbative origin of a large fraction of the mass of the universe.)
- Why do elementary particles have different masses? (I.e., do particles interact with a Higgs field?)
- 95 % of the mass of the universe is not made of matter as we know it. What is it? (I.e. what is dark matter, dark energy?)
- Do supersymmetric particles exist?
- Are there extra dimensions, as predicted by various models inspired by string theory, and can we "see" them?
- Are there additional violations of the symmetry between matter and antimatter?

1.2.3.1 ATLAS

For a detailed technical description of the ATLAS detector see chapter 1.2.4.

1.2.3.2 CMS

The *Compact Muon Solenoid* (CMS) detector [5] represents one of the general-purpose detectors at CERN. As the name suggests, it relies to a rather compact design (compared to ATLAS) with a large superconducting solenoid magnet generating a 4 T magnetic field. The completed detector will be cylindrical, 21 meters long and 16 meters in diameter, and weigh approximately 12500 tons.

The main goals of the experiment are:

- the discovery of the Higgs boson
- to look for evidence of supersymmetry
- to be able to study aspects of heavy ion collisions

The main highlights of the detector are:

- its relatively small size
- the powerful solenoid
- its optimization for tracking muons

1.2.3.3 ALICE

ALICE, is the acronym for *A Large Ion Collider Experiment* [3]. The objectives of the experiment are to study the physics of strongly interacting matter at extreme energy densities, where the formation of a new phase of matter, the *Quark-Gluon Plasma* (QGP), is expected. Apart from proton-proton collisions ALICE utilizes lead-lead collisions of more than 1 PeV center-of-mass energy. The main challenge of heavy-ion physics is recording the enormous number of particles which emerge from the collisions. At LHC energies, about 50000 particles are produced in each collision. A large fraction of these must be tracked and identified to emerge a clear picture and identify key signals, pointing to different stages in the evolution from ordinary matter to QGP and back again.

1.2.3.4 LHCb

The *Large Hadron Collider beauty* (LHCb) is a special B-physics experiment [6], particularly aimed at measuring the parameters of CP violation in the interactions of B-hadrons. The design of the LHCb is optimized to exploit the B-physics potential of the LHC. It is a single arm forward spectrometer with a polar angular coverage from 10 mrad to 300 mrad in the horizontal and 250 mrad in the vertical plane. The asymmetry between the horizontal and vertical plane is determined by a large dipole magnet with the main component in the vertical direction.

The vertex detector is built around the proton interaction region. It is used to measure the particle trajectories close to the interaction point in order to precisely separate primary and secondary vertices, e.g. for b-tagging.

Directly after the vertex detector RICH-1 (a Ring Imaging Cherenkov detector) is located. It is used for particle identification of low-momentum tracks.

The main tracking system is partly placed in the dipole magnet. It is used to reconstruct the trajectories of charged particles and to measure their momenta.

Following the tracking system is RICH-2. It allows the identification of the particle type of high-momentum tracks.

The electromagnetic and hadronic calorimeters provide measurement of the energy of electrons, photons and hadrons. These measurements are used as trigger level to identify high- p_T particles.

The muon system is used to trigger on muons in the events.

1.2.3.5 TOTEM

The *Total Cross Section, Elastic Scattering & Diffraction Dissociation* (TOTEM) [7] experiment with its detectors in the forward region of CMS and the Roman Pots (RP) [32] along the beam line will determine the total pp cross-section via the optical theorem by measuring both the elastic cross-section and the total inelastic rate. The RP are special beam insertions which allow to bring the detectors very close to the beam without interfering with the primary vacuum of the machine. Its task is to detect protons with scattering angles for a few μrad . Each RP station is made of two units separated by 2.5 - 4 m which are equipped with one horizontal and two vertical pots. The pot consists of a vacuum chamber with 10 silicon detectors.

TOTEM will have dedicated runs with special high-beta beam optics and a reduced number of proton bunches resulting in a low effective luminosity between $1.6 \cdot 10^{28} \text{ cm}^{-2} \text{ s}^{-1}$ and $2.4 \cdot 10^{29} \text{ cm}^{-2} \text{ s}^{-1}$. In these special conditions also an absolute luminosity measurement will be made, allowing the calibration of the CMS luminosity monitors needed at higher luminosities. The acceptance of more than 90 % of all leading protons in the RP system, together with CMS's central and TOTEM's forward detectors extending to a maximum rapidity of 6.5 [33], makes the combined CMS+TOTEM experiment a unique instrument for exploring diffractive processes.

1.2.4 The ATLAS experiment

A Toroidal LHC Apparatus (ATLAS) [8] is a general-purpose experiment for recording proton-proton collisions at LHC. The detector design has been optimized to cover the largest possible range of LHC physics: searches for Higgs bosons and alternative schemes for the spontaneous symmetry-breaking mechanism; searches for supersymmetric particles, new gauge bosons, leptoquarks, and quark and lepton compositeness indicating extensions to the Standard Model [4] and new physics beyond it; studies of the origin of CP violation via high-precision measurements of CP-violating B-decays; high-precision measurements of the third quark family such as the top-quark

mass and decay properties, rare decays of B-hadrons, spectroscopy of rare B-hadrons, and B_s^0 -mixing.

The requirements [9] for the ATLAS detector can be summarized as:

- very good electromagnetic calorimetry for electron and photon identification and measurements, complemented by hermetic jet and missing E_T -calorimetry
- efficient tracking at high luminosity for momentum measurements, for b-quark tagging, and for enhanced electron and photon identification
- τ and heavy-flavour vertexing and reconstruction capability of some B-decay final states at lower luminosity
- stand-alone, high-precision, muon-momentum measurements up to the highest luminosity, and very low p_T trigger capability at lower luminosity.

Following this design considerations the ATLAS detector is being constructed as shown in Figure 2. The ATLAS detector consists of following four major components:

- Inner Detector – measures the momentum of each charged particle
- Calorimeters – measures the energies carried by the particles
- Muon Spectrometer – identifies and measures muons which are not stopped in the inner detector and the calorimeters
- Magnet System – bending charged particles for momentum measurements

The interactions in the ATLAS detectors will create an enormous dataflow which is handled by:

- the trigger system – selecting 100 interesting events per second out of 1000 million others
- the data acquisition system – channeling the data from the detectors to the storage
- the computing system – analyzing 1000 million events recorded per year

In the following section only the inner detector will be described in more detail. A complete characterization of the ATLAS detector can be found in [8] and [9].

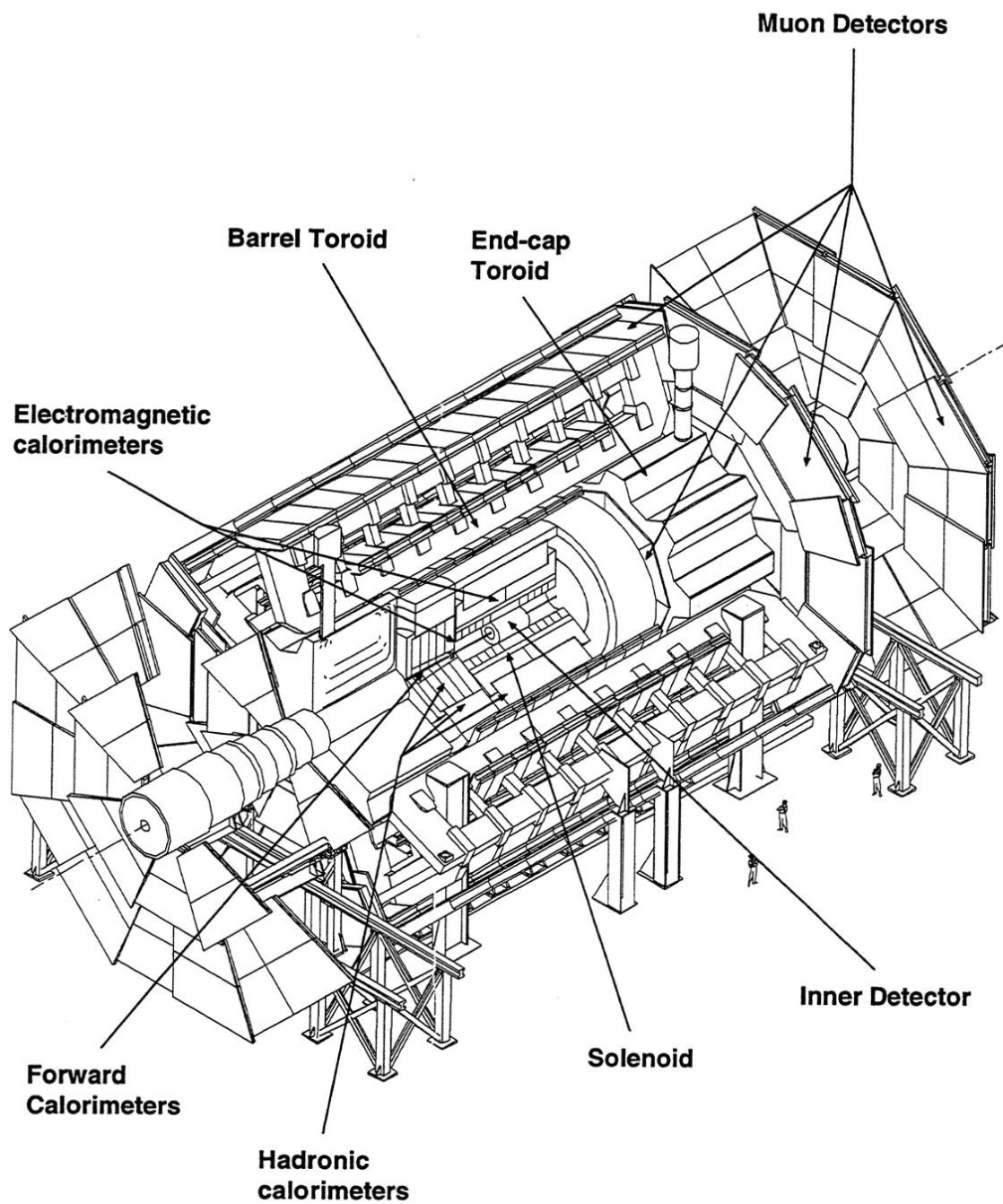


Figure 2: Three dimensional cut-away view of the ATLAS detector

1.2.4.1 The Inner Detector

The purpose of the inner detector is to perform tracking over the rapidity range $|\eta| < 2.5$. The detector begins a few centimeters from the proton beam axis - extends to a radius of 1.2 meters, and is 7 meters in length along the beam pipe. Its basic function is to track charged particles by detecting their interaction with material at discrete points, revealing detailed information about the type of particle and its momentum. The magnetic field surrounding the entire inner detector causes charged particles to curve; the direction of the curve reveals a particles charge and the degree of curvature reveals its momentum. A solenoid magnet provides a 2 T magnetic field. The layout of the inner detector is shown in Figure 3.

The inner detector is divided into the three subdetector systems *Pixel Detector* (PD), *Transition Radiation Tracker* (TRT) and the *Semiconductor Tracker* (SCT) which are described briefly below.

The Pixel Detector

The Pixel Detector (PD) is the closest detector to the collision point. It is designed to provide a very high-granularity and a high precision set of measurements as close to the interaction point as possible. The system provides three precision measurements over the full acceptance, and mostly determines the impact parameter resolution and the ability of the inner detector to find short-lived particles such as B-hadrons and τ leptons.

The Semiconductor Tracker

The Semiconductor Tracker (SCT) is the middle component of the inner detector. It is similar in concept and function to the PD but with long, narrow strips rather than small pixels, making coverage of a larger area practical. The system is designed to provide eight precision measurements per track in the intermediate radial range, contributing the measurement of momentum, impact parameter and vertex position, as well as providing good pattern recognition by use of high granularity. The system is an order of magnitude larger in surface than previous generations of silicon microstrip detectors, and in addition must face radiation levels which will alter the fundamental characteristics of the silicon wafers themselves.

Both the PD and SCT systems require a very high dimensional stability, cold operation of the detectors and the removal of the heat generated by the electronics and the detector leakage current. The structures are therefore designed with materials with extremely low thermal expansion coefficients.

The Transition Radiation Tracker

The Transition Radiation Tracker (TRT) is the outermost component of the inner detector. It contains straws with four millimeters in diameter and up to 144 centimeters long. They are arranged axially in the central barrel and radially in the two endcaps. The total number of straws is about 370000. Straw detectors are used to cover larger radii because it becomes too expensive to cover the large areas required with silicon strip detectors.

Each straw is filled with gas that becomes ionized when a charged particle passes through. The ions produce a current in a high-voltage wire running through the straw, creating a pattern of signals in many straws that allow the path of the particle to be determined. It also contains alternating materials with very different indices of refraction, causing charged particles to produce transition radiation and leave much stronger signals in each straw. Since the amount of transition radiation produced is greatest in highly relativistic particles (those with a speed near the speed of light), and particles of a particular energy have a higher speed the lighter they are, particle paths with many very strong signals can be identified as the lightest charged particles, electrons. The TRT is described in more detail in chapter 1.2.5

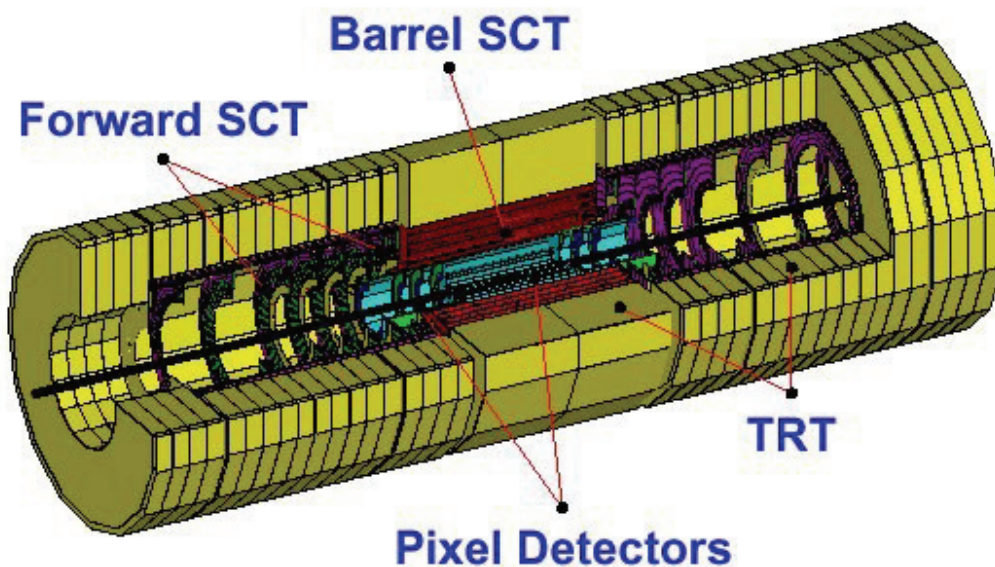


Figure 3: Three dimensional view of the ATLAS Inner Detector

1.2.5 The Transition Radiation Tracker (TRT)

The Transition Radiation Tracker (TRT) is a combination of a *straw tracker* and a *transition radiation detector*. A straw tracker is a type of particle detector which uses many straw chambers (see below paragraph *The Straw Tube*) to track the path of a particle. The path is determined by the best fit to all the straws with hits. A transition radiation detector is a particle detector utilizing the γ -dependent threshold of transition radiation in a stratified material. It contains many layers of materials with different indices of refraction. At each interface between materials, the probability of transition radiation increases with the relativistic γ -factor. Thus particles with large γ give off many photons, and small γ give off few. For a given energy it allows a discrimination between a lighter particle (which has a high γ) and a heavier particle (which has a low γ). The γ -factor (also known as Lorentz factor) is the total particle energy E in units of the particle rest energy mc^2 .

It is defined as:

$$\gamma = \frac{E}{mc^2} = \frac{1}{\sqrt{1-\beta^2}} \quad \beta = \frac{v}{c}$$

Where v is the velocity in m/s and c is the speed of light. It applies to time dilation, length contraction and relativistic mass relative to rest mass in Special Relativity [31].

The TRT is based on the use of straw detectors, which can operate at the expected high rates due to their small diameter and the isolation of the sense wires within individual gas volumes. Electron identification capability is added by employing xenon gas to detect transition radiation photons created in a radiator between the straws.

Figure 4 shows the layout of the TRT. It has been optimized for the best performance in terms of track reconstruction and electron/pion separation in the extremely harsh operating conditions expected at the LHC. With an active length of 5.5 m and an active diameter of 2 m, the TRT consists of three parts: a central barrel and two end-caps. Each straw is 4 mm in diameter and equipped with a 30 μm diameter gold-plated tungsten wire. The maximum straw length is 144 cm in the barrel, which contains about 50000 straws, each divided in two at the center and read out at both end, to reduce the occupancy. The end-caps contain 320000 radial straws, with the readout at the outer radius. The total number of channels that are read out is 420000. Each channel provides a drift time measurement, giving a spatial resolution of 170 μm per straw, and two independent thresholds. These allow the detector to discriminate between tracking hits, which pass the lower threshold, and transition radiation hits, which pass the higher one. The barrel section (see Figure 5) is built of individual modules between 329 and 793 straws each, covering the radial range from 56 to 107 cm. The first nine layers are inactive over the central 80 cm of their length to reduce their occupancy. Each end-cap consists of 18 wheels (see Figure 6). The innermost 14 cover the radial range from 64 to 103 cm, while the last four extend to an inner radius of 48 cm. The production of the last four wheels has been staged. Wheels 7 to 14 have half as many straws per cm in z as the others, to avoid an unnecessary increase of material at medium rapidity. The design and construction of the TRT are described in more detail in reference [10, 11, 12].

The ionization current density will be 0.15 $\mu\text{A}/\text{cm}$ of wire leading to a maximum ionization current per wire of about 10 μA . After 10 years of operation the straws will accumulate a radiation dose of about 10 Mrad, and a neutron fluence of up to 2×10^{14} n/cm². These numbers include a 50% safety factor for uncertainties in the calculations. The total dose results in unprecedented ionization currents and integrated charges (up to ~ 10 C/cm of wire) for a large-scale gaseous detector. The TRT is operated with the non-flammable gas mixture Xe(70%)CO₂(27%)O₂(3%) with a total volume of 3 m³. In chapter 1.2.5.2 the choice of the TRT gas composition and its components is described in more detail.

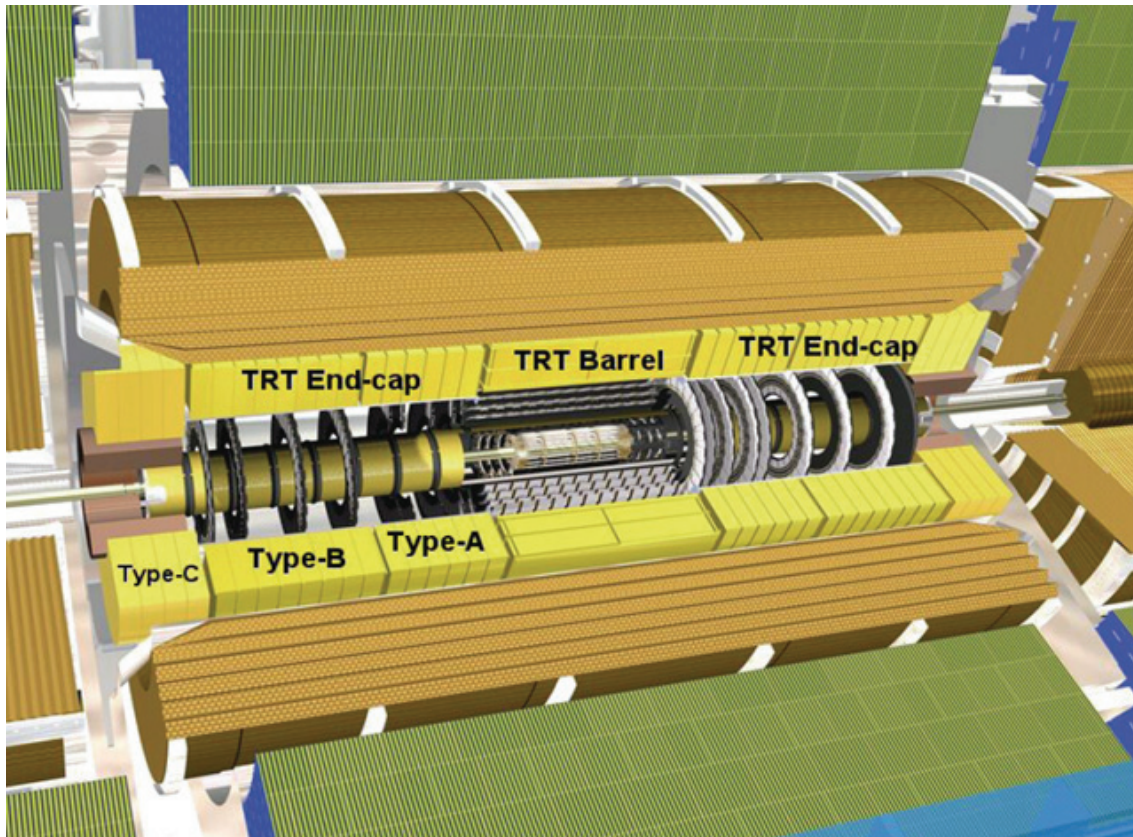


Figure 4: The Transition Radiation Tracker (TRT) of the ATLAS experiment

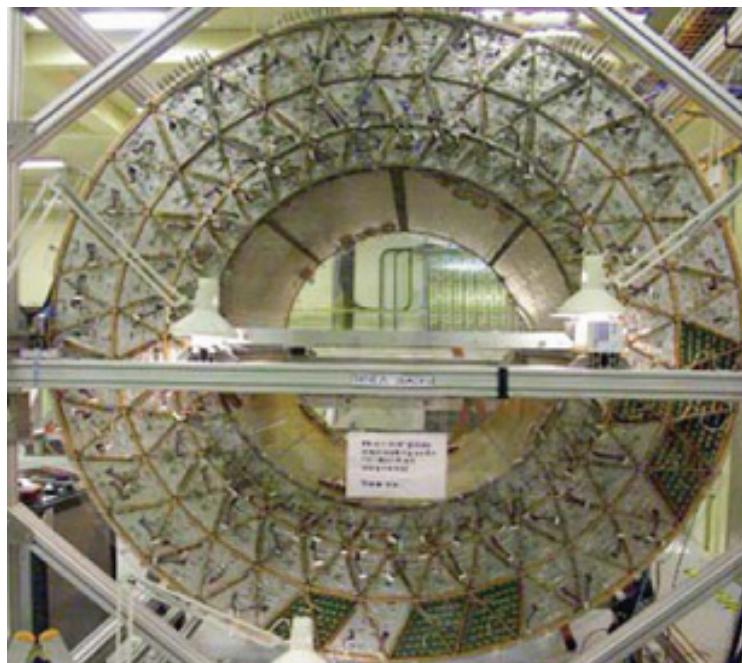


Figure 5: End view of the TRT barrel, which is made of 3 rings of 32 individual modules



Figure 6: End-Cap wheel of the TRT

The Straw Tube

The anode consists of a fine wire in the axis of the hollow tube, which functions as a cathode. The polarization is chosen in such a way because gas amplification, initiated by the electrons, is created only in the high field region around the anode wire and because a uniform multiplication factor is achieved with a small amplification region. In case of the TRT negative high-voltage is applied to the tube, while the anode wire is kept at ground potential.

The 4 mm diameter of the TRT tubes has been chosen because it is a good compromise between speed of response, number of ionization clusters, mechanical and operational stability. The tube is made of a 67 μm thick multilayer film of carbon-polyimide-aluminum-Kapton®-polyurethane (see Figure 7) [15]. It is manufactured by winding two tapes on a precisely tooled mandrel at a temperature of ~ 200 °C (see Figure 7). Four reinforcing carbon fibers glued along the straw give it the necessary mechanical stability for safe operation. In systems with anode read-out, the cathode resistance must be kept as low as possible (specification, 300 Ω/m). To guarantee this a thin aluminum coating serves as a second conductive layer against possible conductivity loss. Severe signal degradation can be caused by the removal of the inner carbon-loaded Kapton layer after several breakdowns.

The tungsten wire has a diameter of 30 μm and with the gold coating of about 0.5 μm the effective thickness of the anode wire is 31 μm [16]. It is produced by Toshiba. Wire diameter and ellipticity are specified to be better than 1% and 2% respectively. The electrical resistance is 60 Ω/m . Altogether the TRT requires about 450 km of wire for its construction, therefore strict wire quality measurements are necessary. Wire samples from each spool were inspected for electrical resistance and tensile strength. Surface quality and diameter variations (see Figure 8) were examined by using a scanning electron microscope (SEM).

As mentioned before the anode wire is kept at ground potential (through protection diodes) and is read out through a 24 Ω resistor by the front-end electronics (see Figure 9).

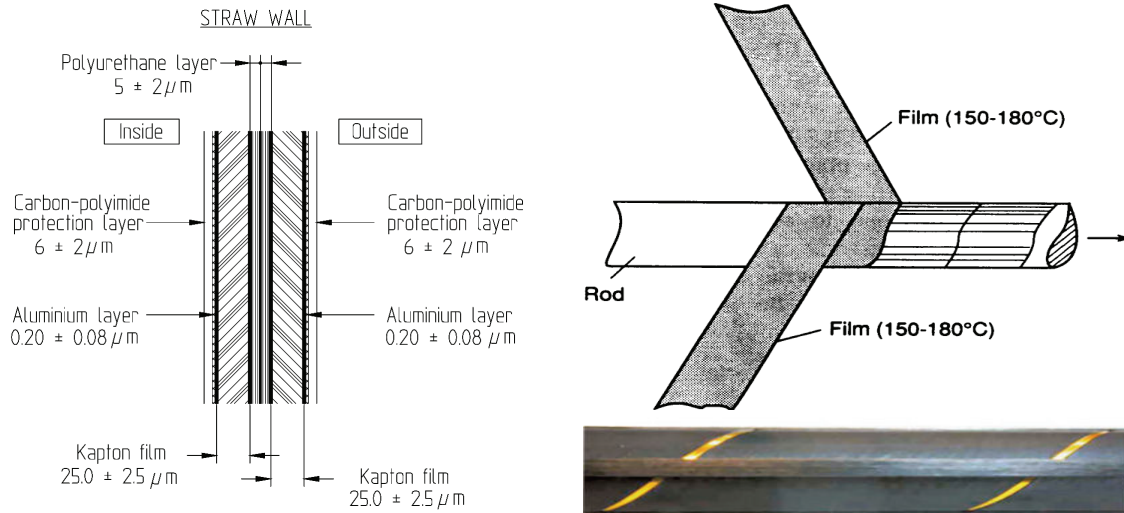


Figure 7: A multilayer film (left) is used to produce the straw tubes by winding two tapes of film on a precision mandrel (top right). Four carbon fibers strips on the outside reinforce the straw (bottom right) [25]

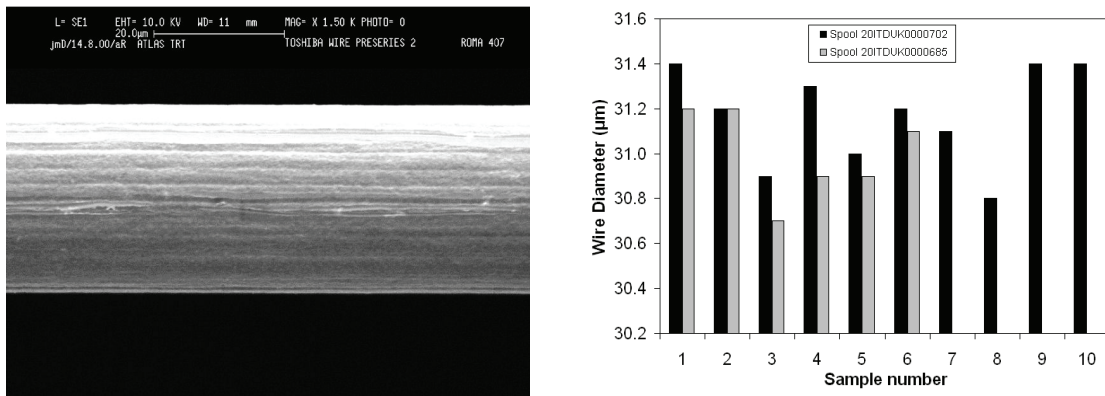


Figure 8: SEM picture from the wire surface quality control (left) and wire diameter variations (right) [25]

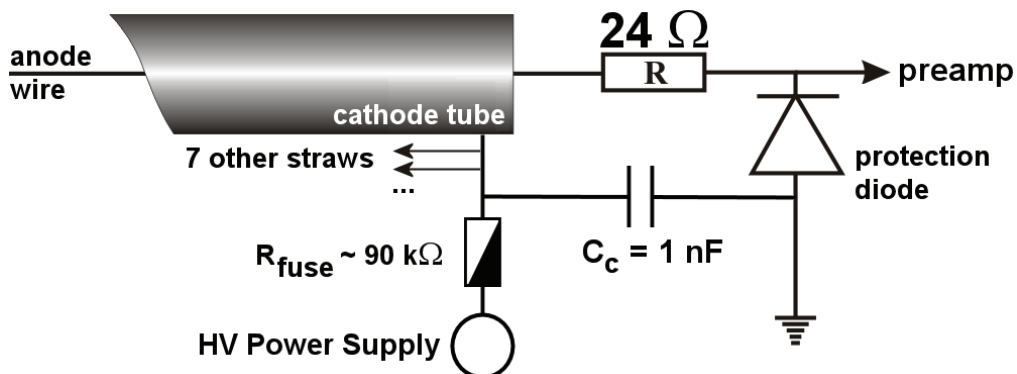


Figure 9: Straw high-voltage and signal connection scheme [25]

1.2.5.1 Choice of Material

The extremely harsh operating conditions expected at the LHC require a very careful choice of materials for all detector elements. The choice of materials was made on the considerations for the initial CF_4 containing gas mixture ($\text{Xe-CF}_4\text{-CO}_2$), the new mixture ($\text{Xe-CO}_2\text{-O}_2$) is CF_4 free, see also chapter 1.2.5.2, and therefore less reactive, corrosive and material destroying. For this reason are the selected materials also applicable for the new gas mixture.

In general stainless steel components are recommended [13], because many non-metallic materials outgas and therefore produce vapors, which may deposit directly on the surface of electrodes and insulators in the chamber or undergo polymerization processes in the avalanche plasma, leading to the formation of wire deposits in the irradiated zones. In both cases, the lifetime of the detectors can be seriously shortened.

The use of glues, plastics and other organic materials is unavoidable in the TRT and most of these materials will be placed in an extremely hostile radiation environment, and the material choices must therefore be made on the basis of their radiation robustness. For aging processes, one of the most important parameters which specify the radiation hardness of materials is the amount of gas which the material desorbs after irradiation. This effect is characterized by the so called G-value, which is the number of free molecules per 100 eV of absorbed radiation. The G-values for different materials are given in Table 2 [19]. There are a number of chemical groups which, when incorporated into the polymer chain, are resistant to radiation. Aromatic groups such as the phenyl groups in polystyrene have lower G-values (from ~ 0.03 to ~ 1). Aromatic groups in polymers absorb the excitation energy, but their excited states undergo efficient decay to the ground state with a low yield for bond cleavage (and hence for radical formation). Other examples of radiation-resistant aromatic polymers are polyimides and polyetherimides as can be seen in Table 2. One of the major guideline for the choice of materials for the construction of the TRT detector is therefore to use materials containing aromatic groups wherever possible.

Intensive studies of the impact of the anode wire material on aging effects have been performed in [20]. Different wires (Au/W, W, Cu, Al, Ni) were exposed to irradiation in CF_4 mixtures. The general recommendation of all the authors who have studied this effect [21, 22] is to use Au/W wire, particularly for the gas mixtures containing CO_2 and CF_4 .

The straw material should be able to operate up to an integrated dose of 10 Mrad without any indication of change of its properties. Materials which have been chosen for the multi-layer straw film are (see also chapter 1.2.5): Kapton (one of the most radiation-resistant plastic materials), Aluminum protected by a carbon-doped polyimide film and polyurethane. It has been demonstrated that the straw itself can easily tolerate a radiation dose corresponding to 100 years of LHC operation [23] in CF_4 mixtures.

Table 2: G-Values from plastics irradiated at 20 °C in air

Material	G-Value
Low-density polyethylene	3.86
High-density polyethylene	3.06
Polystyrene	0.026
Plasticised PVC	1.16
Unplasticised PVC	0.77
Poly-methyl-methacrylate	1.18
Poly-tetrafluor-ethylene	0.098
Nylon 6	1.02
Polycarbonate	0.86
Polyethylene terephthalate	0.17
Polysulfon (depends on chemical structure)	0.13-10
Epoxy resins	0.12-0.57
Polyimide (KAPTON)	0.00276
Polyether-ether-ketone (PEEK)	0.005
Polyetherimide (PEI, ULTEM)	0.014

1.2.5.2 Choice of Gas

The choice of gas for wire chamber operation is determined by various restrictions ranging from physics requirements over safety and environmental concerns up to financial considerations. There is no unique solution which fulfills all the possible demands. An optimum set of parameters should be found for every specific case. In general the gas should:

- be not too expensive
- be fast
- have a low electron diffusion constant affecting the resolution
- provide good aging characteristics for the chambers
- be non-flammable, non-corrosive and non-poisonous

The original TRT gas mixture was Xe(70%)CF₄(20%)CO₂(10%) [13]. The CF₄ component was chosen because of its small diffusion coefficient and large drift velocity. Several studies have demonstrated that the CF₄ creates very reactive fluorine-based species which degrade some materials used in the assembly of the detector, such as epoxy compounds, plastic materials and glass fiber components. In particular, the glass wire-joints inside the long barrel straws were etched to the point of breakage by fluorine radicals. Therefore the original gas mixture has been changed to Xe(70%)CO₂(27%)O₂(3%) which provides acceptable operational stability and equivalent physics performance [13].

Xenon is chosen for its excellent X-ray absorption (see Figure 10), the high costs of it requires a closed-loop gas system. The fraction of 70% xenon marks the balance between transition radiation performance and operation stability. The quencher CO₂, known as “cool gas”, provides excellent drift properties, namely a plateau of constant drift velocity over a large drift range in the straw (see Figure 12), low longitudinal diffusion and small deflection in magnetic fields. Furthermore it also represents the stabilizing factor in the

gas mixture efficiently absorbing UV photons produced in the ionization process and therefore spatially confining the avalanches. Rather than spreading along the wire the avalanche only develops radially as a streamer in case of very large charge creation from low momentum heavily ionizing particles or unforeseen electric field enhancement. The suppression of lateral spread such limits the streamer into a so-called self-quenched streamer (SQS) mode. Although still not being a desired operation mode it is less hostile than a total discharge between cathode and anode. A minimum of 6 % of CO_2 is needed for the TRT to confine discharges to SQS mode. More information about self-quenched streamer mode in gas-discharge detectors can be found in [17].

Unfortunately the binary mixture Xe-CO_2 cannot provide stable operation over a sufficient high-voltage range in the straws tubes, the use of a ternary mixture remained the only feasible solution. Hydrocarbon gases are usually used to stabilize the amplification process in wire chambers, but they are prone for polymerization and would deposit on the anode wire.

Finally an alternative mixture was found using O_2 with a concentration of 3 %. Concentrations below 3.5-4 % do not influence the TRT performance, while a minimum of 2 % is needed to provide good operational stability (see Figure 13). O_2 itself is transparent to UV photons, the stabilization is provided by the Ozone molecules (O_3) created in the avalanches. The consequently loss in amplitude due to the high electronegativity of O_3 was measured to be at most 13 % at current densities of $0.125 \mu\text{A/cm}$, corresponding to O_3 concentrations of not more than 150 ppm, which is acceptable for the TRT operation [18].

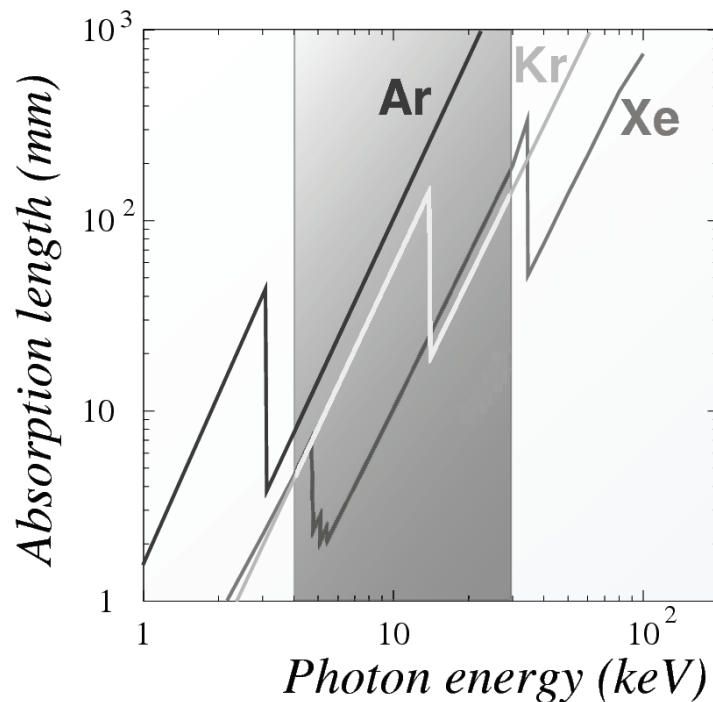


Figure 10: Photon absorption length of argon, krypton and xenon

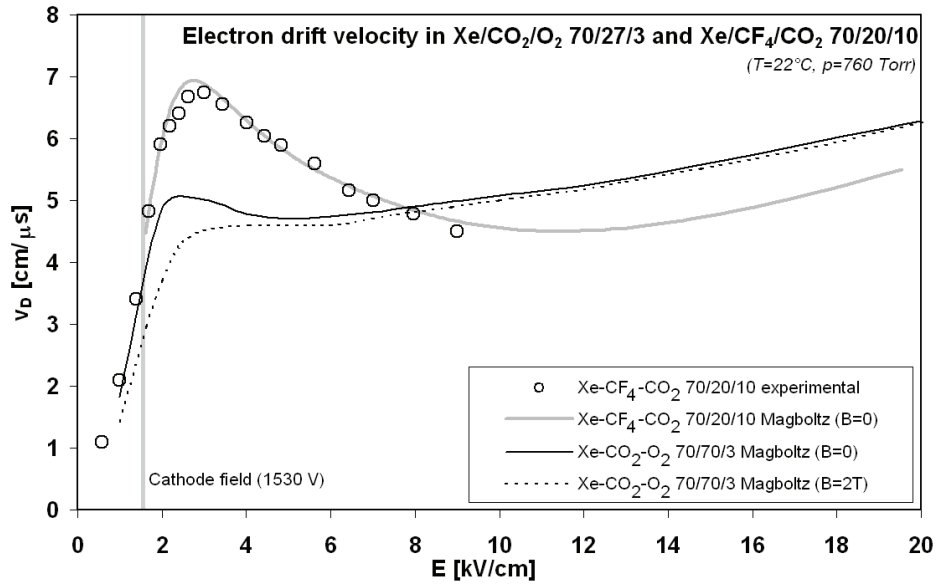


Figure 11: Electron drift velocity versus energy for the gas mixtures Xe-CO₂-O₂ and Xe-CF₄-CO₂ [26]

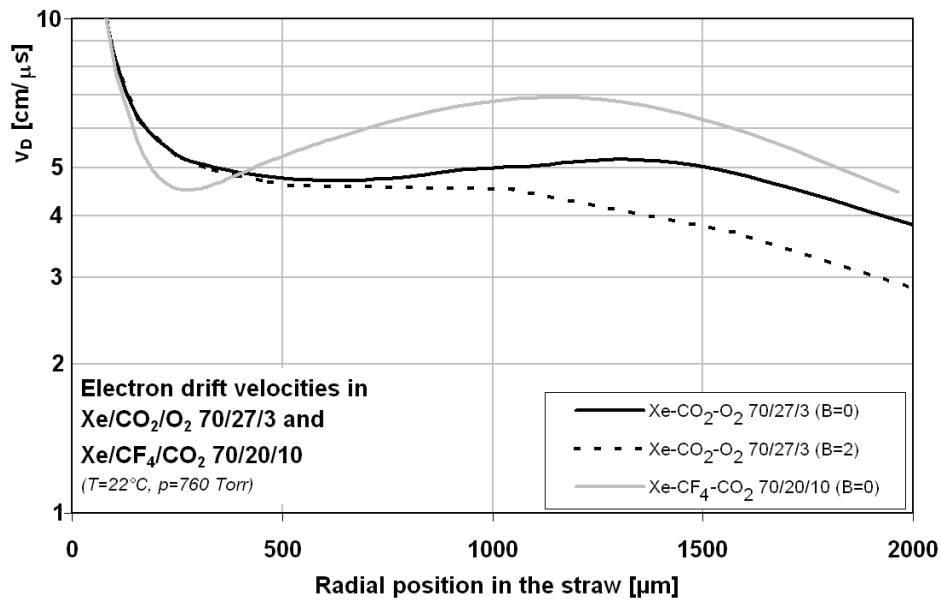


Figure 12: Electron drift velocity versus the radial position in the straw for the gas mixtures Xe-CO₂-O₂ and Xe-CF₄-CO₂ [26]

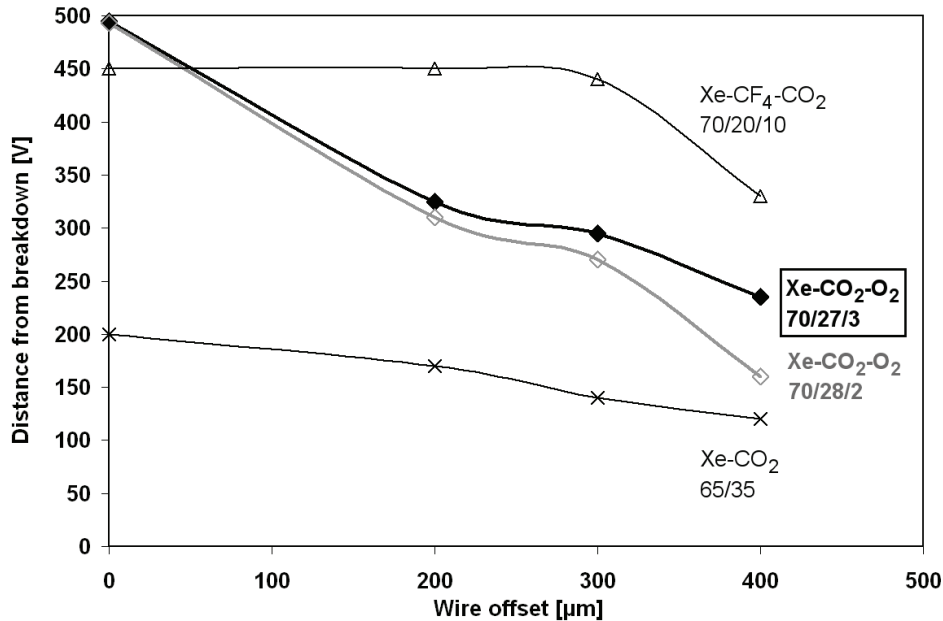


Figure 13: Distance from operating voltage to point of high-voltage breakdown in the straw for different wire offsets and gases [18]

1.2.5.3 Aging Problems of the TRT

The original TRT gas mixture was Xe(70%)CF₄(20%)CO₂(10%) [13]. Plasmachemical reactions occurring in the straw operation under irradiation produce very reactive fluorine-based species (HF, F, F₂...) which attack some detector materials and cause damage. In particular, the glass wire-joints inside the long barrel straws were etched to the point of breakage by fluorine radicals. Therefore it was necessary to replace the original gas mixture. It has been changed to Xe(70%)CO₂(27%)O₂(3%) which provides acceptable operational stability and equivalent physics performance [13]. It is furthermore less reactive, corrosive and material destroying.

An advantage of the original gas mixture was that the CF₄ radicals could prevent the formation of hydrocarbon and SiO_x wire deposits [14]. With the new gas mixture the TRT is much more sensitive to organosilicon impurities because the oxygen radicals which are created in the gas avalanche can prevent hydrocarbon wire deposits but not silicon based ones [24]. Already small concentrations of certain gaseous constituents can have very dramatic effects upon the rate of wire aging. These impurities result from outgassing processes of silicon based materials in contact with the gas. To guarantee the demanded 10 years lifetime of the TRT a systematic validation procedure for selecting components for the construction of the final closed-loop gas system has been developed. This effort should avoid the presence of organosilicon containing components in the gas system. However, being aware of the problem that the construction of an absolute clean gas supply is almost impossible we were looking for a feasible gas cleaning procedure. Intensive efforts were made to identify the origin and the composition of the aging causing impurities which was an important precursor to understand the deposition mechanism. Furthermore it helped to prevent wire aging and to develop a gas purification method.

1.2.5.4 Etching of Silicon Deposits with CF₄

It has been found that a small addition of CF₄ to the gas mixture Ar-CO₂ is able to clean up aged wires [24]. This capability can be used for a periodically cleaning of wire chambers, if needed. In these tests, straws were aged in an Ar(70%)CO₂(30%) gas mixture bubbled through silicon containing oil. The straws were irradiated with a ⁹⁰Sr source over their full length and the gas gain was monitored regularly. After a gain reduction of about 20%, the organosilicon polluted Ar-CO₂ gas mixture was replaced by Ar(70%)CF₄(8%)CO₂(22%) and the straws were again radiated. Full recovery of the gas gain was observed over most of the straw length, except the gas inlet, after a few hours. Several studies have been carried out to determine the safe operating lifetime limit of the glass wire-joint in the barrel straws in CF₄ mixtures, as a function of the CF₄ fraction (16%, 8% and 4%), the moisture level, the gas gain and the irradiation dose [24]. The failure of the wire-joint is defined as the quantity of accumulated charge in C/cm of wire for which, after a loss of wire tension due to etching of the glass wire-joint, the wire breaks. From this and other sets of systematic measurements, the following has been concluded:

- Silicon deposits can be etched away, with the exception of the very first centimeters of the straw, close to the gas inlet, which would require flushing the cleaning gas in the opposite direction.
- The gas gain is restored to its original value.
- No residual effect is seen when the gas is switched back to a non-CF₄ mixture.
- The wire-joint failure limit for different concentrations of CF₄ are ~ 0.15 C/cm for 4%, 0.10 C/cm for 8% and ~ 0.05 C/cm for 16%.
- It has also been observed that the wire-joint failure limit is roughly proportional to the water concentration in the gas.

From these observations, it is estimated that about 30 cleaning days can safely be performed in ATLAS for 4% to 8% concentration of CF₄ in the cleaning gas. Thus, for the case that aging appears in the TRT the gas gain can be restored by operating the detector for a short period of time, about two days per year, with the cleaning gas mixture.

1.3 Previous Aging Studies

1.3.1 Introduction

High Energy Physics experiments are currently entering a new era which requires the operation of gaseous particle detectors at unprecedented high rates and integrated particle fluxes. During the course of experiments using these detectors full functionality is expected for several years. Although there are a few manifestations of these problems, including loss of gain, loss of gain uniformity, loss of energy resolution, excessive and

self-sustained currents, sparking, anode wire corrosion and some more different types of damages, the generic term *aging* is used to describe all forms of performance degradation. These effects are caused by the formation of deposits on the anode or cathode surface or through material damages by aggressive radicals (species with unpaired valence electrons) produced in the avalanche.

The 1st workshop on wire chamber aging was held at LBL, Berkley in 1986. The early studies of wire aging have been aimed at discovering satisfactory sets of operation conditions and not on fundamental research about the processes leading to aging. This approach reflects the poor understanding of the chemical processes involved in aging. Although the basic phenomenology of aging effects has been studied in an impressive number of experiments in the following years not lot of progress in understanding the aging mechanism has been made till the 2nd aging workshop at DESY in Hamburg (2001). At present, aging mechanisms are only partially understood, and the review of the 2001 aging workshop at DESY covers much of what is known today about wire chamber aging [28].

Even there was a wide agreement among researcher in the field that aging is due to certain types of impurities in the gas, specific contaminants have only rarely been identified. Trace components have a large influence on the processes responsible for aging, but it has to be considered that aging effects are a result of the combination of contaminants, bulk gas composition as well as the anode and cathode materials.

The wire chamber aging problem is very complex, many chemical processes are expected to occur simultaneously in the gaseous discharges surrounding the wire and consequently a quantitative description of aging effects is difficult. Due to the different requirements placed on wire chambers by different applications it is not possible to give a unique solution for wire aging. Fundamental gas analysis and the identification of the dominant plasma chemical reactions can provide a qualitative description of the processes responsible for chamber degradation in any specific application. This approach will guide the development of methods and procedures for a safe chamber operation over the full lifetime of the experiment.

1.3.2 Aging Phenomena

The classical aging effects are the results of plasma chemical reactions occurring in the avalanches surrounding the anode wire. In the avalanches molecules dissociate through electron impact collisions, heavy particle collisions or photon exposure. The degradation can occur on both the anode and the cathode, but with very different results (see chapter 1.3.3 and 1.3.4). In general the deposits can have various forms: thin films, whiskers, powder, liquid drops. They can be insulating or electrically conductive

The ionization processes require electron energies greater than 10 eV, whereas the formation of radicals requires only 3-4 eV. This leads to a higher concentration of free radicals than of ions in the gaseous discharge. Cathode aging induced by positive ions drifting towards the cathode will occur therefore less likely than anode wire aging through deposit formation by neutral radicals. Anode aging is for that reason dominating and this work is focused on this phenomena.

In the literature the aging rate R , has been parameterized as a normalized gas gain loss:

$$R = -\frac{1}{G_0} \frac{dG}{dQ}$$

Where G_0 is the initial gain, dG is the loss of gas gain after collected charge dQ per unit length [22].

R is expressed in $\frac{\%cm}{C}$.

1.3.3 Anode Aging

One of the main characteristics of straw detectors is the presence of a very high field near the anode wire where dissociation and ionization processes occur.

Highly aggressive radicals produced in the avalanche can either attack the anode material directly and degrade it or combine with other molecules and form larger ones (polymerization). The growth of the molecules causes also an increase of their dipole moments. Thus they can get attracted by the electric field near the wire and when the polymerized chains comes large enough they can condense on the wire surface as a solid or liquid substance.

Oxygen radicals are formed in bulk gases containing O_2 or CO_2 . If organosilicon impurities are present intermediate products are produced by eliminating hydrocarbon side chains. It can be concluded that the oxygen and the oxygen radicals converts the eliminated hydrocarbon gases into volatile oxides (CO_2 and H_2O) which leave the chamber with the current gas flow. In addition the dissociation of intermediate compounds continues through oxidation which leads to the formation of SiO_x and $SiO-R$ wire deposits. Higher O_2 concentrations result in a lower carbon content in the deposit (the purer SiO_x films are produced). However, organosilicon dissociation and deposition phenomena are not understood clearly.

Deposits usually cause a gain loss due to the increase of the effective diameter of the wire. Figure 14 shows some general examples for wire aging. Nevertheless gain drop can also occur through the reduction of the electric field caused by an accumulation of charge on an insulating layer. The variation of the deposit thickness along the wire causes a variation of the gain and, consequently, a loss in pulse-height resolution.

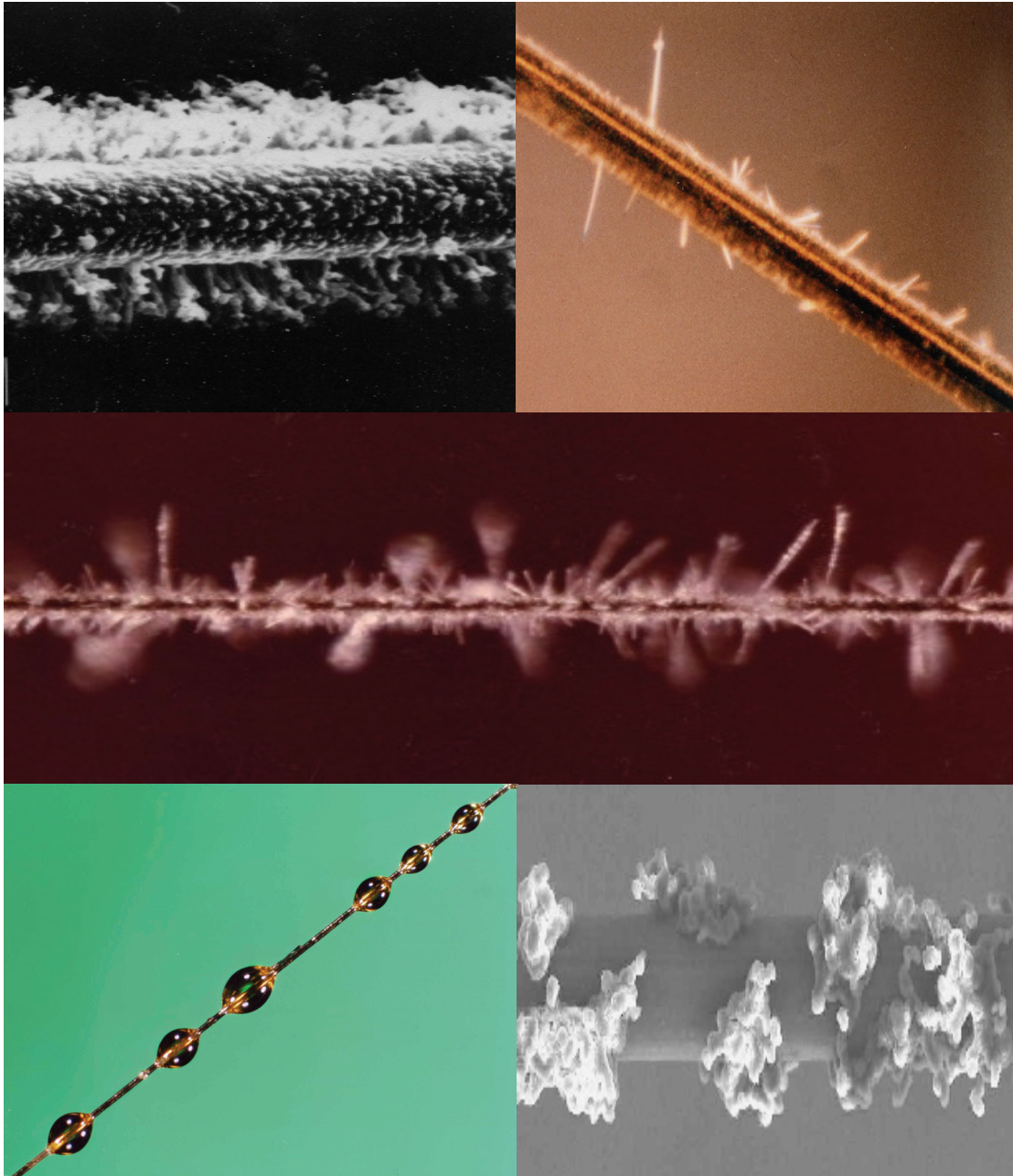


Figure 14: Some examples for wire aging

1.3.4 Cathode Aging

The main mechanisms of cathode aging are etching processes of the cathode material through aggressive radicals formed in the avalanche and deposit formation on the cathode surface.

The most dangerous and devastating phenomena of all aging effects is the Malter effect [29]. It causes a self-sustained discharge, which is due to a thin insulating layer deposited on the conducting cathode. The insulating layer prevents positive ions created in the

avalanche from reaching the cathode and being neutralized. Instead these ions accumulate on the layer and create a dipole field which, if it exceeds the threshold for field emission, can eject electrons from the cathode. Many of them recombine with positive ions immediately, but some of them drift to the anode and generate avalanches. This process can develop into a continuous, self-sustaining current in the chambers without an external flux of ionizing particles. The most dangerous aspect of the Malter effect is that it easily can spread over a large area, if it remains undetected for a long period of operation, causing irreparable damages to the chamber.

1.3.5 Outgassing of Materials

Aging is a complex phenomenon that depends, among other parameters, on the purity of the gas mixture. The origin of the pollutants is diverse and includes outgassing from assembly materials, contamination of the detector during the assembly process and the gas system itself. Systematic studies on this topic have been carried out [30].

To construct a gas system completely free (below ppb level) of hydrocarbons is impossible. Even stainless steel pipes will pollute a clean gas mixture with a low amount of hydrocarbons, however, not all impurities are harmful for the detector operation.

Outgassing studies can help to choose the right materials for the detector construction but they have some limitations like:

- the incapability to detect substances below some given quantity (for mass spectrometers and gas chromatographs the detection limit is about 100 ppb)
- the inability to separate and identify certain compounds
- the incapacity to designate if detected impurities are harmful for the detector operation

Therefore a low outgassing characterization for materials can be considered as a guideline but the definitive test should be done by an aging test with a straw prototype (see chapter 6). This allows correlating the presence of impurities in the gas with aging effects in the detector.

Table 3 shows a partial list materials tested for outgassing, characterized by gas chromatograph measurements [31]. The detected pollutant concentration is in average at ppm level.

Table 3: Partial list of materials tested for outgassing. For a few substances the gas chromatograph detects pollutants at ppm level

Material	Outgassing Detected	Comment
STYCAST 1266 (A+B)	no	epoxy
ARALDITE AW103	no	epoxy
ARALDITE AW106	yes	epoxy
TRABOND 2115	no	epoxy
DURALCO 4525	yes	epoxy
EPOTEK E905	yes	epoxy
SCOTCH 467 MP	yes	adhesive
VARIAN Torr-Seal	no	sealant
LOCTITE 5220	yes	sealant
POLYCARBONAT	no	rigid
RYTON	yes	rigid
POLYPROPYLENE	no	plastic pipe
PEEK crystalline	no	plastic pipe
PEEK amorphous	yes	plastic pipe
VITON	yes	O-rings
EPDM	yes	O-rings

2 Wire Chamber Theory

2.1 Introduction

It is useful to have a qualitative understanding of the electron avalanche to understand wire aging phenomena.

The electron avalanche is the mechanism for the process of gas gain, wherein a charged particle is converted to a pulse of typically $10^4 - 10^5$ electrons. An avalanche is initiated when a charged particle drifting in a gas enters a region of sufficiently high electric field ($\sim 10^5$ V/cm at atmospheric pressure) near an anode wire that it gains enough energy to undergo ionizing collisions with gas molecules, thereby freeing more electrons. These electrons drift along the electric field lines towards the anode and are multiplied in an avalanche process close to the wire due to the high field ($E \sim 1/r$). Movement of ions and electrons induces a current in the wire, which is read out by an amplifier. The gain is simply the amplification factor of the avalanche.

In very simplified terms, a wire chamber is a gas filled three dimensional array of thin anode wires and cathodes. The anode/cathode array establishes an electric field appropriate to the desired detection task. When a sufficiently energetic charged particle passes through the chamber, it ionizes some of the gas molecules along its path, leaving a thin ionization trail (particle track). The electrons freed by this ionization drift towards an anode where they initiate avalanches and are thus detected. Since the velocity of drifting electrons is known, the measured time of drift determines the position of the track relative to the wire. From such measurements on many wires, the track of the detected particle can be completely reconstructed.

2.2 Interactions of Particles with Matter

Particles and radiation cannot be detected directly but through their interactions with matter. The main interactions of charged particles are ionization and excitation. For relativistic particles, Bremsstrahlung energy losses must be considered. Neutral particles must produce charged particles to be detected via their characteristic interaction processes. In the case of photons these processes are the photoelectric effect, Compton scattering and pair production of electrons. The electrons produced in these photon interactions can be observed through their ionization in the sensitive volume of the detector.

2.2.1 Detection of Charged Particles

Charged particles can be detected directly through their electromagnetic interactions. If a charged particle passes a layer of material, three processes can occur: atoms can be ionized, the particle can emit Cherenkov radiation or the particle can cause the emission of transition radiation.

Ionization and excitation processes cause an energy loss which can be described by the Bethe-Bloch equation [34]:

$$-\frac{dE}{dx} = 4N_A \pi r_e^2 m_e c^2 z^2 \frac{Z}{A} \frac{1}{\beta^2} \left[\ln \left(\frac{2m_e c^2 \gamma^2 \beta^2}{I} \right) - \beta^2 \right] \quad \text{with} \quad \beta = \frac{v}{c}$$

With:

- z charge of incident particle in units of the elementary charge
- Z, A ... atomic number and weight of the absorber
- m_e electron mass
- r_e classical electron radius
- N_A Avogadro number
- I ionization constant
- c speed of light
- v velocity
- γ Lorentz factor

At low energies the energy loss caused by ionization prevails. The dominating total energy loss, even for heavy particles, at very high energies is due to Bremsstrahlung (radiation losses). In contrast to the ionization energy loss it is proportional to the energy of the particle and inversely proportional to the mass squared of the incident particle.

If a charged particle is decelerated in a Coulomb field a fraction of its kinetic energy will be emitted in form of photons (Bremsstrahlung). This energy loss can be described by following equation [34]:

$$-\frac{dE}{dx} = 4\alpha N_A z^2 \frac{Z^2}{A} \left(\frac{1}{4\pi\epsilon_0} \frac{e^2}{mc^2} \right)^2 E \ln \frac{183}{Z^{\frac{1}{3}}}$$

With:

- z charge of incident particle in units of the elementary charge
- Z, A ... atomic number and weight of the medium
- m mass of incident particle
- E energy of incident particle
- α fine structural constant
- ϵ_0 permittivity of free space

The Bremsstrahlung energy loss for electrons is therefore [34]:

$$-\frac{dE}{dx} = 4\alpha N_A \frac{Z^2}{A} r_e^2 E \ln \frac{183}{Z^{\frac{1}{3}}}$$

Because of the small electron mass the Bremsstrahlung energy loss plays an especially important role for electrons.

2.2.2 Detection of Photons

Photons are detected indirectly through the interaction with the detector medium. In these processes charged particles are produced which causes ionization in the sensitive volume of the detector and can therefore be recorded. Interactions of photons are different from ionization processes of charged particles because in every photon interaction, the photon is either completely absorbed (photoelectric effect, pair production) or scattered through a relatively large angle (Compton effect). If a beam of photons with intensity I_0 traverses a layer of material of thickness x the intensity emerging from the layer is defined as [35]:

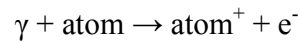
$$I = I_0 e^{-\mu x}$$

The length x is a surface mass density with the dimension g/cm^2 . If the length is measured in cm, the mass absorption coefficient μ must be multiplied by the density ρ of the material. The mass absorption coefficient μ is related to the cross-section σ for photon absorption according to [35]:

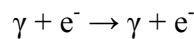
$$\mu = \frac{N_A}{A} \sum_i \sigma_i$$

Here N_A is the Avogadro number and A is the mass of a mole of the material.

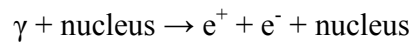
The photoelectric effect in which all the energy of the photon is transferred to a bound atomic electron dominates at low energies ($100 \text{ keV} \geq E_\gamma \geq 10 \text{ keV}$).



The Compton effect where the photon scatters a quasi-free electron dominates at medium energies ($E_\gamma \sim 1 \text{ MeV}$).



At high energies the cross section for pair creation is prevailing ($E_\gamma \gg 1 \text{ MeV}$).



2.2.3 Drift and Diffusion of Charges in Gases

Electrons and ions, produced in an ionization process, give up their energy by multiple collisions with other atoms and molecules of the gas. The average thermal energy ε of a gas molecule with three degrees of freedom is:

$$\varepsilon = \frac{3}{2}kT$$

In this equation k is the Boltzmann constant and T the temperature in Kelvin. At a temperature of 273 K, $\varepsilon_T \sim 40$ meV. The distribution of kinetic energies is defined by the Maxwell-Boltzmann equation:

$$F(\varepsilon) = \text{const} \sqrt{\varepsilon} e^{-\frac{\varepsilon}{kT}}$$

The locally produced ionization diffuses by multiple collisions corresponding to a Gaussian distribution. The diffusion coefficient D is then defined by the following functional form of the differential distribution dN/N of charges as a function of the spatial coordinate x at time t :

$$\frac{dN}{N} = \frac{1}{\sqrt{4\pi Dt}} e^{-\frac{x^2}{4Dt}} dx$$

For linear or volume diffusion the standard deviation σ of this distribution is:

$$\sigma_x = \sqrt{2Dt} \quad \sigma_{vol} = \sqrt{3}\sigma_x = \sqrt{6Dt}$$

The average mean free path λ during the diffusion process is given by the collision cross section $\sigma(\varepsilon)$, which depends on the kinetic energy of the charged particles:

$$\lambda(\varepsilon) = \frac{1}{N\sigma(\varepsilon)} \quad N = \frac{N_A}{A} \rho$$

Here N is the number of molecules per volume, A is the molar mass, ρ is the density of the gas and N_A the Avogadro number. For noble gases one has $N = 2.69 \cdot 10^{19}$ molecules/cm³ at standard temperature and pressure.

If the charge-carriers are exposed to an electric field, an ordered drift along the field will be superimposed over the statistically disordered diffusion. The drift velocity \vec{v} can be defined according to [35]:

$$\vec{v}_{drift} = \mu_{(E)} \vec{E} \frac{P_0}{p}$$

In this equation $\mu_{(E)}$ is the energy dependent charge-carrier mobility, \vec{E} the electric field strength and p/p_0 the pressure normalized to the standard pressure.

An important presupposition for the drift of free charge-carriers in an electric field is that electrons and ions do not recombine and that they are also not attached to atoms or molecules of the medium in which the drift proceeds.

For some molecules and atoms the diffusion coefficients D^+ , the mobility μ^+ , the mean free path λ and the mean thermal velocity u are summarized in Table 4 [35].

The corresponding quantity of electrons strongly depends on the energy of the electrons and on the field strength. The mobility of electrons in gases is approximately three orders of magnitudes higher than that one of ions.

A simple and easy way to express the drift velocity \vec{v} is the following equation:

$$\vec{v}_{drift} = \frac{e}{m} \vec{E} \tau(\vec{E}, \varepsilon)$$

Here \vec{E} is the electric field strength, τ the time between two collisions and ε the electron energy. Figure 15 shows the Ramsauer cross-section for electrons in argon as a function of the electron energy and Figure 16 shows the drift velocities for electrons in argon-methane mixtures.

The drift characteristics of electrons in gases are strongly modified in the presence of a magnetic field. In addition to the electric force also the Lorentz force acts on the charge-carriers and forces them into a circular or spiral orbit. The path of the charge-carriers can be described with the following equation of motion [35]:

$$m\ddot{\vec{x}} = q\vec{E} + q\vec{v} \times \vec{B} + m\vec{A}(t)$$

Here $m\vec{A}(t)$ is a time dependent stochastic force, which has its origin in collisions with gas molecules, \vec{E} is the electric field and \vec{B} the magnetic field. The drift velocity \vec{v} can be derived from the above equation by assuming that the time average product $m\vec{A}(t)$ can be represented by a velocity proportional friction force $-m\vec{v}/\tau$, where τ is the average time between two collisions, to be:

$$\vec{v}_{drift} = \frac{\mu}{1 + \omega^2 \tau^2} \left(\vec{E} + \frac{\vec{E} \times \vec{B}}{B} \omega \tau + \frac{(\vec{E} \cdot \vec{B}) \cdot \vec{B}}{B^2} \omega^2 \tau^2 \right)$$

In the drift velocity equation ω is the cyclotron frequency which can be derived from $m r \omega^2 = e v B$.

If $\vec{E} \perp \vec{B}$, the angle between the drift velocity \vec{v}_{drift} and \vec{E} (the Lorentz angle) can be calculated with following equation:

$$\tan \alpha = \omega \tau$$

Table 4: Thermal velocity u , diffusion coefficient D^+ , mobility μ^+ and the mean free path λ of ions in their own gas for standard temperature and pressure

Gas	Mass number	u [cm/s]	D^+ [cm ² /s]	μ^+ [cm ² /Vs]	λ [10 ⁻⁵ cm]
H ₂	2.02	1.8E+05	0.34	13.0	1.8
He	4.00	1.3E+05	0.26	10.2	2.8
Ar	39.95	4.1E+04	0.04	1.7	1.0
O ₂	32.00	4.6E+04	0.06	2.2	1.0
H ₂ O	18.02	6.1E+04	0.02	0.7	1.0

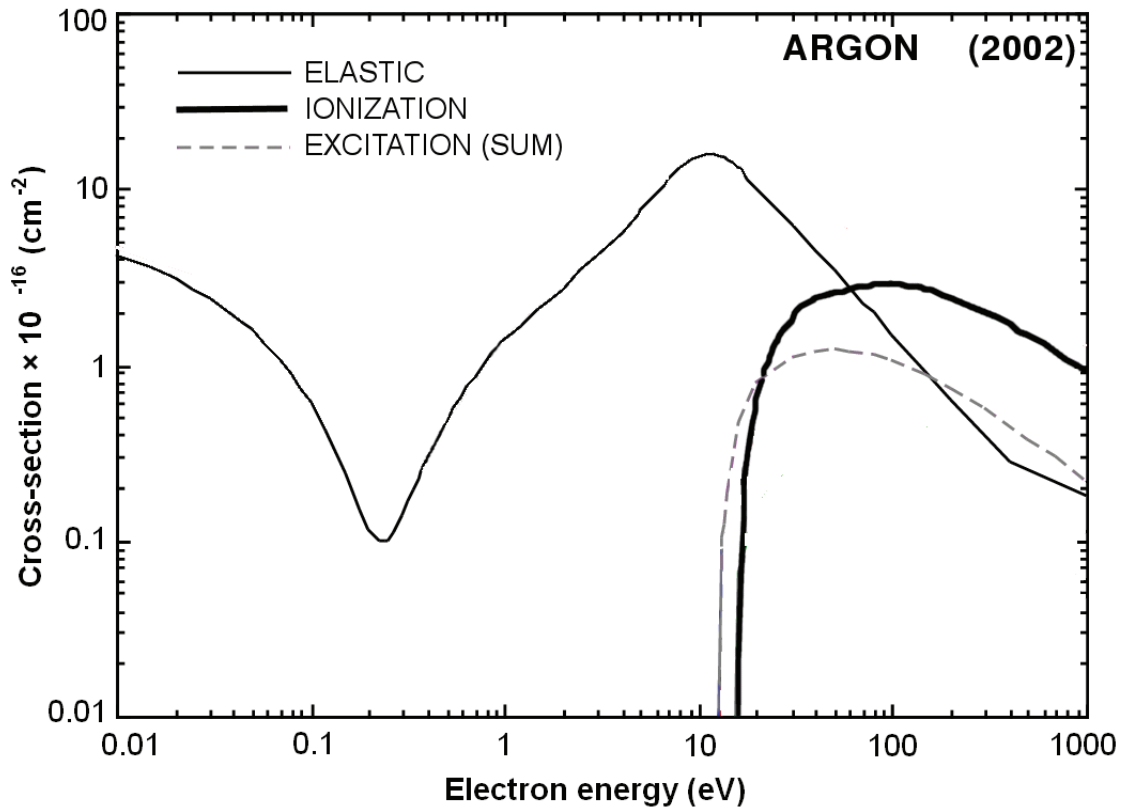


Figure 15: Collision cross-section for electrons in argon as a function of electron energy ε [37]

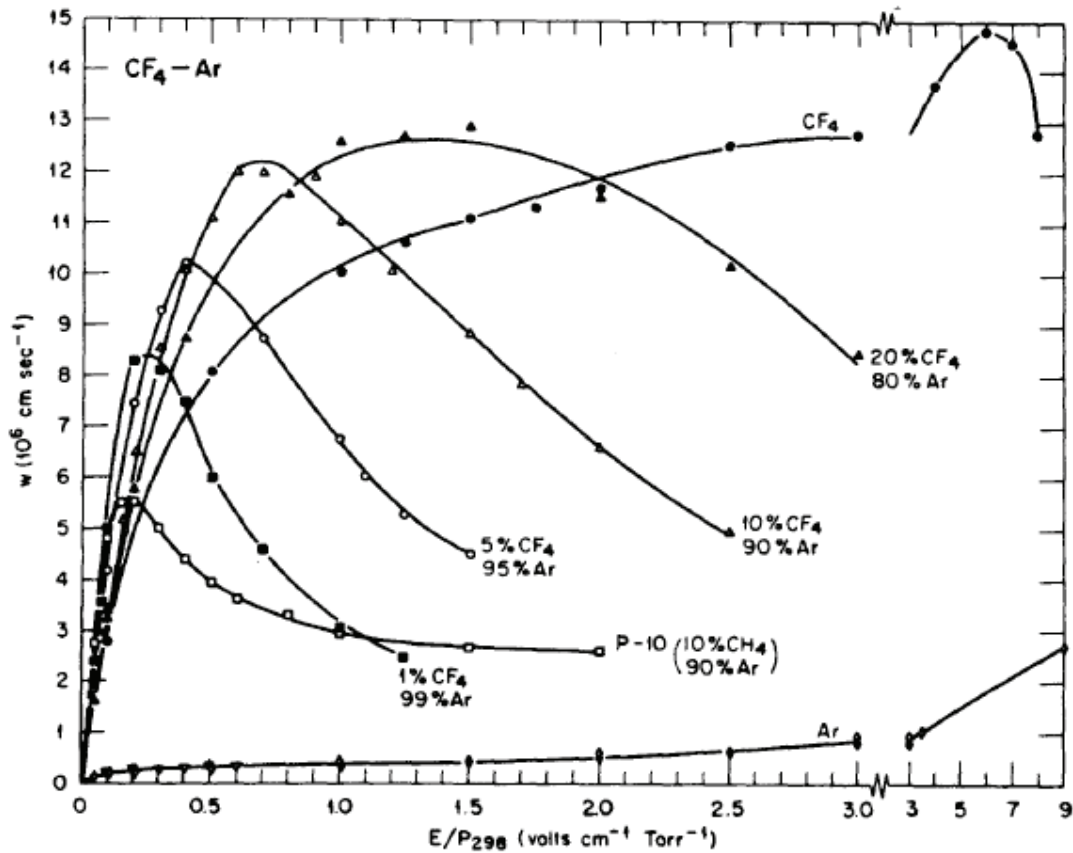


Figure 16: Drift velocities for electrons in argon-methane mixtures [37]

2.3 Measurement of Ionization

2.3.1 Ionization Chambers

The term *ionization chamber* is commonly used for detectors in which ion pairs are collected from gases. They are the simplest of all gas-filled detectors. In these chambers the ionization produced by a passing particle is measured. They can operate in a pulse mode or in a current mode. In the first case the pulse induced by each individual incident particle is measured independently; in the second case the average DC current produced by the sequence of incident particles is recorded.

In the simplest case an ionization chamber consists of a system of parallel electrodes. A voltage applied across the electrodes produces a homogeneous electric field. The electrode pair is placed in a gas tight volume that is filled with a gas mixture which allows electron and ion drift. This means it does not contain electronegative gases.

In principle the counting medium can also be a liquid or even a solid (solid state ionization chamber). The essential properties of ionization chambers are not changed by the state of the counting medium.

If a charged particle passes through the gas it causes ionization. Through the electric field the electrons and negative ions drift towards the anode and are collected there. A minimum ionizing particle leaves about 120 ion pairs per cm, the signal produced is therefore very small. With a voltage of about 100 V applied across a small chamber, the drift times will be typically 10 μ s for the electrons and 10 ms for the heavier ions.

Ionization chambers are therefore

- insensitive to single minimum ionizing particles, and more useful for heavy (slow) ions.
- slow, suitable for an environmental radiation monitor with a DC current indicating a steady flux of particles.

If a liquid is used instead of a gas, the higher density (and lower ionization potential) leads to a considerable increase in signal. Suitable liquids are for example

- argon (which requires a cryogenic system).
- room temperature liquids, such as TMP (tetramethylpentane) and TMS (trimethylsilane), which must be kept extremely pure to avoid electron capture.

More detailed information about ionization chambers can be found in [34, 35, 36].

2.3.2 Proportional Counters

Proportional counters are almost always operated in pulse mode and they differ from ionization chambers discussed above by the phenomenon of gas multiplication. Charges represented by the original ion pairs created in the gas are getting amplified and pulses are therefore significantly larger than those from ion chambers under the same conditions. Proportional counters can be applied to situations where the number of ion pairs generated by the radiation is too small to permit satisfactory operation in pulse type ion chambers.

The Counter Geometry

The disadvantage of planar ionization chambers is that the electric field strength is constant. The simplest way of producing a local region of high electrical field is to utilize a cylindrical geometry with a very fine central sense wire acting as anode. In this way, the amplification region is surrounded by a lower field, and there is no danger of a direct breakdown between the electrodes. The maximum of the electric field occurs close to the wire surface (see Figure 17). For cylindrical geometries the electric field E at radius r is given by:

$$E_{(r)} = \frac{V}{r \ln\left(\frac{b}{a}\right)}$$

In this equation V is the applied voltage between anode and cathode, r the radius from the center of the anode wire, a the anode wire radius and b the cathode inner radius (see also Figure 17).

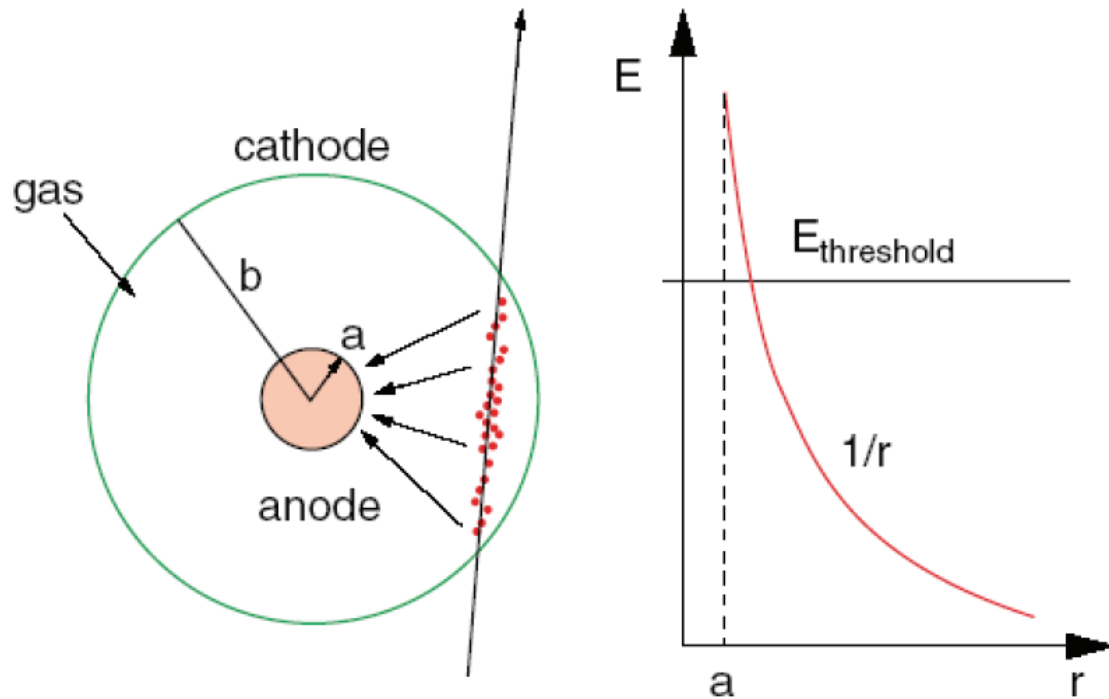


Figure 17: Electric field distribution in a straw tube [38]

Avalanche Formation

For gas amplification the electric field strength must be high enough (10^4 - 10^5 V/cm) so that the electrons formed through the primary ionization process can gain enough kinetic energy (between two collisions) to be able to ionize other atoms or molecules in the gas. In an increased electric field, the electrons are accelerated and produce secondary ionization in an avalanche process. A gain, or gas multiplication, of 10^3 to 10^5 is then possible with a produced signal proportional to the original ionization.

The gas multiplication process has the form of a cascade, known as the Townsend avalanche, in which each free electron created in a collision can potentially create more free electrons by the same process. The fractional increase in the number of electrons per unit path length is described by the Townsend equation [34]:

$$\frac{dn}{n} = \alpha dx$$

Here α is called the first Townsend coefficient for the gas and n the number of electrons. The average gas multiplication factor M characterizes the proportional counter operation. The solution of the Townsend equation (see equation above) in cylindrical geometry must take into account the radial dependence of the Townsend coefficient α caused by the

radial variation of the electric field strength. In general the mean gas amplification factor M can be written as [36]:

$$M = \frac{n}{n_0} = e^{\int_a^{r_c} \alpha(r) dr}$$

In this equation n represents the number of all ion pairs, n_0 the number of original ion pairs, r the radius from the center of the anode wire, a the anode wire radius and r_c the critical radius beyond which the field is too low to support further gas multiplication. The Townsend coefficient α is a function of the gas type and the magnitude of the electric field $E(r)$. Data on this dependence can be found in [39].

To achieve a uniform amplification for all ion pairs formed by the original ionization process, the region of gas multiplication must be limited to a very small volume compared with the total volume of the gas. Under these conditions, almost all primary ion pairs are formed outside the multiplying region, and the primary electron drifts towards that region where the multiplication takes place. Therefore each electron goes through the same multiplication process, independently from its position of formation. For this reason the multiplication factor will be the same for all original ion pairs.

The time development of the avalanche formation in a proportional counter can be described as follows (see Figure 18):

- a) A primary electron drifts towards the anode.
- b) The electron is accelerated in the strong electric field close to the wire in such a way that it can gain enough energy (between two collisions) to ionize further gas atoms or molecules. At this moment the avalanche formation starts.
- c) Electrons and positive ions are created in the ionization process essentially in the same place. The multiplication of charge-carriers comes to an end when the space charge of positive ions reduces the external electric field below a critical value. After the production of charge-carriers, the electron and ion clouds drift apart.
- d) The electron cloud drifts towards the anode wire and broadens slightly due to lateral diffusion. The density distribution of the secondary electrons around the wire depends on the occurrence of the primary ionization.
- e) The ion cloud recedes radially and drifts slowly towards the cathode.

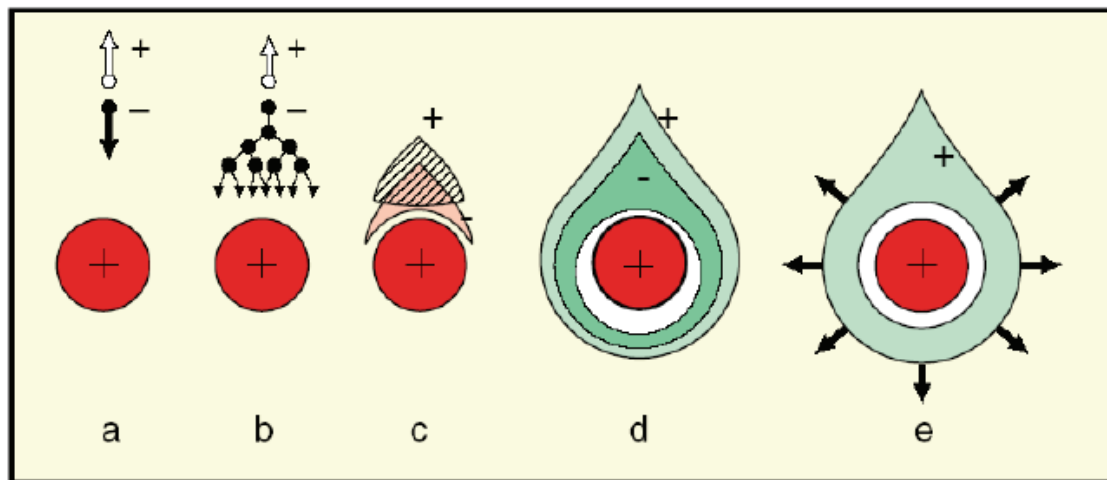


Figure 18: Temporal and spatial development of an electron avalanche [38]

Regions of Detector Operations

Figure 19 shows the different regions of operation of cylindrical gas detectors in pulse mode. The amplitude of the observed pulse from the detector is plotted versus the applied voltage or electric field within the detector. The five main operation regions are described as follows:

- I) Recombination before collection: At very low voltages the field is insufficient to prevent recombination of the original ion pairs, and the collected charge is less than that represented by the original ion pairs.
- II) Ionization chamber: With raising voltage, recombination is inhibited and the region of ion saturation is achieved. This is the normal mode of operation for ionization chambers discussed in chapter 2.3.1.
- III) Proportional counter: With further increased voltage the region at which gas multiplication begins is reached. Over some region of electric field, the gas multiplication is linear and the collected charge is proportional to the number of original ion pairs created through the incident radiation. This region represents the mode of operation of conventional proportional counters discussed in this chapter.
- IV) Region of limited proportionality: A further increase of the applied voltage leads to the formation of nonlinear effects. The reasons for this are positive ions which are also created in each secondary ionization process. The free electrons are collected rapidly at the anode wire but the positive ions move much slower towards the cathode. If the concentration of these ions is sufficiently high, they represent a space charge that can change the shape of the electric field within the chamber. Because further gas multiplication is dependent on the electric field, some nonlinearities will be observed. The pulse amplitude still increases with the increasing number of initial ion pairs, but not in a linear way.
- V) Geiger-Mueller counter: At sufficient high voltage the space charge created by the positive ions is dominating. Under these conditions, the avalanche proceeds until a sufficient number of ions have been created to reduce the electric field

below the point at which additional gas multiplication can continue. Therefore each output pulse from the detector will have the same amplitude and does not longer reflect the initial ionizing radiation. This is the mode of operation for Geiger-Mueller chambers, which are described in detail in [34, 35, 36].

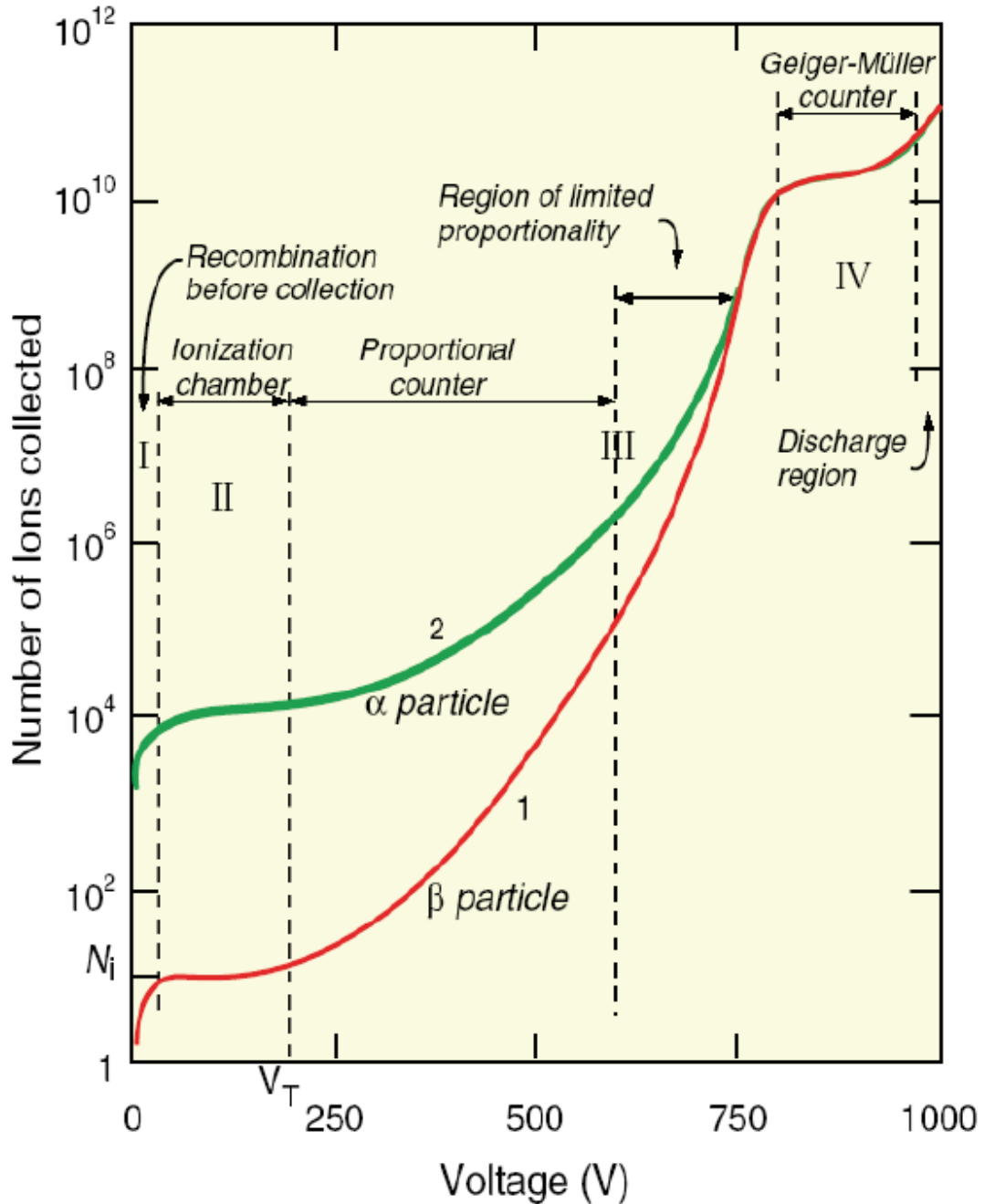


Figure 19: Characterization of modes of operation of cylindrical gas detectors [38]

2.4 Measurements of Position

2.4.1 Multiwire Proportional Chamber

In a multiwire proportional chamber (MWPC), the principle of a proportional counter (see section above) is applied to a detector with a large area. The advantage of this detector system is that large surface areas can be covered economically, for example, by placing a grid of anode wires between two cathode planes. Figure 20 shows the configuration of the electric field lines which results from such a type of MWPC. Avalanche formation in a MWPC proceeds exactly in the same way as in proportional counters.

A wide variety of MWPCs of different complexity has been constructed, tested, and applied successfully in experiments:

- Proportional and drift chambers of planar and cylindrical type. They provide one-dimensional measurements on a surface made by the parallel wires. The information is binary (on or off) or may contain pulse height; with drift time measured, the inter-wire distance can be subdivided, but left-right ambiguities are introduced. Planes at different angles or segmentation of the cathode allow one to obtain information along the wire.
- Jet and time projection chambers. These chambers are characterized by comparatively longer drift times; multiple sense wires can cover a large volume, and are usually equipped with multihit electronics, such that the passage of several tracks in the volume part associated with a wire can be recorded. These chambers give inherently two-dimensional information (the drift time is in a coordinate orthogonal to the wire plane). With added cathode instrumentation or charge division, three-dimensional points can be obtained.
- Time expansion chambers, a special type of drift chamber.

The main parameters of a wire chamber (from the viewpoint of optimizing particle detection) are:

- Single- and multihit detection efficiency.
- Precision and two track separation.
- Dead time.

The ATLAS – TRT MWPC consist of an array of single proportional counters, where each anode wire is placed in a cylindrical tube which functions as the cathode. The TRT detector is described in detail in chapter 1.2.5.

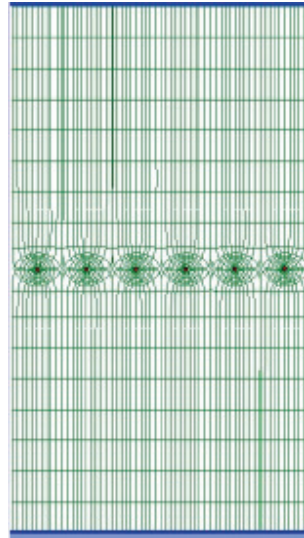


Figure 20: Electric field lines in a multiwire proportional chamber. A grid of anode wires are placed between two parallel cathode plates at the top and bottom of the figure [38]

2.5 Particle Identification

2.5.1 Transition Radiation Detectors

Transition radiation is produced by relativistic charged particles when they cross the interface of two media of different dielectric constants. This occurs if a charged particle passes a medium with varying dielectric constant, for instance a periodic series of foils and air gaps. The radiation is emitted from the interfaces between the two materials.

A charged particle moving towards a boundary layer forms together with its image charge in the denser layer an electric dipole. The electric field strength of this dipole varies while the particle approaches the boundary plane and vanishes upon its entry into the denser medium (see Figure 21). This variation in time of the dipole produces radiation.

The total energy loss of a charge particle on the transition depends on its Lorentz factor γ (see also chapter 1.2.5). The intensity of the emitted transition radiation is approximately proportional to the particles energy with an angle θ of emission which is inversely proportional to the Lorentz factor [34]:

$$\theta = \frac{1}{\gamma_{particle}}$$

Usually several layers of alternating materials or composites are used to collect enough transition radiation photons for an adequate measurement. For example, one layer of inert material followed by one layer of detector and so on. Counters measuring this transition

radiation can therefore be used in order to discriminate between particles of different mass but the same momentum by means of their γ factor

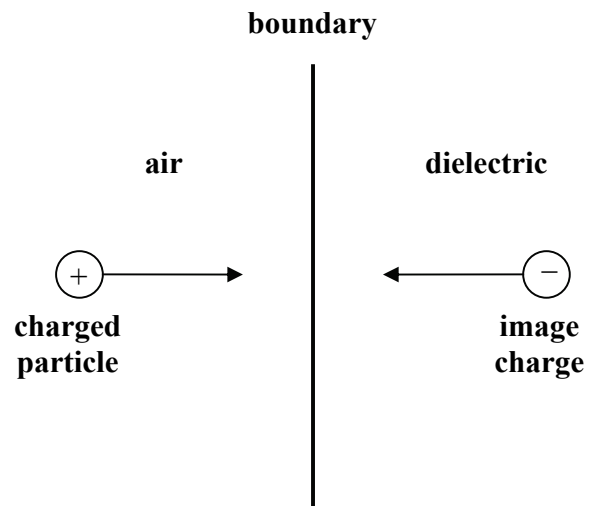


Figure 21: Illustration of the production of transition radiation at boundaries [34]

3 Plasma Chemistry of Organosilicon Compounds

3.1 Introduction

In the thin tube of plasma surrounding the anode wire, many complex physical and chemical phenomena are occurring simultaneously. The plasma chemical vapor deposition process involves the dissociation and/or chemical reaction of gaseous reactants (organosilicon compounds) in the plasma environment, followed by the formation of a stable solid product. The deposition involves homogenous gas phase reactions, which occur in the gas phase, and/or heterogeneous chemical reactions which occur on/near the vicinity of the anode wire leading to the formation of SiO_x films.

Dissociation and deposition are not understood clearly, however the general process can be specified as follows [40]:

- I) Formation of active gaseous organosilicon compounds through outgassing processes in the initially clean carrier gas (see also chapter 1.3.5).
- II) Transport of the gaseous species into the straw tube.
- III) Gaseous reactants undergo gas phase reactions forming intermediate species:
 - a) which undergo subsequent decomposition and/or chemical reaction, forming powders and volatile by-products in the gas phase. The powder will be collected on the wire surface and can act as crystallization center, at the same time the by-products are transported out of the straw tube with the gas flow. The deposited film may have poor adhesion.
 - b) and diffusion/convection of the intermediate species across the boundary layer (a thin layer close to wire surface) occur. These intermediate species subsequently undergo steps IV – VII.
- IV) Absorption of gaseous reactants onto the wire surface, and the heterogeneous reaction occurs at the gas–solid interface (i.e. wire surface) which produces the deposit and by-product species.
- V) The deposits will diffuse along the wire surface forming the crystallization centre and growth of the film.
- VI) Gaseous by-products are removed from the boundary layer through diffusion or convection.
- VII) The not reacted gaseous precursors and by-products will be transported out of straw tube with the gas flow.

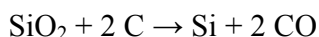
In the following chapters the key steps involved in the plasma chemical deposition process of organosilicon compounds in wire chambers will be described in detail.

3.2 Chemical Precursors – Organosilicon Compounds

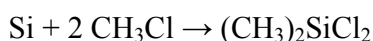
It is shown in chapter 5 and has often been reported [14, 21, 22, 24, 28, 30, etc] that the presence of volatile organosilicon impurities in the working gas of wire chambers lead to the formation of anode wire deposits. The properties, composition and usage of these aging precursors are discussed in detail below.

Silicon is, after oxygen, one of the most frequent elements on earth. It does not occur free in nature, but as an oxide (silica) or silicate (feldspar) in sand, rock and clay. Silicones, or polysiloxanes, are synthetic polymers consisting of a silicon-oxygen backbone (...-Si-O-Si-O-Si-O-...) with side groups attached to the silicon atoms. Certain organic side groups can be used to link two or more of these -Si-O- backbones together. By varying the -Si-O- chain lengths, side groups, and crosslinking, silicones can be synthesized into a wide variety of materials. They can vary in consistency from liquid to gel to rubber to hard plastic. The most common type is the linear polydimethylsiloxane or PDMS. The second largest group of silicone materials is based on silicone resins, which are formed by branched and cage-like oligosiloxanes

The basic raw material for the silicon production is quartz (SiO₂). A method of preparation is heating quartz sand together with carbon [40], which gives carbon monoxide and raw silicon (98 % pure). The 2 % impurities consist usually of Fe, Ca or Al.



A well known common method for preparing polysiloxanes is the direct reaction between silicon and methylchloride which gives dichlorodimethylsilane [41].



Hydrolysis of dichlorodimethylsilane (CH₃)₂SiCl₂ gives rise to straight chain polymers and, as an active OH group is left at each end of the chain, polymerization continues and the chain increases in length. (CH₃)₂SiCl₂ is therefore a chain building unit. The basic reaction sequence is represented as:



The result of this reaction are PDMS oligomers [(CH₃)₂SiO]_n. This is the favored route although other raw materials such as alkoxy silanes or alkyl/aryl substituted chlorosilanes can be used. The progress of conversion is called polymerization and silicon polymers occur in a broad diversity of utilization. Molecular weight and the structure of the polymer chain (straight, ramified, crosslinked) determine the thermodynamic properties of the resulting materials.

Silicone *fluids* are usually straight chains of PDMS. They are water insoluble and may be further modified with the addition of organofunctional groups at any point in the polymer chain.

Silicone *gels* are lightly cross-linked PDMS fluids, where the cross-link can be introduced through a trifunctional silane (e.g. CH_3SiCl_3). This produces a three-dimensional network that can be swollen with PDMS fluids to give a sticky, cohesive mass without form.

Silicone *elastomers* are cross-linked fluids whose three-dimensional structure is much more complicated than that of gels. In addition, there is a little amount of free fluid in the matrix. Fillers, such as amorphous silica, are frequently added to the matrix to give greater reinforcement to the network and thereby increase the strength of the product.

Silicone *resins* are more heavily cross-linked polymer networks. The physical properties of the finished silicone resin can be tailored to suit many applications by varying the ratio of branched and linear siloxanes and also the functional groups attached to the silicon.

Polysiloxanes have a wide variety of applications in vacuum systems, such as lubricants, adhesives, sealants, gaskets and many other materials. Due to their thermal stability and relatively high melting and boiling points, silicones are often used where organic polymers are not applicable. Through their low vapor pressure they can easily pollute an initially clean gas mixture by outgassing processes. These pollutants can further have dramatic effects on the lifetime of radiation detectors. Detailed information about outgassing processes can be found in chapter 1.3.5.

3.3 Thermodynamics, Kinetics and Mass Transport

The analysis of the deposition processes in wire chambers includes the understanding of the thermodynamics, chemical kinetics and mass transport phenomena. It is a complex chemical system and the following sections describe some methods for analyzing these phenomena.

Thermodynamics

Crystallization in general constitutes a phase change. A phase change occurs if the Gibbs free energy of the system is reduced. The feasibility of a reaction can be determined by calculating the Gibbs free energy ΔG_r of the reaction for the given temperature and pressure. The Gibbs free energy of reaction, ΔG_r , is the difference between the free energy of formation, ΔG_f , of the individual species of the reactants and the products:

$$\Delta G_r = \Delta G_f(\text{prod}) - \Delta G_f(\text{react})$$

The free energy of formation, ΔG_f , of an individual species, at a temperature T , can be determined by using the following equation:

$$\Delta G_f(T) = \Delta H_f^0(298) + \int_{298}^T c_p dT - TS^0(298) - \int_{298}^T \frac{c_p}{T} dT$$

Here ΔH_f^0 is the enthalpy of formation, S^0 the standard entropy and c_p the heat capacity at the temperature T .

A reaction will occur when ΔG_r is negative. Under certain circumstances where there are several possible reactions, which are all thermodynamically feasible, the kinetics determines which route is taken. Generally the reaction with the most negative ΔG_r value will dominate as it has the most stable reaction products.

Mass Transport

The mass transport phenomena include:

- transport of the impurities from the outgassing place into the straw tube by fluid dynamics (fluid flow, mass transfer, heat transfer), and
- mass transport of impurities close to the wire surface, diffusion through the boundary layer on the wire surface, desorption of the by-products from the wire surface and transport of the by-products out of the straw tube.

Basic fluid-mechanic concepts can be applied to describe the fluid flow and mass transfer in the gas phase. The fluid flow can be characterized by several dimensionless parameters such as the Reynolds number (Re) and Knudsen number (Kn) which are described in more detail in chapter 7.1.3. Re defines the limit between the laminar and turbulent flow regimes, whereas Kn defines the limits between laminar, Knudsen and molecular flow.

Other dimensionless parameters that are important in the characterization of the transport processes are Prandtl, Schmidt, Grashof, Peclet and Damkohler numbers [42]. For examples, the Rayleigh and Grashof numbers indicate the strength of natural convection in a system, the Peclet number predicts any diffusion of downstream impurities into the deposition zone and the gas-phase Damkohler number estimates the reactant residence time.

The deposition rate is dependent on the concentration of reactants, thickness of the boundary layer and diffusivity of active species. These factors are influenced by the temperature, pressure, gas flow rate, geometry, etc. There are many different definitions of the boundary layer existing in the literature. The basic approach is to define it as the distance where the velocity of gas increases from zero at the wire surface to the bulk value.

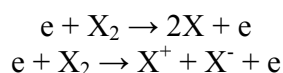
3.4 Gas Phase Reactions forming Intermediate Species

3.4.1 Formation of Intermediate Species

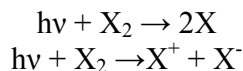
Unintentional contaminants (organosilicon compounds) can significantly modify the chemistry occurring in the thin tube of plasma surrounding the anode wire.

In general, gas phase reactions generate reactive chemical species while surface reactions result in deposit formation. The creation of molecular fragments in the plasma is therefore a necessary precursor for wire aging. In the gas phase, collisions of neutral molecules with high energy electrons and heavy particles (ions or neutrals) or photon absorption results in the generation of molecular fragments. “Generic” reactions for these processes are indicated in the equations below, where X_2 represents any molecular chemical species, and B represents an ion, molecule or atom [43].

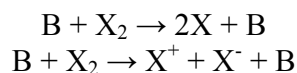
Electron impact collisions



Photon exposure



Heavy particle collisions



Generally $E_{\text{Thermal_Dissociation}} < E_{\text{Electron_Dissociation}} < E_{\text{Ionization_Energy}}$. The electrons in the plasma around the anode wire have a broad distribution of energies with an average of a few electron volts (see Figure 22). The avalanche is probably too short to create thermal dissociation and the electron energy is somewhat less than that required for ionization. Ionization results from the few electrons on the upper end of the energy spectrum above the ionization threshold. Electron impact dissociation might be therefore the dominating mechanism for molecular fragment formation. In Table 5 dissociation and ionization energies are summarized for some selected gases.

Table 5: Dissociation and ionization energies for some selected gases [22]

Compound	Dissociation Energy [eV]	Ionization Energy [eV]	Comment
H	-	13.6	
Ar	-	15.8	
Xe	-	12.1	
H ₂	4.5	15.4	
N ₂	9.8	15.6	
O ₂	5.2	12.1	
Cl ₂	2.6	11.5	
CO	11.2	14.0	
NO	6.5	9.2	
H-CH ₃	4.6	12.6	
H-CH ₂	4.8	9.8	
H-C	3.5	11.1	
H-C ₂ H ₅	4.3	11.5	
H-iC ₃ H ₇	4.2	11.1	
H-iC ₄ H ₉	4.0	10.6	
H-C ₆ H ₅	4.8	9.2	
H-OH	5.2	12.6	
H-CH ₂ OH	4.1	10.8	Methanol
H-CH(CH ₃)OH	4.0	10.5	Ethanol
H-CH ₂ OCH ₃	4.0	10.0	Dimethylether
HO-iC ₃ H ₇	4.0	10.2	Isopropanol
C ₆ H ₁₈ OSi ₂	4.5	9.6	Hexamethyldisiloxane

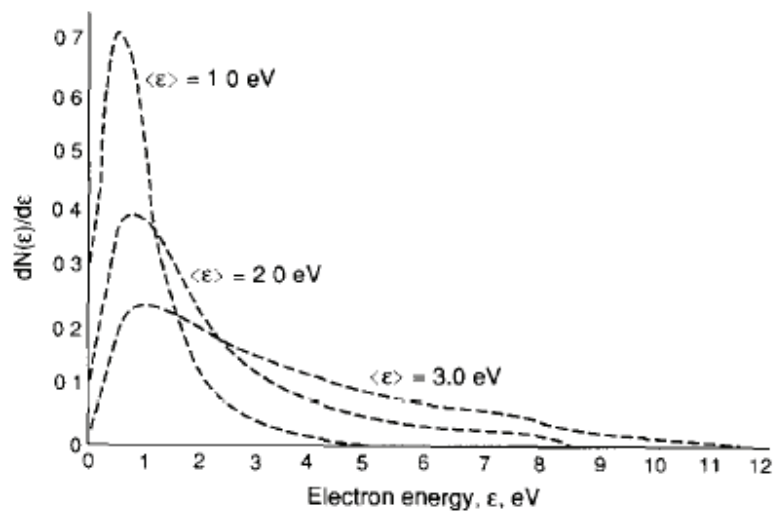


Figure 22: Typical electron energy distribution in a plasma [22]

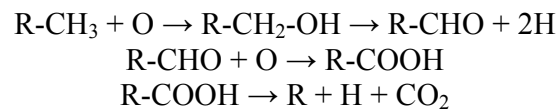
3.4.2 Plasma Chemical Processes

While the specific reactions in wire chamber aging are extremely complex, some qualitative approach to aging phenomena can be obtained from similarities with processes in plasma chemical vapor deposition.

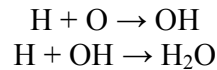
Plasma enhanced chemical vapor deposition (PECVD) of organosilicon compounds as precursor is widely used in the microelectronics industry to deposit dielectric materials such as silicon dioxide (SiO_2). Intensive studies have been performed to understand the plasma chemical mechanisms, see for example [44, 45, 46, 47, 48]. These studies focus on the species in vapor phase whereby the reactions on the surface which will complete the SiO_2 networking are not understood clearly and need further investigations. It has been shown in [44] and [45] that the ratio of O_2 over the organosilicon precursor is a key parameter to control the deposition properties. Large amounts of high molecular intermediate products are present in O_2 free plasmas, while they disappear with higher partial pressure of O_2 against the organosilicon precursor, representing the promotion of dissociation by added O_2 . Signal intensity of H_2 decreases, while signals from oxides such as H_2O and CO_2 increases remarkably with increasing O_2 . From these results it can be concluded that added O_2 promotes the dissociation of intermediate products and that eliminated hydrocarbon gases are converted into oxides which are readily pumped out. In O_2 containing plasmas, intermediate products which are initially produced by electron impact react with O atoms or O_2 eliminating alkyl groups and OH radicals. As a result of such oxidation in vapor phase the deposited films show lower concentrations of hydrogen and carbon. In [48] it has been reported that O_2 is not capable of etching the silicon oxide matrix in the deposited film, but it is able to reduce the amount of hydrogen and carbon atoms present in the film.

A surprising decrease of the Si-O-Si concentration, in a hexamethyldisiloxane/ O_2 /Ar plasma with increasing O_2 concentration has been reported in [47]. One would expect an increase of the Si-O-Si concentration in the plasma, which could be the starting point for generating long chains of Si-O-Si to finally produce quartz-like films. In addition an increase of oxygen in the deposited films has been observed. This proves that the polymerization process takes place mainly at the surface and not in the bulk plasma and that oxygen dissociates the organosilicon precursor with high efficiency. Thus volume plasma processes are only preparing the activated radicals needed for deposition.

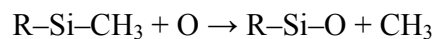
Applying the knowledge from PECVD to aging phenomena we can form a rough model of the plasma chemical reactions in wire chambers. As specified in chapter 5, the aging causing impurities in the TRT are polyorganosiloxanes, most commonly polydimethylsiloxanes. For the model let us assume that the active TRT working gas ($\text{Xe}/\text{CO}_2/\text{O}_2$) is polluted with a low concentration of pentamethyldisiloxane (PMDS). Electron impact collisions dissociate the PMDS impurities into fragments. These fragments further react with oxygen. The methyl group can react in the well-known oxidation scheme:



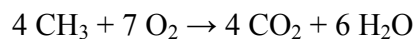
The atomic hydrogen also reacts with oxygen:



Si-CH₃ can also react with oxygen a possible reaction scheme can be for example:



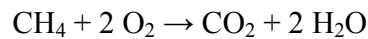
CO₂ and H₂O are end products in the oxidation pathways and they will be readily pumped out of the straw. CH₃, Si-CH₃ and R-Si-O are start products of further reactions. CH₃ can be either oxidized,



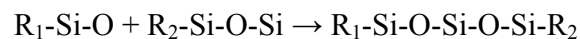
or react with H which is produced in previous oxidation steps:



Thus methane is an indirect product of the oxidation, which either leaves the straw with the current gas flow or oxidizes:



As proven in [47] and mentioned above, the following expected reaction doesn't occur in the plasma:



This leads to the conclusion that SiO₂ polymerization is a solely surface process. The surface reactions mechanisms forming the deposits are not fully understood. However, the deposit composition on the wire surface depends strongly on the O₂ content in the gas mixture, on the exposure time and on the current density. Higher O₂ concentrations, longer exposure times and higher current densities are leading to purer SiO₂ deposits.

3.5 Deposition Mechanisms

During the deposition process, chemical reactions can occur in the gas phase or near the vicinity of the anode wire surface.

The reactions in the gas phase lead to the homogenous nucleation of solid from the gas phase. This results in the formation of stable solid reaction product in the form of fine powder. The powder that nucleated from the gas phase will deposit onto the wire surface and lead to a powdery coating with irregular structure and poor coating adhesion. This reaction mechanism occurs preferred at high impurity concentration and high deposition temperatures.

Heterogeneous reactions near the vicinity of the wire surface result in the adsorption of mobile atoms/monomers on the wire, which diffuse to the preferred sites to form germs and stable nuclei. As the impurity level in wire chambers is very low and the working temperature is ambient this deposition mechanism will be dominating. Growth will occur by the addition of adsorbed monomers to sites with lowest free energy such as kinks and ledges to form crystallites. A thin crystal is formed upon coalescence. Heterogeneous reactions can lead to the formation of various structures, depending on precursor concentration and surface temperature, like epitaxial, polycrystalline, whiskers or amorphous.

4 Technology of Gas Separation

4.1 Introduction

In chemical engineering a separation process is defined as a process that transforms a mixture of substances into two or more compositionally distinct products. There are many different types of separation processes e.g. filtration, chromatography, distillation, extraction, cryogenic, adsorption and lots more. To choose the right separation method for the required task is an important supposition for high separation efficiency. Therefore it is necessary to have a clear picture of the system parameters (e.g. temperature, pressure, concentration, mass flow, etc.) and the thermodynamic data of the involved substances.

4.2 Composition and Thermodynamic Data of Impurities

Through outgassing processes of organosilicon compounds as specified in chapter 1.3.5 the initially clean working gas mixture of the TRT gets polluted. These pollutants are causing wire deposits and thereby detector performance degradation. To guarantee a 10 year lifetime of the TRT detector these impurities need to be separated from the working gas mixture. In order to select the most appropriate separation method, it is indispensable to make a careful analysis of the system parameters and clearly identify the requirements.

Table 6 represents some selected TRT gas system parameters. The organosilicon impurity level is expected to be below 1 ppb (see chapter 7.2) and as shown in chapter 5 the main substance of hazardous impurities is polymethylsiloxane. Therefore some thermodynamic data of polydimethylsiloxane (PDMS), pentamethyldisiloxane (PMDS) and hexamethyldisiloxane (HMDS) are summarized in Table 7 [49]. The chemical structure of PMDS and HMDS are shown in Figure 23 and Figure 24 respectively [49]. In Figure 25 the calculated vapor pressure of HMDS is plotted versus the temperature, whereby the calculation has been performed by applying the Antoine equation [49].

In general organosilicon compounds are liquid at room temperature and have a vapor pressure of about 100mbar.

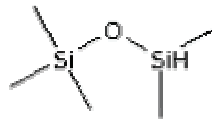


Figure 23: Chemical Structure of PMDS

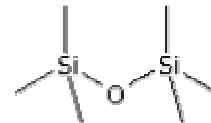


Figure 24: Chemical Structure of HMDS

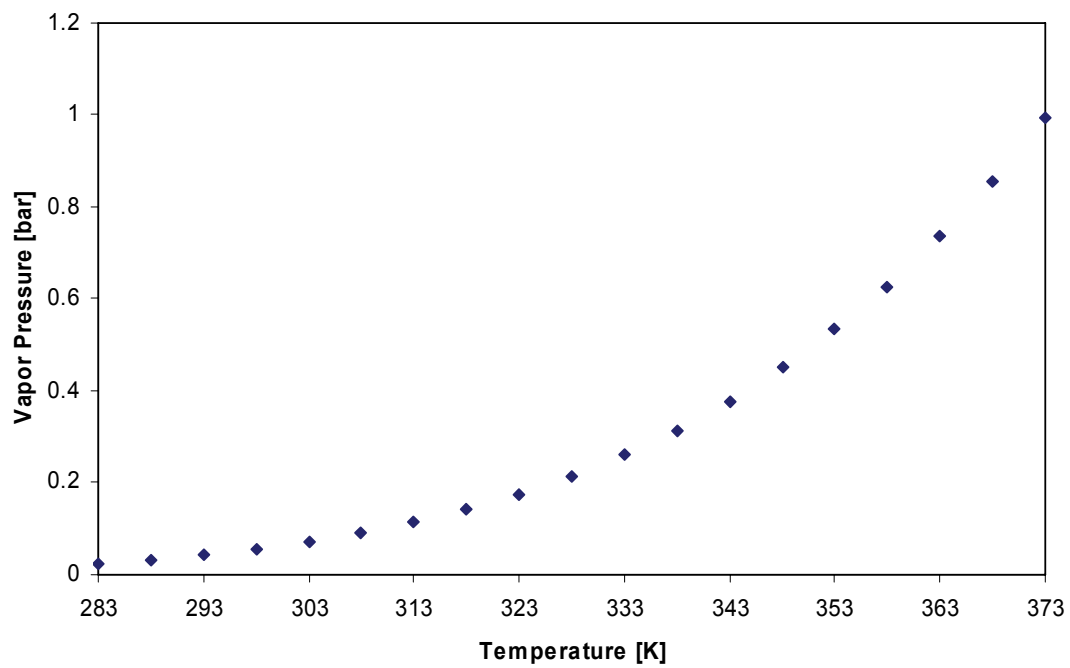


Figure 25: Vapor Pressure of HMDS calculated with Antoine Parameters

Table 6: Some selected TRT gas system parameters

flow rate [m ³ /h]	3
temperature [K]	293
pressure [bar]	1
gas composition	
Xe [Vol%]	70
CO ₂ [Vol%]	27
O ₂ [Vol%]	3

Table 7: Thermodynamic data of some organosilicon compounds

Name	PDMS	PMDS	HMDS
Formula	C ₂ H ₆ OSi ¹	C ₅ H ₁₆ OSi ₂	C ₆ H ₁₈ OSi ₂
Molecular Weight	74.2 ²	148.4	162.4
C _{p, Liquid} [J/molK]	154.6	-	311.4
T _{Boil} [K]	-	359	373

4.3 Purification Principles for Volatile Organic Compounds

There exist some different techniques of gas purification that can be employed for the TRT system. The simplest and most appropriate has to be selected. From the data summarized in the previous chapter, three different methods which will meet the requirements can be applied. The different principles (cryogenic distillation, catalytic conversion, adsorption) are described in detail below.

4.3.1 Cryogenic Distillation

Cryogenic distillation is a process used to separate two or more gases which have different condensing points. This happens by dropping the temperature of the gas mixture till one gas fraction will reach its condensing point and liquefies, while the other will remain gaseous.

This principle can be applied to separate organosilicon compounds from the TRT working gas mixture Xe/CO₂/O₂. Therefore the gas mixture has to be cooled down from room temperature to about -20 to -70 °C. The finally condensation temperature of a certain organosilicon compound depends on its concentration level and thermodynamic data. The working gas components will liquefy later, whereby CO₂ condenses first at about -80 °C.

4.3.2 Catalytic Conversion

Catalytic processes used in gas purification differ from the techniques discussed in chapter 4.3.1 and 4.3.3 in that the objectionable impurities are not physically removed from the gas stream, but converted to compounds which are not objectionable anymore and remain in the gas stream. The field of chemical catalysis is extremely complex and to discuss it would go far beyond the scope of this work. However, extensive information about catalysis can be found in various textbooks [50, 51, 52].

Catalysis is based on the fact that the rate of certain chemical reactions is influenced by the presence of substances which remain unchanged in the reaction products. Catalysts

¹ Monomer Formula

² Monomer Molecular Weight

may increase (positive catalysis) or decrease the rate of reaction (negative catalysis), or direct the reaction along a specific path. Depending on the phase relationship between the catalysts and the initial reactants, catalytic processes may involve homogeneous and heterogeneous catalysis. Homogeneous catalysis is characterized by the fact that the catalyst and the reactants are in the same phase, while in heterogeneous catalysis the catalyst and the reactants are in different phases. Catalytic gas purification processes utilize positive, heterogeneous catalysis.

Ideally catalysts could be used for an indefinite period of time as they don't participate in the reaction process. In practice most catalysts deteriorate or are gradually deactivated during operation, and have to be regenerated or replaced periodically.

Vapor phase catalytic oxidation and reduction can be used for the removal of a large variety of objectionable compounds from many types of gas streams. Catalytic oxidation is particularly suitable for removing small amounts of combustible contaminants from gas streams containing these compounds in concentrations below the flammable limit. Oxidation catalysts most commonly used in gas purification are platinum or palladium supported on various carrier materials. These catalysts are effective over a wide range of temperature, pressure, concentration and combustible compounds. Minimum temperatures for initiation of catalytic oxidation of aliphatic and aromatic hydrocarbons are shown in [53]. These values vary significantly with space-velocity, catalyst activity, hydrogen and oxygen concentrations. However, they are a useful reference quantity for estimating the gas temperature required for a catalytic-converter.

The removal of hydrocarbons and organosilicon compounds from the TRT working gas mixture (Xe/CO₂/O₂) by catalytic oxidation is feasible. The oxygen concentration is 3 Vol.% which is more than enough for an expected impurity level of maximum 1 ppb (see 7.2). Tests with a platinum wool catalyst at a gas temperature of 300 °C have been performed and were successful (see chapter 7.3.1).

Table 8: Minimum temperatures for initiation of catalytic oxidation of hydrocarbons

Compound	Initiation Temperature [°C]
Methane	404
Ethane	360
Propane	343
n-Butane	299
n-Pentane	310
n-Hexane	332
n-Heptane	304
n-Octane	254
n-Decane	260
n-Dodecane	282
n-Tetradecane	288
Benzene	227
Toluene	238
o-Xylene	243

4.3.3 Adsorption

This gas purification method has been selected for the TRT gas system. The advantages of the removal of objectionable impurities by adsorption are that the working temperature is ambient and that no additional heat or power is required.

A detailed description of gas separation by adsorption processes can be found in chapter 4.4.

4.4 Gas Separation by Adsorption Processes

4.4.1 Fundamentals of Adsorption

In adsorption, materials are concentrated on the surface of a solid as a result of attractive interaction between the molecules to be adsorbed and the solid surface. Atoms on the surface of a solid experience a bond deficiency, because they are not wholly surrounded by other atoms. When the solid is exposed to a gas, the gas molecules will form bonds with it and become attached. There are two main kinds of interactions holding adsorbed molecules to the surface, physical or chemical, and therefore we distinguish between physical (or “van der Waals”) adsorption and chemisorption. In physisorption the adsorbate adheres to the surface only through weak intermolecular interactions, whereby in chemisorption a molecule adheres to a surface through the formation of a chemical bond. Physisorption is characterized by low temperature, low activation energy and low enthalpy as opposed to chemisorption which is characterized by high temperatures, high activation energy and high enthalpy. Chemisorption is less dominant in adsorption processes.

The quantity of material adsorbed is directly related to the area of surface available for adsorption and therefore adsorbents generally are prepared to have a very large surface area per unit weight. The material adsorbed by the solid (the adsorbent) is termed the adsorbate, in contradistinction to the adsorptive which is the general term for the material in the gas phase which is capable of being adsorbed. The fundamental terms of adsorption are shown in Figure 26.

The most common theory to describe adsorption processes is that of Langmuir [54] which considers monolayer adsorption. When adsorption starts a large number of active sites exists and the number of molecules adhering exceeds the number of those leaving the surface. As the surface becomes covered, the probability of a molecule in the gas phase finding an unoccupied space decreases, until finally the rate of condensation equals the rate of evaporation which represents the condition of equilibrium.

In the Langmuir model, it is assumed that adsorption could only occur on the unoccupied substrate adsorption sites. If the initial adsorbed layer can act as a substrate for further adsorption then the amount of layers can be expected to rise indefinitely. The most widely used isotherm dealing with multiplayer adsorption is described by Brunauer-Emmett-Teller and is called the BET isotherm [54].

The Langmuir and BET isotherm are described in further detail in chapter 4.4.3. Although adsorption can be practiced with many porous materials this work will focus on the adsorption of organic compounds on zeolite materials (see chapter 4.4.9).

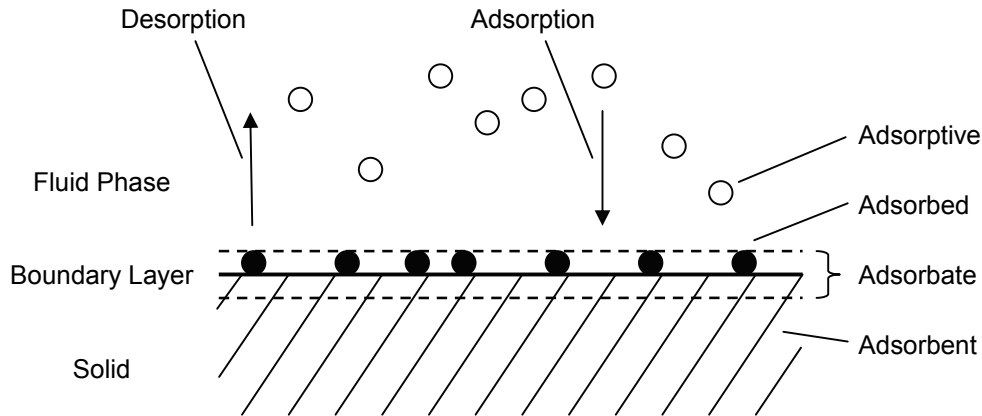


Figure 26: Fundamental terms of adsorption

4.4.2 Characterization of Adsorbents

The most important characteristic of an adsorbent is its high porosity and its high surface area. The microporous structure of the adsorbent can be characterized by standardized techniques. Important physical characteristics are pore volume, pore size distribution and surface area. Also of practical importance are bulk density, crush strength and erosion resistance.

The surface area of an adsorbent can be determined by the Brunauer-Emmett-Teller (BET) method, which is widely used in surface science for the calculation of surface areas of solids by physical adsorption of gas molecules [55]. The concept of the theory is based on multilayer adsorption with the following hypotheses:

- gas molecules physically adsorb on a solid in layers infinitely
- there is no interaction between each adsorption layer
- the Langmuir theory can be applied to each layer.

The resulting BET equation is defined as:

$$\frac{1}{v \left[\left(\frac{P_0}{P} \right) - 1 \right]} = \frac{1}{v_m c} \left(\frac{P}{P_0} \right) + \frac{1}{v_m}$$

Where P and P_0 are the equilibrium and the saturation pressure of the adsorbate at the temperature T , v is the adsorbed gas quantity, and v_m is the monolayer adsorbed gas quantity. c is the BET constant, which is expressed by the following equation:

$$c = e^{\left(\frac{E_1 - E_L}{RT}\right)}$$

E_1 is the heat of adsorption for the first layer, E_L is that for the second and higher layers and is equal to the heat of liquefaction, R is the ideal gas constant and T the temperature. The total surface area S_{total} and the specific surface area S are determined by:

$$S_{total} = \left(\frac{v_m N s}{M}\right)$$

$$S = \frac{S_{total}}{a}$$

Here, N is the Avogadro number, s the adsorption cross section, M the molecular weight of the adsorbate and a is the weight of the solid sample.

In characterizing the pore volume, both total pore volume and its distribution over the pore diameter are needed. The total pore volume is usually determined by helium pycnometry and mercury density. Helium gives the total voids, because of its small atomic size and negligible adsorption, whereas mercury gives the inter-particle voids because it does not penetrate into the pores at ambient pressure. The total pore volume is the difference between the two voids. The pore size distribution can be measured by mercury porosimetry and by N_2 desorption (or adsorption).

For the helium pycnometer the adsorbent to be measured is placed in a cell of known volume [56]. This cell is pressurized, using helium, to an exactly measured pressure. Then a valve between the sample cell and a reference cell of known volume is opened and the helium from the pressurized chamber is transported to the reference cell. The subsequent pressure in the system is measured. Using the ideal gas law, the sample volume can be calculated from the pressure ratio.

The mercury porosimetry is based on measuring the extent of mercury penetration into the evacuated solid as a function of the applied hydrostatic pressure [56]. The pore radius at a given pressure is given by:

$$r = -\frac{2\sigma \cos \Theta}{P_L - P_G}$$

Where r is the pore radius, P_L the liquid pressure, P_G the gas pressure, σ the interfacial tension and Θ the contact angle.

Since the technique is usually done under vacuum, the gas pressure becomes zero. The contact angle of mercury with most solids is between 135° and 142° , so an average of 140° can be taken without much error. The surface tension of mercury at 20° C under vacuum is 0.48 N/m. With the various substitutions, the equation becomes:

$$r = \frac{7500}{P_L}$$

In this equation the units of P_L are in atmospheres and that of r in Å.

The N₂ desorption (or adsorption) technique is based on the phenomenon of capillary condensation. It occurs at a relative pressure below unity because the equilibrium vapor pressure P over a concave meniscus is lower than the pressure P_0 over a plane surface. This is expressed by the Kelvin equation:

$$\ln \frac{P}{P_0} = - \frac{2\sigma V_m \cos \Theta}{r_K RT}$$

Here σ is the interfacial tension, Θ the contact angle ($\Theta = 0$ for N₂), V_m the liquid molar volume, r_K the radius of the curvature (Kelvin radius), R the ideal gas constant and T the absolute temperature.

From the measurement of an adsorption or desorption isotherm, the pore size distribution of the adsorbent can be calculated by applying the Kelvin equation.

4.4.3 Adsorption Equilibrium

Models or correlations for gas adsorption are crucial for the design of adsorptive gas separation processes. The theories should be capable of predicting the equilibrium amount adsorbed within a given range of operating temperature and total pressure. The most common methods to describe the adsorption equilibrium are the Langmuir and the BET isotherm.

The Langmuir Isotherm

For molecules in contact with a solid surface at a fixed temperature the Langmuir isotherm describes the partitioning between gas phase and adsorbed species as a function of applied pressure [54]. It is the simplest and most useful isotherm, which is based on the following assumptions:

- a) Adsorption cannot proceed beyond monolayer coverage.
- b) All surface sites are equivalent and can accommodate, at most, one adsorbed atom.
- c) The ability of a molecule to adsorb at a given site is independent of the occupation of neighboring sites.

The adsorption process (see Figure 28) between gas phase molecules, A, vacant surface sites, S, and occupied surface sites, SA, can be represented by the equation:



The equilibrium constant, K , can be defined as:

$$K = \frac{k_a}{k_d} = \frac{[SA]}{[S][A]}$$

With rate constants k_a for adsorption and k_d for desorption. The surface coverage, θ , can be written as:

$$\theta = \frac{N}{S_0}$$

Where N is the number of adsorbed molecules and S_0 the total number of surface sites. At equilibrium, the coverage is independent of time and thus the adsorption and desorption rates are equal. If we assume that,

- [SA] is proportional to the surface coverage, θ , of adsorbed molecules
- [S] is proportional to the number of vacant sites $(1 - \theta)$
- [A] is proportional to the gas pressure P

we can define the equilibrium constant, b :

$$b = \frac{\theta}{(1 - \theta)P}$$

Rearrangement of this equation gives the expression for the surface coverage:

$$\theta = \frac{bP}{1 + bP}$$

The rate of change of the surface coverage due to adsorption is:

$$\frac{d\theta}{dt} = k_a S(1 - \theta)P$$

The rate of change of the coverage due to desorption is proportional to the number of adsorbed species:

$$\frac{d\theta}{dt} = -k_d S\theta$$

The graphical form of the Langmuir isotherm is shown in Figure 27, where $b_3 > b_2 > b_1$. b is only constant if the enthalpy of adsorption is independent of the surface coverage. The value of b depends on a number of factors like the gas temperature, the surface temperature and the gas pressure.

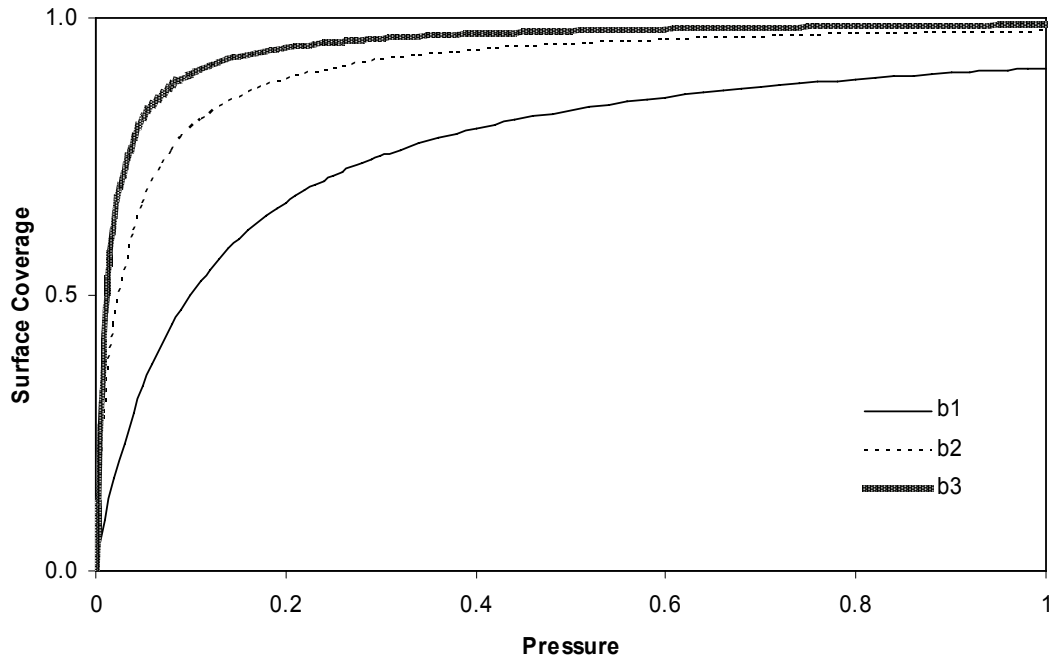


Figure 27: Graphical form of the Langmuir isotherm where $b_3 > b_2 > b_1$ [62]

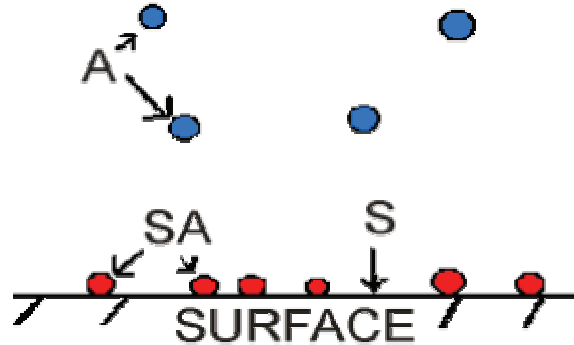
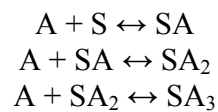


Figure 28: Adsorption process between gas phase molecules and adsorbent

The BET Isotherm

In the Langmuir model, it is assumed that adsorption can only occur on the unoccupied substrate adsorption sites. In the BET model this restriction is relaxed, and the initially adsorbed layer can act as a substrate for further adsorption. The proposed mechanism for multilayer adsorption is:



And so on where A is a gas molecule and S a surface site. A complete derivation of the BET isotherm can be found elsewhere [56], it is expressed as:

$$\frac{x}{V(1-x)} = \frac{1}{V_m c} + \frac{x(c-1)}{V_m c}$$

In this equation x is the ratio of P/P_0 (pressure to saturation pressure), V is the volume of adsorbed adsorbate, V_m is the volume of the amount of adsorbate required to form a monolayer and c is the equilibrium constant K used in Langmuir isotherm multiplied by the vapor pressure of the adsorbate.

The Langmuir isotherm is usually better for chemisorption and the BET isotherm works better for physisorption. Figure 29 shows the typical graphical form of the BET isotherm.

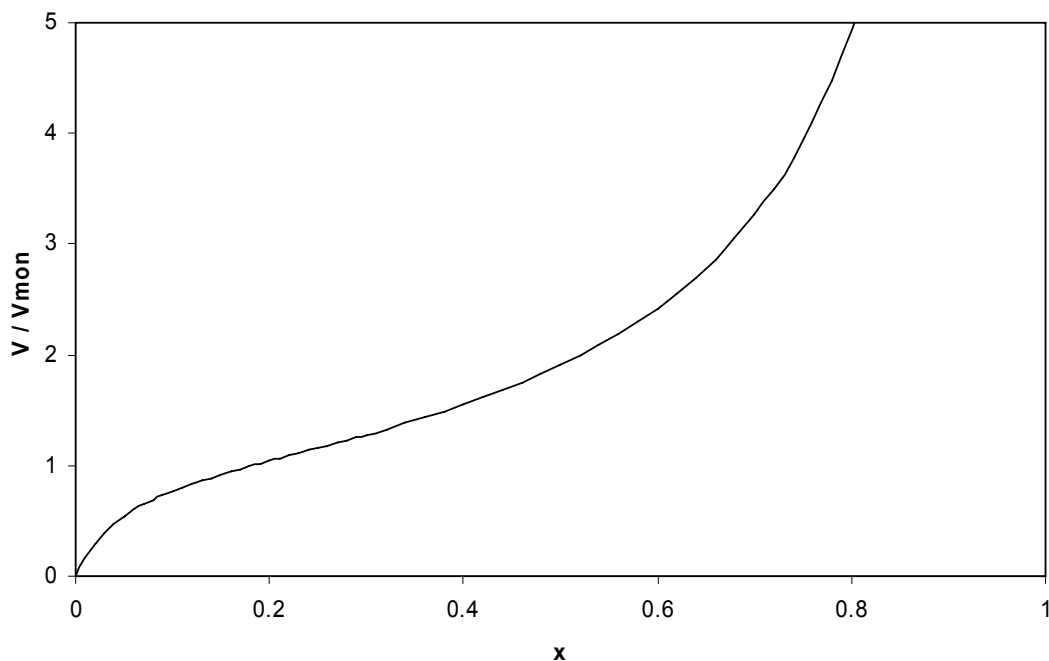


Figure 29: Graphical form of the BET isotherm [62]

4.4.4 Adsorption Kinetics

The transport of a gas molecule from the gas phase to an adsorption site inside the adsorbent particle is handicapped by the existence of transport resistances along the path. Bigger transport resistances require more time to reach equilibrium. Rate influencing factors are film diffusion, pore diffusion, surface diffusion and the combination of these mechanisms. The following transport resistances are recognized [57]:

- a) External gas film resistance outside the adsorbate particle. The mechanism for this transport is gas – gas diffusion.

- b) Diffusion resistance through the network of pores within the adsorbate particle. Simultaneous viscous and Knudsen diffusion through the adsorbate pores as well as surface diffusion of adsorbed molecules are mechanisms for this transport mode.
- c) Diffusion resistance through the micropores of the adsorbate to the adsorption sites. The transport mechanism is activated diffusion of adsorbed molecules from site to site.

In addition skin resistance at the surface of the adsorbent particle can occur. Skin resistance is created by the formation of a thin but denser layer of material at the surface during extrusion of a pellet and by hydrolysis during thermal regeneration processes.

A mathematical description of the adsorption kinetics of single component sorption requires the consideration of the transport mechanisms (film diffusion, surface diffusion, pore diffusion). For each transport mechanisms a set of equations can be established. The kinetic modeling of multi component sorption is based on the equations which have been developed for single component sorption. The adsorption kinetic of a complex multi component mixture with known composition can be determined in the same way as the adsorption equilibrium. A specific modeling of the adsorption kinetics will not be performed in this work as the kinetics is included in the adsorption dynamics (see chapter 4.4.5).

4.4.5 Adsorption Dynamics

Purification of gas mixtures by selective adsorption of one or more of its components on a solid adsorbent is most generally performed by using packed bed adsorbers.

Adsorption is a transient process and the amount of material adsorbed within a bed depends on position and time. When the gas containing the adsorptive enters the bed it comes in contact with the first few layers of adsorbent and starts to fill up some of the available sites. The adsorbent near the entrance gets saturated and the adsorptive penetrates farther into the bed. Thus the active region or the so-called mass transfer zone shifts up through the bed as time goes on. The gas emerging from the packed bed will be free of adsorptive. As the gas flow through the bed continues the mass transfer zone moves up the bed until breakthrough appears. At this moment the adsorptive concentration at the outlet is no longer zero and the ratio of c/c_0 becomes 1. The shape of the mass transfer zone depends on the adsorption isotherm (equilibrium expression), flow rate, and the diffusion characteristics in the packed bed. Its shape and width is crucially important for the design of adsorbers, whereby a sharp concentration front is desirable for high separation efficiency. Usually breakthrough curves must be determined experimentally (see chapter 7.3). The principle of a packed bed adsorber and the concentration front is shown in Figure 30. The adsorbents for such kind of adsorbers can be used in a form of powder, pellets, spheres or beads. The advantages of beads are their high bulk density, their low formation of fines and dust and their minimized pressure drop. Mechanical sieves at the inlet and outlet of the adsorber hold the adsorbents in the

reactor. The outlet sieve is also used to keep fines and dust back, which are resulting from ablation processes of the adsorbents.

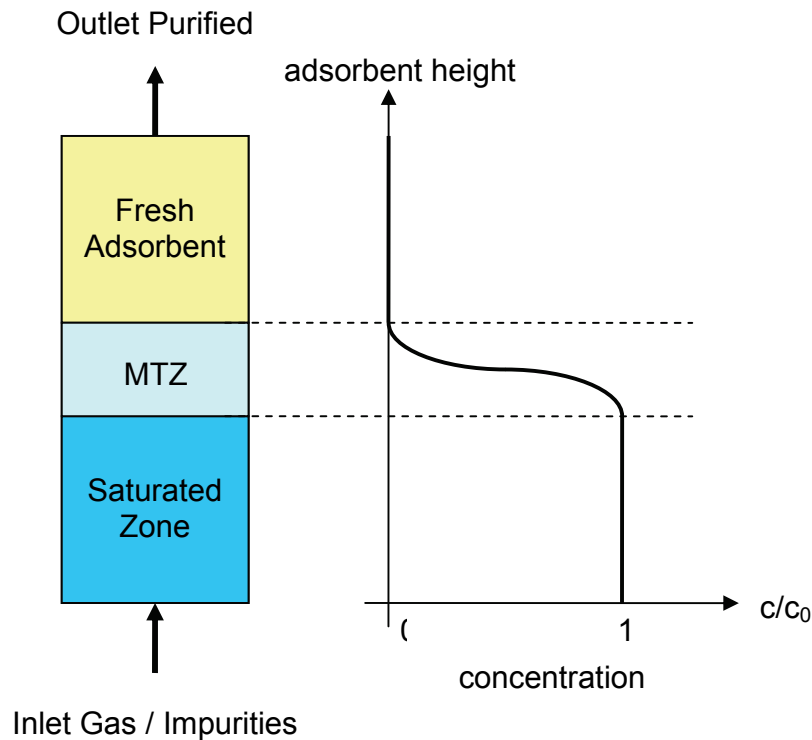


Figure 30: Mass transfer zone in a packed bed adsorber

4.4.6 Mass Balance of Packed Beds

The time dependent propagation of the mass transfer zone (MTZ) for a feed with constant concentration introduced at time zero into a clean packed bed is shown in Figure 31. The location of the MTZ at any time can be found through an overall mass balance and the form can be determined by breakthrough curves. Ideally the breakthrough curve would have the form of a step function and the difference between the breakthrough time, t_B , and the saturation time, t_S , would be zero. In reality the MTZ occurs in a S-form, whereby t_{MTZ} represents the unused bed volume. The value t_{MTZ} is the time the MTZ needs to propagate a distance corresponding to its own height.

The adsorber balance is required to determine the equilibrium adsorption capacity, a_0 , which is an important parameter for the dimensioning of packed beds. a_0 is defined as the ratio of adsorbate mass, m_s , and adsorbent mass, m_{ad} :

$$a_0 = \frac{m_s}{m_{ad}}$$

The packed bed mass balance can be written as:

$$m_{total} = m_s + m_{void}$$

Here m_{total} is the total stored adsorbate in the packed bed and m_{void} is the mass of adsorbate stored in the voids of the adsorbent. If we assume ideal adsorption with a step form of the MTZ, m_{total} can be expressed as follows:

$$m_{total} = c_0 \dot{V}_{feed} t_{id}$$

In the above equation c_0 is the sorbate feed concentration, \dot{V}_{feed} the feed volume flow and t_{id} the ideal breakthrough time.

The adsorbate mass stored in the voids of the adsorbent can be calculated as:

$$m_{void} = c_0 \varepsilon V_{bed}$$

Here ε is the void fraction of the bed and V_{bed} the packed bed volume. Combining these equations the mass balance for ideal adsorption can be expressed as:

$$c_0 \dot{V}_{feed} t_{id} = m_{ad} a_0 + c_0 \varepsilon V_{bed}$$

To describe a real breakthrough curve t_{id} must be replaced by following integral:

$$c_0 \dot{V}_{feed} \int_{t=0}^{t=t_s} \left(1 - \frac{c}{c_0} \right) dt = m_{ad} a_0 + c_0 \varepsilon V_{bed}$$

The ideal propagation velocity, v_{id} , of the MTZ can be expressed as:

$$v_{id} = \frac{h_{bed}}{t_{id}}$$

Here h_{bed} is the bed height. If the form of the concentration front is constant the ideal propagation velocity corresponds to the real propagation velocity.

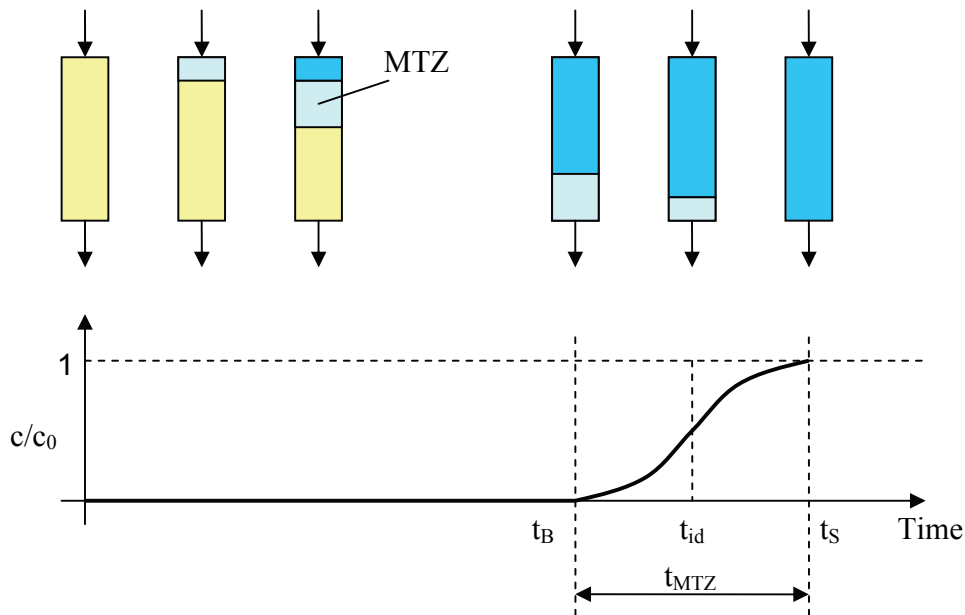


Figure 31: Movement of the MTZ through the packed bed and breakthrough

4.4.7 Flow Distribution and Pressure Drop in Packed Beds

The characteristics of the flow through packed beds are important in filter design and an understanding of the relationship between void fraction and flow distribution is essential. The void fraction, ε , of packed beds is defined as:

$$\varepsilon = 1 - \frac{V_p}{V}$$

Where V is the packed bed volume and V_p the volume of the adsorbent particles in the packed bed. The void fraction distribution is not uniform over the bed diameter. At the wall $\varepsilon = 1$ and then it follows a damped oscillatory function until it reaches a constant value about 3 particle diameters, d_p , from the wall where the packing is random. The maximum can be found approximately at a distance d_p from the wall. Various parameters like the particle size, particle shape or the bed diameter are influencing the distribution profile. An example for a typical radial void fraction distribution is shown in Figure 32. In beds with large diameter the average value of ε is around 0.37 – 0.4 for spheres and about 0.25 for cylinders [58].

The velocity profile of a packed bed is strongly related to the void fraction distribution. At a distance of approximately 0.5 d_p from the wall there is a peak velocity, which decreases sharply towards the wall and more gradually away from it. The flow rate through the bed has no influence on the velocity profile.

Variables like the particle size, fluid velocity and bed dimensions determine the pressure drop and have furthermore an important impact on the adsorption efficiency. The pressure drop through a packed bed can be calculated by applying following equation [58]:

$$\Delta p = \zeta \frac{H}{d_h} \frac{\rho_f}{2} \left(\frac{v_{f0}}{\varepsilon} \right)^2$$

Here Δp is the pressure drop, H the height of the bed, d_h the hydraulic diameter, ρ_f the fluid density, v_{f0} the superficial velocity, ε the void fraction and ζ the friction factor.

The superficial velocity is defined as:

$$v_{f0} = \frac{\dot{V}}{A} = 4 \frac{\dot{V}}{D^2 \pi}$$

In the above equation \dot{V} is the volume flow rate, A the cross sectional area of the bed and D the bed diameter.

The friction factor is defined by Ergun [59] as follows:

$$\zeta = \frac{133.3}{\text{Re}_{\varepsilon,h}} + 2.33$$

with

$$\text{Re}_{\varepsilon,h} = \frac{v_{f0} d_h \rho_f}{\varepsilon \mu_f}$$

and

$$d_h = \frac{2}{3} \frac{\varepsilon}{1 - \varepsilon} d_p$$

Where μ_f is the fluid viscosity and d_p the adsorbent particle diameter.

If the particle shape is taken into account, the friction factor for spherical particles can be expressed as [60]:

$$\zeta = 2.2 \left(\frac{64}{\text{Re}_{\varepsilon,h}} + \frac{1.8}{\text{Re}_{\varepsilon,h}^{0.1}} \right)$$

And as follows for sharp edged particles [60]:

$$\zeta = 2.2 \left(\frac{64}{\text{Re}_{\varepsilon,h}} + \frac{2.6}{\text{Re}_{\varepsilon,h}^{0.1}} \right)$$

Figure 33 shows a comparison of the measured and calculated pressure drop through a zeolite packed bed. The measurements have been performed by Zoechem AG [88] with a packed bed of 300 mm height and 25 mm diameter. Zeolite beads with a diameter of 2.5 – 5 mm have been used as filling material and nitrogen as working gas. The calculated pressure drop curve is determined by applying the above equations for spherical particles. Uncertain factors in the calculations are the void fraction and the particle diameter, which need to be estimated for the zeolite beads. This can be an explanation for the divergence between the calculation and the measurement however with the help of the calculation a rough estimation of the pressure drop is possible.

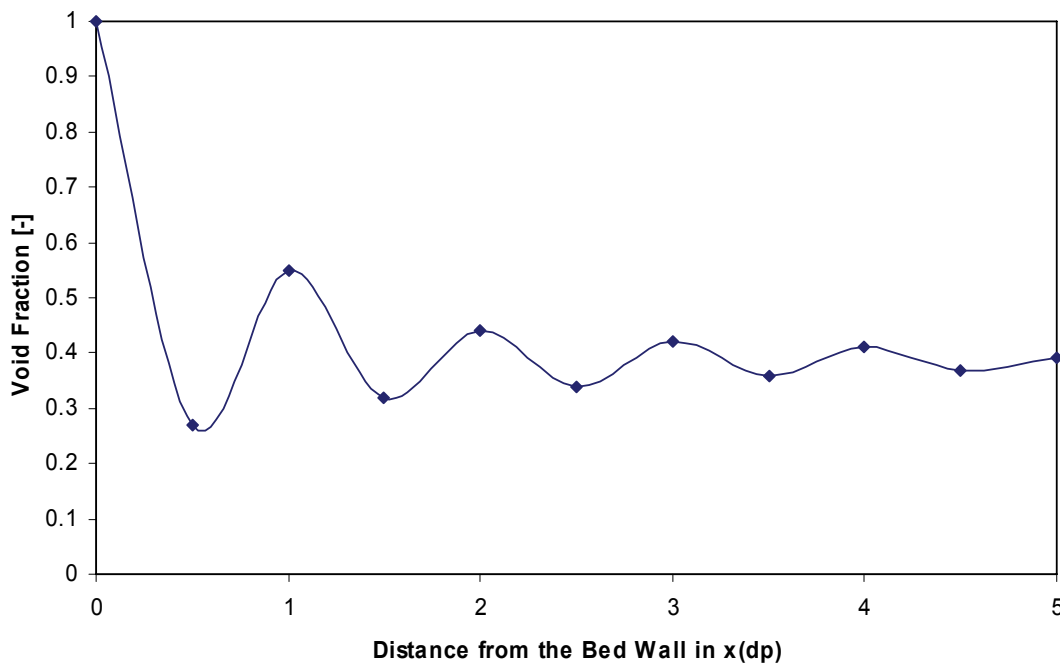


Figure 32: Typical radial void fraction distribution in packed beds

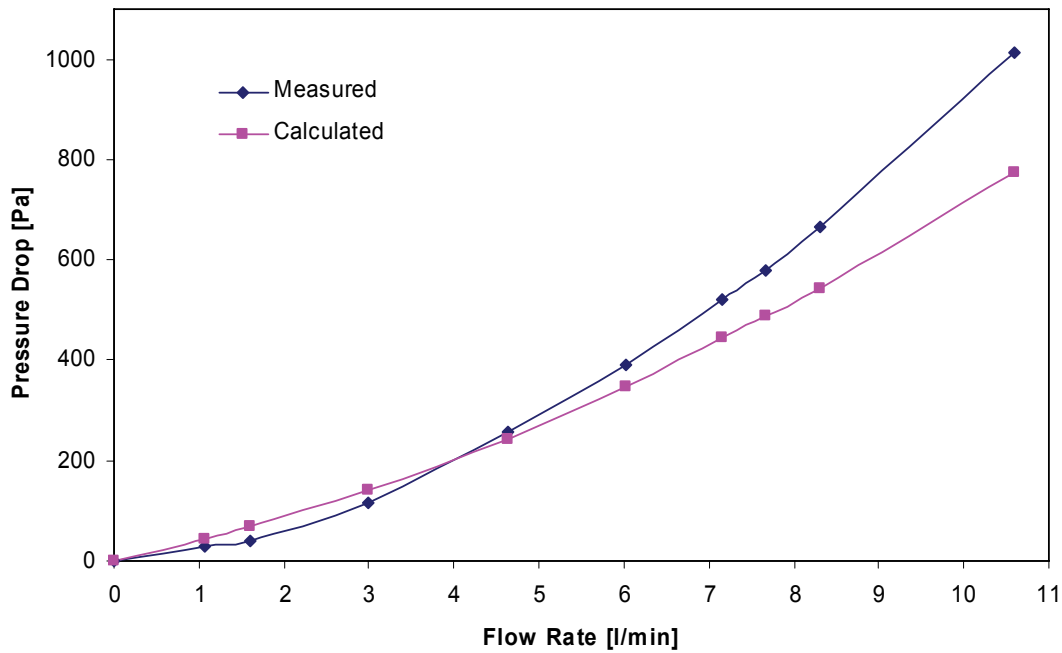


Figure 33: Calculated and measured pressure drop of a zeolite packed bed

4.4.8 Guideline for Dimensioning of Packed Beds

Important objectives of packed bed dimensioning are to achieve a low pressure drop and a uniform gas flow distribution over the cross-section of the adsorber. Usually a required flow rate is given and the bed dimensions have to be adjusted to it.

Bed Diameter

The bed diameter determines the flow regime in a packed bed at a specified gas flow rate. For gas adsorption processes the product of the superficial velocity, v_{f0} , and the fluid density, ρ_f , is recommended to be in the range of [58]:

$$0.22 \leq v_{f0} \sqrt{\rho_f} \leq 0.44$$

Too low gas velocities result in a non uniform velocity distribution in the bed and therefore in a poor adsorbent efficiency, whereby higher flow velocities yield a higher pressure drop (see chapter 4.4.7). By choosing a suitable superficial velocity the bed diameter can be calculated as follows:

$$D = 2 \sqrt{\frac{\dot{V}}{v_{f0} \pi}}$$

In the above equation D is the bed diameter and \dot{V} the total flow rate. To minimize the wall influence on the flow distribution through the bed, the following ratio of bed diameter, D , and particle diameter, d_p , should be realized [58]:

$$\frac{D}{d_p} \geq 10$$

Bed Height

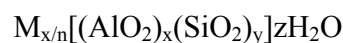
A minimum bed height is required to reduce negative effects like axial dispersion and channeling. A recommended value is given by [58]:

$$\frac{H}{D} \approx 5$$

Here H is the bed height and D the bed diameter. The bed height determines furthermore the capacity of the adsorber and thereby the lifetime before regeneration is required. There exists a linear relationship between the bed height and the pressure drop, and a minimization of the pressure drop is usually targeted.

4.4.9 Organosilicon Adsorption on Zeolites

Zeolites are microporous crystalline solids with well-defined structures. Generally they contain silicon, aluminum, oxygen in their framework and cations and water within their pores. At least forty of naturally occurring zeolite framework structures have been found and about 170 types of zeolites have been synthesized (see also Table 9). Many of them can be represented by the following stoichiometry [61]:



Where x and y are integers with $y/x \geq 1$, n is the valence of cation M and z is the number of water molecules in each unit cell. Also other compositions have been synthesized, including the growing category of microporous aluminophosphates, known as ALPOs. Zeolite frameworks are made up of 4-connected networks of atoms, like a tetrahedron, with a silicon atom in the middle and oxygen atoms at the corners. These tetrahedrons can then link together by their corners (see Figure 34) to form a rich variety of structures. The framework structure may contain linked cages, cavities or channels, with a limiting pore size of roughly 3 to 10 Å in diameter. The micropore structure is determined by the crystal lattice and is therefore precisely uniform with no distribution of pore size. Because of this unique porous property zeolites are used in a wide variety of applications from petrochemical industry to the separation and removal of gases and solvents. As an example a unit cell of a Faujasite type Zeolite is shown in Figure 35. It is formed by a oxygen 12-ring with a free diameter of approximately 7,4 Å (see Figure 36) in all

directions. All channels are connected and a three dimensional diffusion is possible. Figure 37 shows a picture of zeolite beads with different diameters.

Usually hydrophobic zeolites are used for the adsorption of organic compounds. They show a high adsorption capacity for hydrocarbons and a low one for water. For the TRT gas system the water content is no matter of interest but for the Muon detectors a small amount of water is required. Therefore hydrophobic zeolites will have to be used. The hydrophobicity of zeolites is designated by the Si/Al ratio whereby high Si/Al ratios indicates the hydrophobicity of a material. Through special treatments (steam, acid, SiCl_4) the aluminum content in a zeolite cell can be reduced and the Si/Al ratio can be increased.

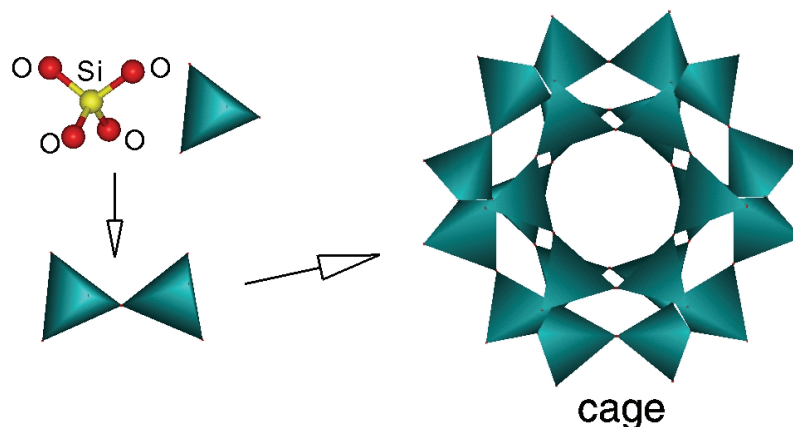


Figure 34: Zeolite Framework Structure [61]

Table 9: Atlas of zeolite framework types [61]

ABW	ACO	AEI	AEL	AEN	AET	AFG	AFI	AFN	AFO	AFR	AFS
AFT	AFX	AFY	AHT	ANA	APC	APD	AST	ASV	ATN	ATO	ATS
ATT	ATV	AWO	AWW	BCT	*BEA	BEC	BIK	BOG	BPH	BRE	CAN
CAS	CDO	CFI	CGF	CGS	CHA	-CHI	CLO	CON	CZP	DAC	DDR
DFO	DFT	DOH	DON	EAB	EDI	EMT	EON	EPI	ERI	ESV	ETR
EUO	FAU	FER	FRA	GIS	GIU	GME	GON	GOO	HEU	IFR	IHW
ISV	ITE	ITH	ITW	IWR	IWW	JBW	KFI	LAU	LEV	LIO	-LIT
LOS	LOV	LTA	LTL	LTN	MAR	MAZ	MEI	MEL	MEP	MER	MFI
MFS	MON	MOR	MOZ	MSO	MTF	MTN	MTT	MTW	MWW	NAB	NAT
NES	NON	NPO	NSI	OBW	OFF	OSI	OSO	OWE	-PAR	PAU	PHI
PON	RHO	RON	RRO	RSN	RTE	RTH	RUT	RWR	RWY	SAO	SAS
SAT	SAV	SBE	SBS	SBT	SFE	SFF	SFG	SFH	SFN	SFO	SGT
SOD	SOS	SSY	STF	STI	STT	TER	THO	TON	TSC	UEI	UFI
UOZ	USI	UTL	VET	VFI	VNI	VSV	WEI	WEN	YUG	ZON	

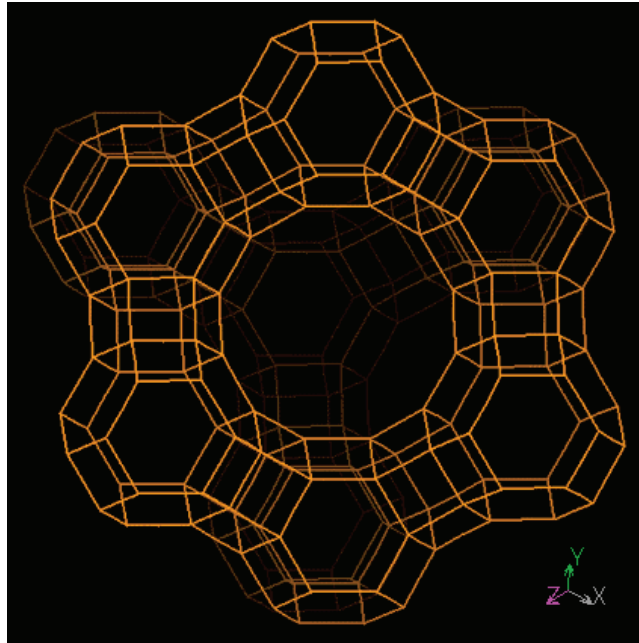


Figure 35: Faujasite unit cell viewed along $\{111\}$ $[61]$

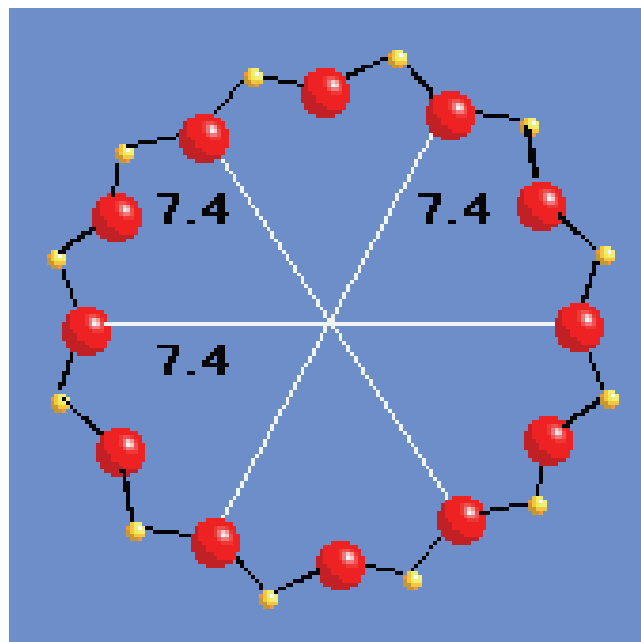


Figure 36: Faujasite 12-ring viewed along $\{111\}$ $[61]$



Figure 37: Zeolite Beads [88]

5 Deposit and Gas Analysis

Different techniques were used to identify the source and the composition of the aging causing impurities in the TRT gas system. The basic approach was to perform:

- deposit analysis
- gas analysis
- chemical analysis of substances in gas system components

The results of these analyses delivered the necessary information to develop procedures and methods for the prevention of wire aging. A detailed description of the techniques can be found in the following subchapters.

5.1 Deposit Analysis

Surface analyses of wires were performed with scanning electron microscopy (SEM) and energy dispersive X-ray (EDX) spectroscopy.

Figure 38 shows the SEM picture of an anode wire for the TRT detector. The wire surface appears clean and free of any deposits. A typical picture for a silicon aged wire is illustrated in Figure 39. It can be seen that the surface is covered with a large amount of needles/hairs causing a gas gain drop of about 30 %. An EDX analysis of these deposits (see Figure 40) identified the chemical elements C (carbon), O (oxygen), Si (silicon) and Au (gold). Thus organosilicon deposits can be assumed whereby the carbon content of the deposit represents alkyl groups (most likely methyl groups). The gold peak comes from the gold plated tungsten wire.

Results:

Surface analyses of aged wires showed needle like deposits which consists of the chemical elements C, O and Si. Thus organosilicon deposits can be assumed whereby the carbon content of the deposit represents alkyl groups (most likely methyl groups). Conclusion about the gas phase impurity composition and concentration are not possible. Therefore gas phase analyses (see chapter 5.2) and chemical analyses (see chapter 5.3) have been performed.

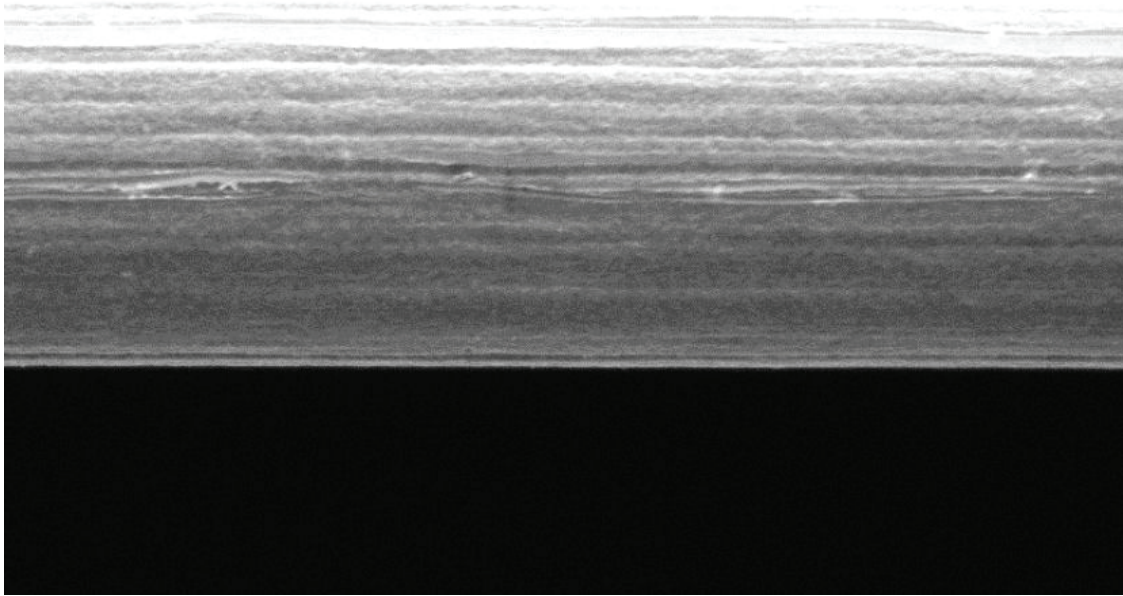
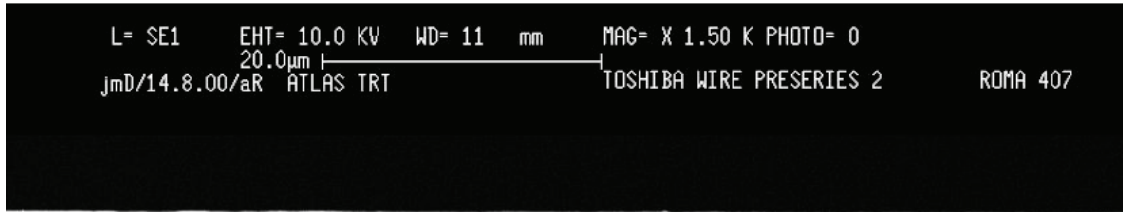


Figure 38: SEM picture of a clean anode wire surface

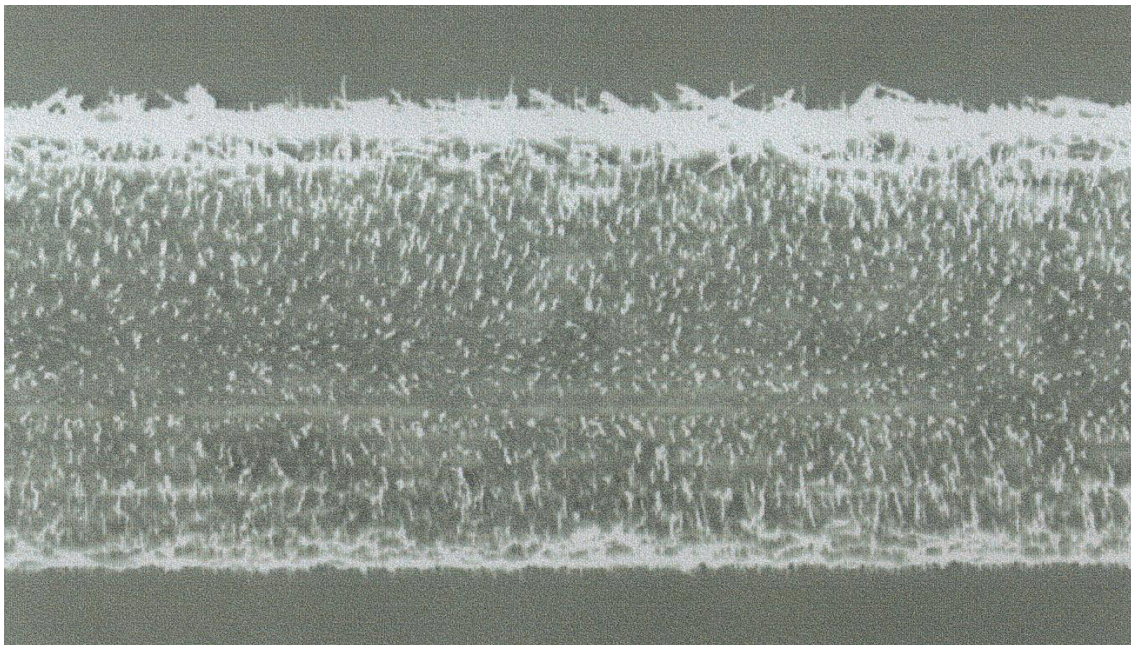


Figure 39: SEM picture of an anode wire surface with Si deposits

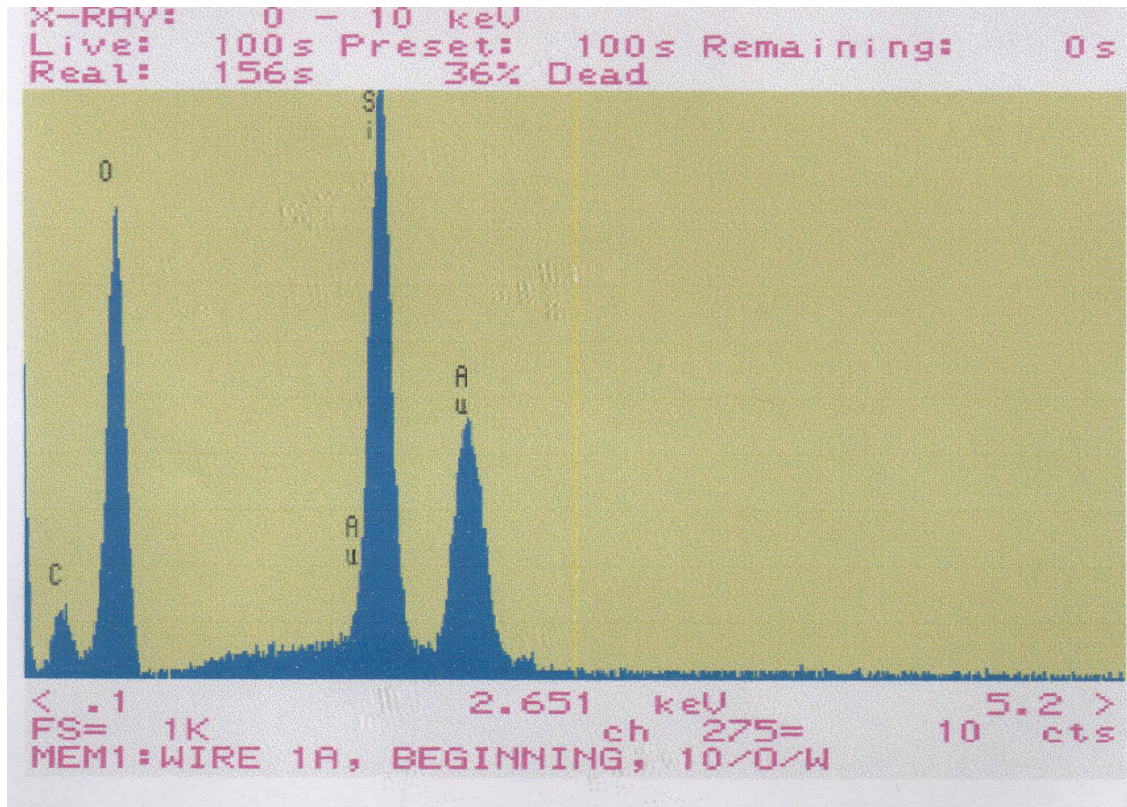


Figure 40: EDX spectrum of the wire surface shown in Figure 39

5.2 Gas Analysis

5.2.1 Introduction to the PTR-MS Instrument

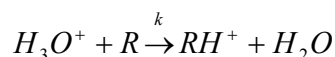
Gas chromatographic methods allow the quantification of trace compounds in the low ppb regime but they are not well suited for online investigations of time dependent concentrations. Mass spectrometry on the other hand is extremely fast but online gas analysis based on conventional mass spectrometry using electron impact ionization suffers from the strong fragmentation of molecular ionic species. Especially when a mixture of organic compounds has to be analyzed, the complexity of breakup patterns makes quantitative analysis of the concentrations of these components very difficult.

An alternative to the methods mentioned above is the proton-transfer-reaction mass spectrometer (PTR-MS) system which has been developed at the *University of Innsbruck - Institut für Ionenphysik*. It allows online measurements of trace components with concentrations as low as pptv up to a time response of 0.1 second. The ionization agent in PTR-MS instruments are H_3O^+ ions, and the buffer gas in which the ions are allowed to drift is the gas containing the trace compounds to be analyzed. H_3O^+ ions do not react with any compounds which have a proton affinity lower than H_2O , being 7,22 eV, but they do transfer their proton to volatile organic compounds (VOCs), all of which – with

the exception of a very few – have proton affinities larger than 7,22 eV (see Table 11) [63].

The PTR-MS system consists of three sections: an ion source, a drift tube and an ion detection section (QMS¹ / SEM²). A schematic drawing is shown in Figure 41 [64]. In the hollow cathode ion source H₃O⁺, primary ions are produced from pure water vapor. The H₃O⁺ ions enter the drift tube via a the inlet and undergo non-reactive collisions with any of the common components in carrier gases like (He, Ar, Xe, N₂, CO₂, O₂,...). A small fraction (~1%) of the H₃O⁺ ions transfer their proton to VOCs which are present as trace gases in the carrier gas and which have proton affinities higher than that one of water. These exothermic proton transfer reactions occur on every collision with well-known rate constants, having typical values $1,5 \times 10^{-9} \text{ cm}^3 \text{ s}^{-1} < k < 3 \times 10^{-9} \text{ cm}^3 \text{ s}^{-1}$. An advantage of using primary H₃O⁺ ions is that many of their proton transfer processes are non-dissociative, so that only one product ion species occurs for each neutral reactant. For an accurate quantification of the neutral reactants from measured primary and production signals, the reactions of H₃O⁺ with the neutrals can proceed under well defined conditions within the drift tube.

Detection of organic reactants R having low volume mixing ratios in the carrier gas rely on exothermic proton transfer reactions:



At the end of the reaction section the density of product ions [RH⁺] is given by:

$$[RH^+] = [H_3O^+]_0 (1 - e^{-k[R]t}) \approx [H_3O^+]_0 [R]kt$$

Where the density of H₃O⁺ ions at the end of the drift tube is about the same with and without the presence of trace compounds, thus $[H_3O^+]_0 \approx [H_3O^+]$. k is the reaction rate constant and for the proton transfer reaction and t is the average time the ions spent in the drift tube. As [R] denotes small densities of trace constituents, then $[RH^+] \ll [H_3O^+] \approx [H_3O^+]_0 = \text{constant}$.

Under typical operation conditions (reaction time t = 0.1 ms, reaction pressure p = 2 mbar, count rate $i(H_3O^+) = 3 \times 10^6 \text{ s}^{-1}$, reaction rate constant $k = 3 \times 10^{-9} \text{ cm}^3 \text{ s}^{-1}$), the smallest detectable volume mixing rate of organic compounds is about 10 pptv which was demonstrated by Hansel et al [67]. The uncertainty of [R] is about ± 30 % which is mostly due to the uncertainty of the reaction rate constant k, which is ± 20 %. The reproducibility for quantitative analysis is better than 10 % [64].

Different trace constituents in a carrier gas can have the same molecular weight and will be therefore placed on the same ion mass. To distinguish these compounds the natural isotopic abundances of elements (see Table 10 for Si and C) can be used.

Further information about the PTR-MS can be found elsewhere [64, 65, 66, 67].

¹ QMS Quadrupole Mass Spectrometer

² SEM Secondary Electron Multiplier

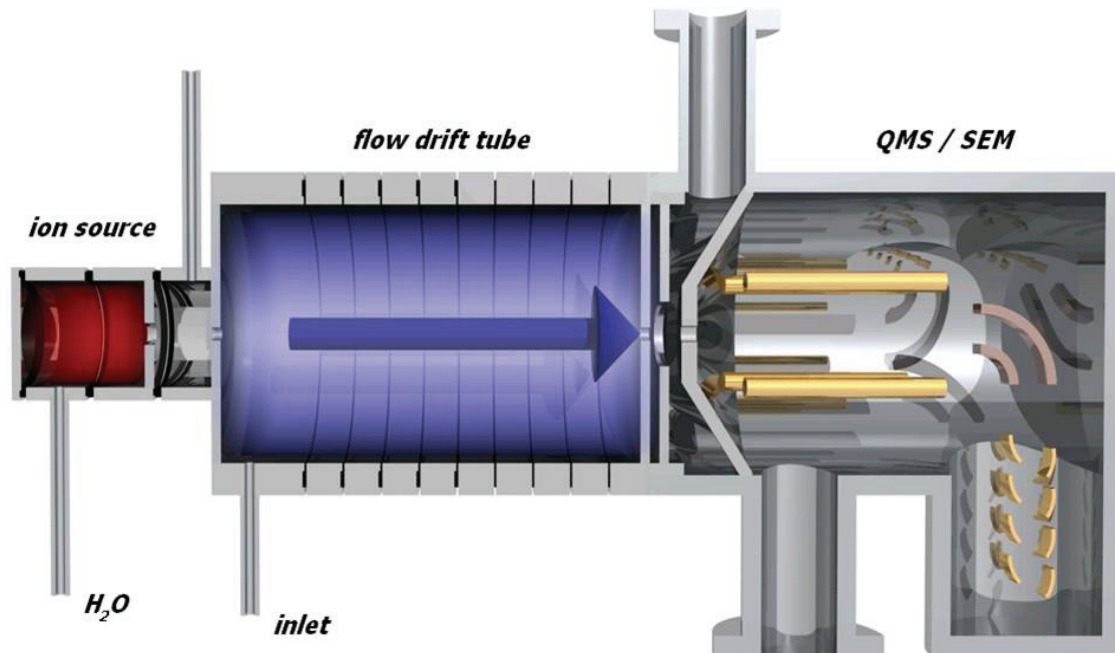


Figure 41: Principle structure of the PTR-MS with its 3 subsections: ion source, flow drift tube, ion detection system (QMS / SEM) [68]

Table 10: Natural isotopic abundances of Si and C

Ion Mass	Si [%]	C [%]
A	100	100
A+1	5.1	1.1
A+2	3.4	0.0

Table 11: Proton affinities of various volatile organic compounds [63]

Component	Proton Affinity	
	[kcal/mol]	[eV]
He	42.5	1.8
Ne	48.1	2.1
Ar	88.6	3.8
O ₂	100.9	4.4
N ₂	118.9	5.1
CO ₂	130.9	5.7
CH ₄	132	5.7
N ₂ O	136.5	5.9
CO	141.9	6.2
H₂O	166.5	7.2
C ₄ H ₁₀	163.3	7.1
H ₂ S	170.2	7.4
HCN	171.4	7.4
C ₆ H ₆	181.9	7.8
C ₃ H ₆	179.8	7.8
CH ₃ OH	181.9	7.9
CH ₃ CN	188	8.1
CH ₃ COH	186.6	8.1
C ₂ H ₅ OH	188.3	5.2
CH ₃ COCH ₃	196.7	8.5
NH ₃	204	8.8

5.2.2 PTR-MS Measurements

Setup:

A stainless steel tube (1/8" diameter) connected to the inlet of a rotameter (Vögtlin V100) has been investigated with a highly sensitive PTR-MS instrument enabling detection at pptv trace level. The sample has been placed in an oven which was operated at 30 °C (oven off) and 60 °C. This allows to determine variations of emission rates of substances with the sample heating temperature. The general operating conditions were:

- gas flow ~40 sccm
- gas mixture: 21 % O₂, 79 % N₂ (synthetic air)
- heated inlet line temperature ~65 °C (connection between oven and PTR-MS)
- PTR-MS inlet and drift tube temperature ~80 °C
- drift tube voltage and pressure kept at nominal values

Experiments:

Initial measurements of a stainless steel tube without rotameter:

- continuous bar graph scans from m20+ to m300+ at 1 second per mass

- sequence of bar graph scans made at ~ 30 °C
- oven switched on (set point ~ 60 °C) – continues scans

This test was done to determine if the rotameter or the stainless steel tube is the source of contamination. Being at the inlet of the rotameter this sample was tested first. A mass spectrum from this test is displayed below in Figure 42. As it can be seen, the sample appears to be fairly clean. No effects were observed when the sample was heated. The mass spectrum of the stainless steel tube without the rotameter represents more or less the machine background.

Further measurements of the stainless steel tube attached to the inlet of a rotameter:

- continuous bar graph scans from m_{20+} to m_{300+} at 1 second per mass
- sequence of bar graph scans made at ~ 30 °C
- oven switched on (set point ~ 60 °C) and variations of emissions with temperature monitored

With the stainless steel tube now attached to the inlet of the rotameter, measurements showed a very different mass spectrum. The mass spectrum is displayed below in Figure 43, it shows the presence of many high-mass peaks. These data represents results at the beginning of heating at ~ 60 °C. After a period of almost 20 hours of heating at ~ 60 °C, the mass spectrum was measured again (see Figure 44). It can be seen that the background has been greatly reduced but certain masses are ever present. Five peaks in particular seen here come from masses m_{149+} , m_{163+} , m_{177+} , m_{223+} and m_{287+} , plus their isotopes. An additional peak is present at m_{297+} (see Figure 43), which, after a period of heating dropped below 10 counts per second corresponding to approximately 50 pptv and thus is not seen in the mass spectrum of Figure 44.

The PTR-MS cannot distinguish between two compounds having the same molecular weight and therefore identification is not always easy to accomplish. However, the series of masses m_{149+} , m_{163+} , m_{177+} , and m_{223+} found in the mass spectrum of Figure 43 and Figure 44 have a typical “fingerprint” of protonated polymethylsiloxanes. Below some possible candidates for the detected ion masses are listed:

Mass: m_{149+}

Possible candidate: Pentamethyldisiloxane (148 amu)

Formula: $C_5H_{16}OSi_2$

Mass: m_{163+}

Possible candidate: Hexamethyldisiloxane (162 amu)

Formula: $C_6H_{18}OSi_2$

Mass: m_{177+}

Possible candidate: Ethylpentamethyldisiloxane (176 amu)

Formula: $C_7H_{20}OSi_2$

Mass: m223+

Possible candidate: Hexamethylcyclotrisiloxane (222 amu)

Formula: $C_6H_{18}O_3Si_3$

The instrumental sensitivity during the study was typically 5 pptv / cps. This value is a rough estimate which is claimed to be accurate within a factor of 2. A higher accuracy can be reached if needed by using calibration standards of individual compounds.

Results:

These measurements have clearly shown that the rotameter (Vögtlin V100) is the source of contamination and that organosilicon compounds, namely polymethylsiloxanes, are present in the gas phase. The concentration level of these organosilicon compounds is between 500 and 3000 pptv. A quantitative certification of the absolute VOC emission rate of gas system components is feasible but was not part of this study.

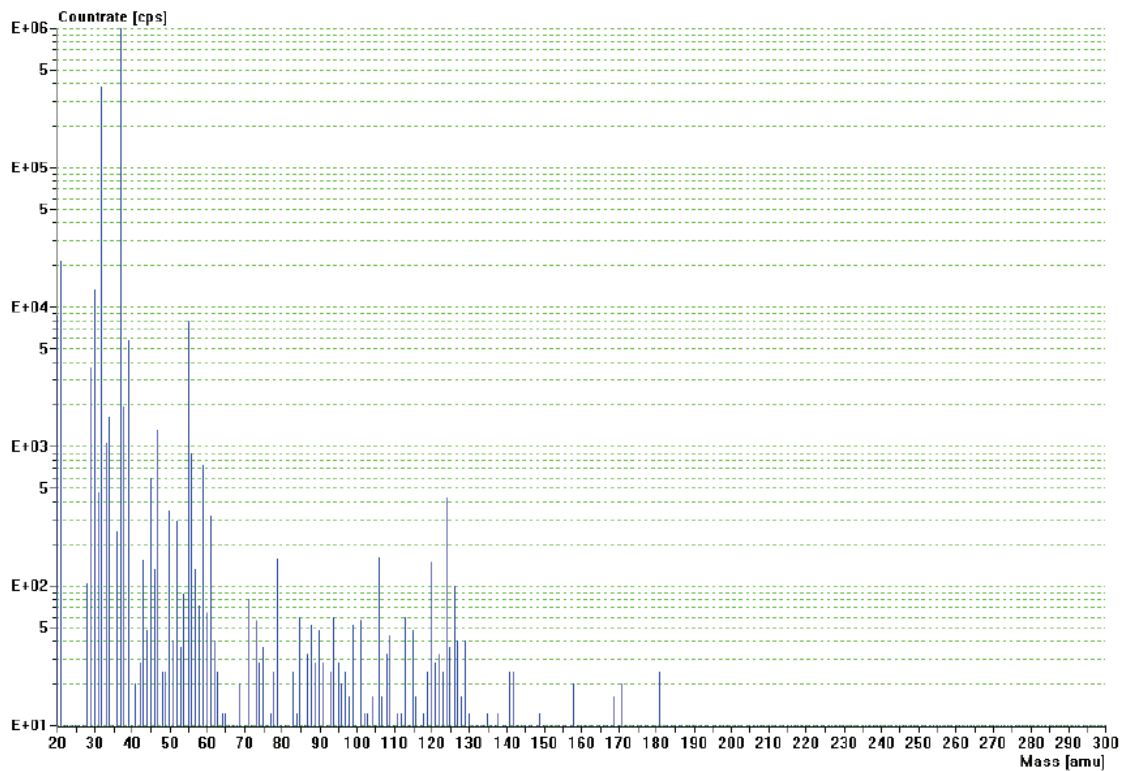


Figure 42: Mass spectrum of a stainless steel tube at ~30 °C

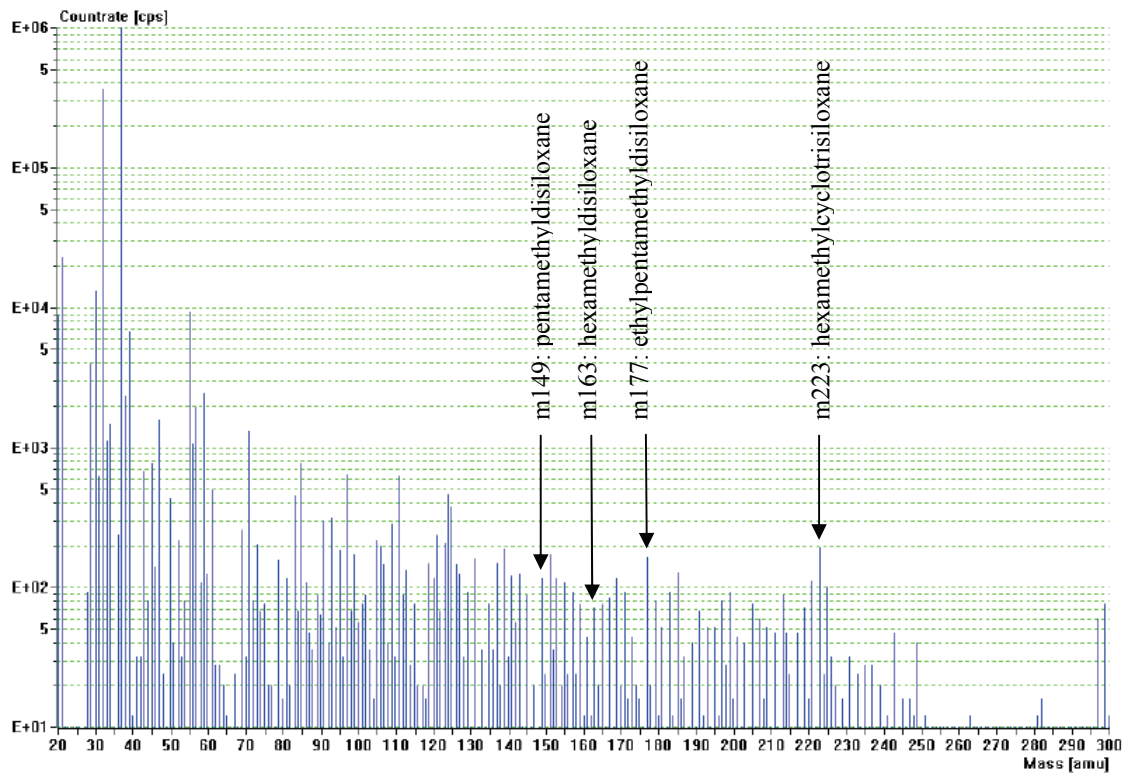


Figure 43: Mass spectrum of a stainless steel tube with a rotameter attached at initial stages of heating ($\sim 60^\circ\text{C}$)

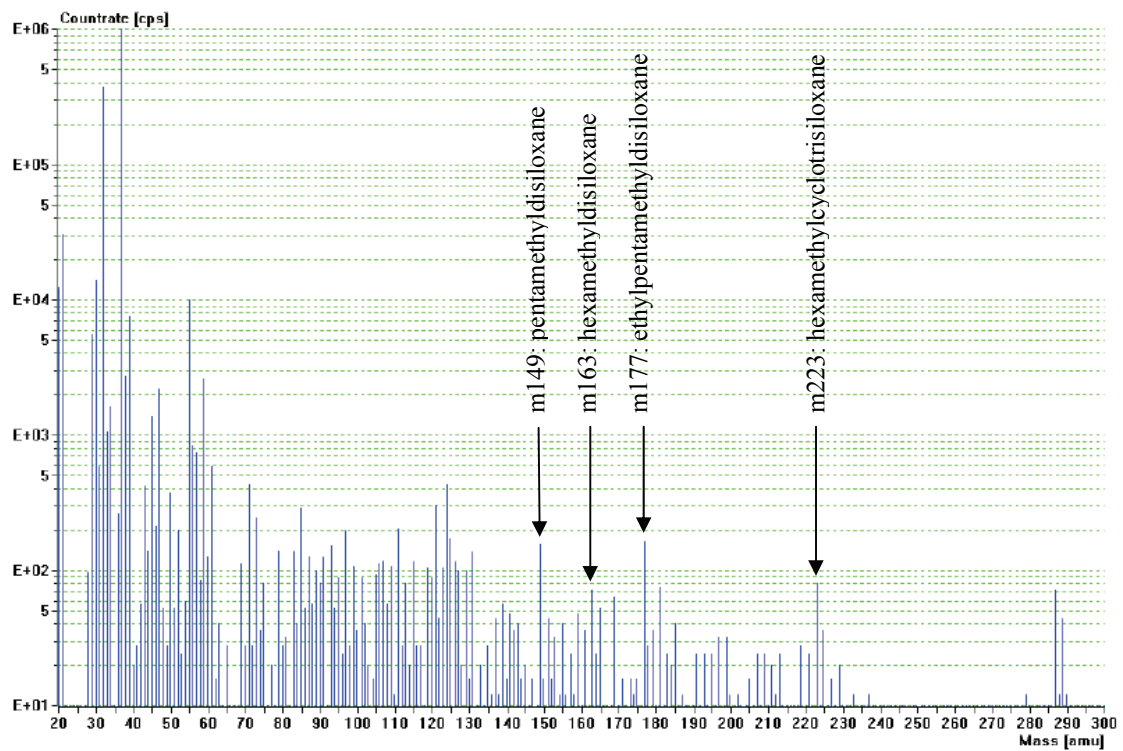


Figure 44: Mass spectrum of a stainless steel tube with a rotameter attached after about 20 hours of heating at $\sim 60^\circ\text{C}$

5.3 Chemical Analysis

5.3.1 Introduction to Infrared Spectroscopy

Fourier Transformed Infrared Spectroscopy (FTIR) is a dynamic tool for the study of molecular structures of organic and inorganic substances. The main goal of infrared (IR) spectroscopic analysis is to determine the chemical functional groups in the sample. Different functional groups absorb characteristic frequencies of IR radiation. Using various sampling accessories, IR spectrometers can be used for a wide range of sample types such as gases, liquids and solids. The IR radiation spans a section of the electromagnetic spectrum having wavenumbers from roughly 13000 to 100 cm^{-1} . The range of interest for the analysis of organic compounds is between 4000 and 400 cm^{-1} . The resonant frequencies or vibrational frequencies can be in a first approach related to the length of the bond, and the mass of the atoms at either end of it. Thus the frequency of the vibrations can be associated with a particular bond type. Bonds can vibrate in six different ways, symmetrical and asymmetrical stretching, scissoring, rocking, wagging and twisting.

This analytical technique has been applied to identify the presence of silicon based oils, lubricants or greases in components for the TRT gas system. The experiments were carried out by the CERN Chemical Laboratory and a detailed description of the method can be found below.

5.3.2 Instrumentation

A FTIR system consists of three basic spectrometer components: radiation source, interferometer and detector. Figure 45 illustrates the design of a typical FTIR spectrometer [70]. The IR radiation from a broadband source is first directed into an interferometer. Here a beam splitter divides the IR beam in such a way that 50% is reflected to a fixed mirror and 50% is transmitted to a moveable mirror. After being reflected at each mirror the beam splitter recombines the beams. The resulting beam travels now with different optical paths to generate constructive and destructive interference. Then the beam passes through the sample compartment and reaches the detector. The two most popular detectors for a FTIR spectrometer are deuterated triglycine sulphate (DTGS) and mercury cadmium telluride (MCT). To reduce the strong background absorption from water (peaks at 3500, 1650, 600 and 300 cm^{-1}) and carbon dioxide (peaks at 2350 and 670 cm^{-1}) in the atmosphere, the optical bench is usually purged with inert gas [74].

The IR spectrometer used was the Bruker IFS 66 spectrometer. It has near, mid and far infrared capability, and can be applied for transmission measurements in liquids, gas and solid samples. All spectra recorded were done with a window of ZnS (Irtran-2 or Cleartran). This optical material has a transmission range between 50000-720 cm^{-1} and is very resistant to organic solvents. The used IR source is a specific one for mid IR studies

(Globar). A DTGS detector has been utilized with a bandwidth of $10000\text{-}370\text{ cm}^{-1}$. The sample analyses were performed in a range of $4000\text{-}750\text{ cm}^{-1}$ because the main absorption bands of silicones are not located lower than 750 cm^{-1} . All spectra were done in transmission mode because it provides a better contrast between intensities of strong and weak bands [70].

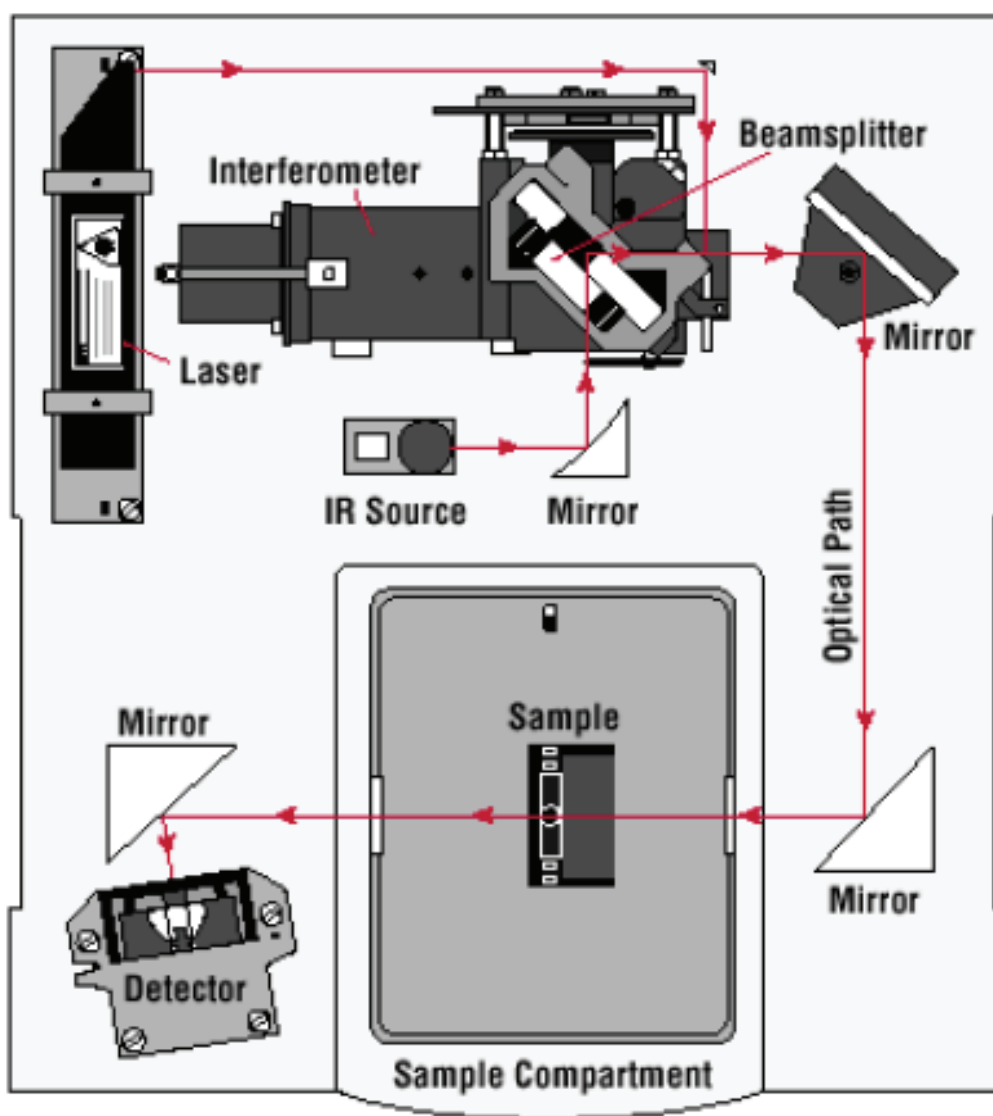


Figure 45: Illustration of a typical FTIR spectrometer [70]

5.3.3 Sample Preparation

Non-polar compounds like oils, resins or greases dissolve preferred in very non-polar solvents. Hexane is largely unreactive, very non-polar and is frequently used as an inert solvent in organic reactions. It is an alkane with the molecular formula C_6H_{14} .

Thus n-hexane has been used for the solubilization of organosilicon substances which are eventually present in components needed for the construction of the TRT gas system. The amount of solvent necessary to prepare a sample depends on the surface area of the component to be analyzed. The recommended standard volume of n-hexane is 340 ml/m^2 [75]. For example a tube with an inner diameter of 8 mm and a length of 2.5 m will require 19 ml of n-hexane. For the extraction the gas system component has to be filled up with the n-hexane and shaken for 10 minutes. Thereafter a correlated volume of the solution obtained is evaporated on a ZnS window and the film formed is investigated with a FTIR spectrometer in transmission mode [71, 75].

5.3.4 Interpretation of IR Spectra

IR spectroscopy is mainly used in two ways: structural elucidation and compound identification. This is possible because chemical bonds have specific frequencies at which they vibrate corresponding to energy levels. The resonant frequencies or vibrational frequencies are determined by the shape of the molecular potential energy surfaces, the masses of the atoms and, eventually by the associated vibronic coupling. In order to be IR active, a molecule needs to have a changing dipole. The resonant frequencies can be in a first approach related to the length of the bond, and the mass of the atoms at either end of it. Thus, the frequency of the vibrations can be associated with a particular bond type. Bonds can vibrate in six different ways, symmetrical and asymmetrical stretching, scissoring, rocking, wagging and twisting.

Due to the specific nature of the absorption bands of organosilicon compounds, IR spectroscopy can be used for the identification of their presence in gas system components. Some of the characteristic absorption bands for specific types of bonds to silicon are summarized in Table 12. A discussion about their significance and interpretation is done below.

C-H:

Methyl groups, methylene groups and methine hydrogen on carbon atoms absorb between 2850 and 3000 cm^{-1} . It is difficult to differentiate between these types of hydrogen. For a CH_3 group symmetric and asymmetric stretching will be observed. These peaks are usually sharp and of medium intensity. Considerable overlap of several of these bands usually results in absorption that is intense and broad in this region [69]. Figure 46 shows a typical absorption band for C-H stretching of CH_3 . The presented IR spectrum is from silicon based oil.

Si-H:

Stretching frequencies of the Si-H bond show absorption between 2260 - 2100 cm^{-1} and bending frequencies absorb in the region of 950 - 800 cm^{-1} [77, 78]

Si-CH₃:

The Si- CH_3 group is characterized by a very strong and sharp absorption band between 1270 - 1250 cm^{-1} due to CH_3 symmetric deformation and between 870 - 750 cm^{-1} due to Si-

C stretching and CH₃ rocking. The asymmetric CH₃ deformation absorbs weakly near 1410 cm⁻¹ [79]. Figure 46 shows the main absorption bands of compounds with Si-CH₃ bonds. The presented IR spectrum is from silicon based oil.

Si-CH₂-R:

A medium intensity absorption band due to the Si-CH₂-R group can be found between 1250-1220 cm⁻¹. In straight chain compounds absorption between 760-670 cm⁻¹ is due to CH₂ rocking. CH₂ bonds on halogens, phosphorous and sulfur absorb near 1410 cm⁻¹ due to CH₂ deformation and between 1250-1220 cm⁻¹ due to CH₂ wagging. The Si-C₂H₅ group absorbs between 1020-1000 and 970-945 cm⁻¹ [79].

Si-C₆H₅:

The Si-C₆H₅ group absorbs between 1125-1100 cm⁻¹ due to a planar ring vibration having and Si-C stretching. Phenyl bands are found near 1430, 730, 695 cm⁻¹ [79]

Si-CH=CH₂:

The Si-CH=CH₂ group is characterized by vinyl vibrations between 1610-1590 cm⁻¹ (C=C stretching), 1410-1390 cm⁻¹ (CH₂ bending), 1020-990 cm⁻¹ (CH wagging) and 980-940 cm⁻¹ (CH₂ wagging).

Si-O-R:

The Si-O-R group (R= saturated aliphatic group) has a strong absorption band between 1110-1000 cm⁻¹ due to asymmetric Si-O-C stretching. Si-O-CH₃ absorbs near 2840 cm⁻¹ (CH₃ symmetric stretching) and 1190 cm⁻¹ (CH₃ rocking). The asymmetric and symmetric stretching of the Si-O-C bonds absorbs near 1100 and 850-800 cm⁻¹. The Si-O-C₂H₅ group absorbs between 1175-1160 cm⁻¹, 1100-1075 cm⁻¹ and 970-940 cm⁻¹ [76].

Si-O-C₆H₅:

The Si-O-C₆H₅ group absorbs between 970-920 cm⁻¹ due to Si-O stretching [80].

Si-O-Si:

Siloxanes are characterized by a strong absorption band between 1130-1000 cm⁻¹ due to asymmetric Si-O-Si stretching. This is shown in Figure 46 for a silicon based oil. In infinite siloxane chains the absorption band occurs between 1085-1020 cm⁻¹. Cyclotrisiloxane rings absorb near 1020 cm⁻¹ and cyclic tetramers near 1090 cm⁻¹ [81].

Si-OH:

The Si-OH group has an absorption band between 3700-3200 cm⁻¹, like alcohols, due to monomers (in solution) and hydrogen bonded polymers. A strong absorption band due to Si-O stretching occurs between 950-830 cm⁻¹.

Si-Halogen:

The fluorine group absorption bands are between [82]:

- 980-945 cm^{-1} (strong) and 910-860 cm^{-1} (medium) for SiF_3
- 945-915 cm^{-1} (strong) and 910-870 cm^{-1} (medium) for SiF_2 .
- 920-820 cm^{-1} for SiF

The chlorine group absorbs between:

- 620-570 cm^{-1} (strong) and 535-450 cm^{-1} (medium) for SiCl_3
- 600-535 cm^{-1} (strong) and 540-460 cm^{-1} (medium) for SiCl_2
- 550-470 cm^{-1} for SiCl

Si-N:

The Si-NH_2 group has two bands between 3570-3390 cm^{-1} in solution. The NH_2 deformation band occurs near 1540 cm^{-1} . The Si-NH-Si group absorbs near 3400 cm^{-1} , 1175 cm^{-1} and 935 cm^{-1} [83].

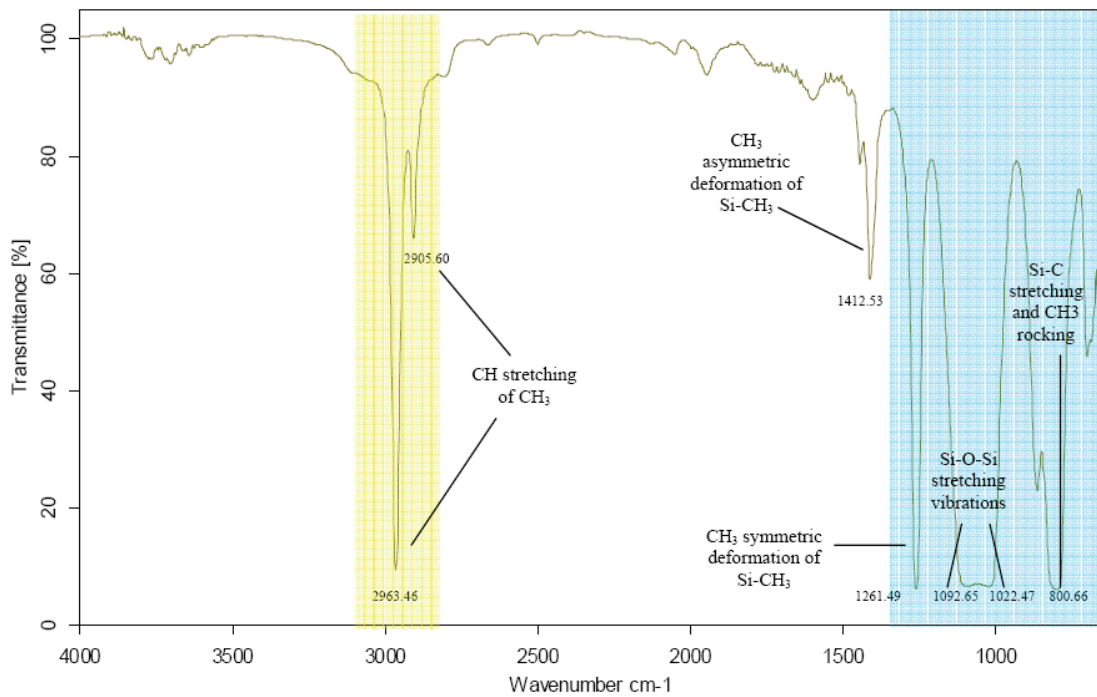


Figure 46: Infrared spectrum of a silicon oil [69]

Table 12: Detailed absorption table of bonds in organosilicon molecules [70]

Silicon Bond	Absorption Range and Intensity [cm⁻¹]
C-H	3000-2850, medium, (CH ₃ stretching)
Si-H	2260-2100, strong, (Si-H stretching) 960-800, medium, (Si-H bending)
Si-CH ₃	1410, weak, (CH ₃ asymmetric stretching) 1270-1250, strong, (CH ₃ symmetric bending) 870-750, medium, (CH ₃ rocking, Si-C stretching)
Si-CH ₂ -R	1410, weak, (CH ₂ bending) 1250-1220, medium, (CH ₂ wagging) 1020-1000; 970-945, medium, (Si-C ₂ H ₅ stretching) 830-670, strong, (Si-C stretching) 760-670, medium, (CH ₂ rocking)
Si-C ₆ H ₅	1590, medium, (C-C ring stretching) 1430, strong, (phenyl stretching) 1125-1100, strong, (ring vibration + Si-C stretching) 700-690 (2 bands), strong, (H phenyl wagging)
Si-CH=CH ₂	1610-1590, medium, (C=C stretching) 1410-1390, medium, (CH ₂ bending) 1020-990, medium, (CH wagging) 980-940, medium, (CH ₂ wagging)
Si-CH ₂ -Si	1080-1040, strong, (CH ₂ wagging) 770, medium, (Si-C-Si stretching)
Si-O-CH ₃	2840, strong, (CH ₃ symmetric stretching) 1100-1000, medium, (Si-O-C asymmetric stretching) 1190, strong, (CH ₃ rocking) 850-800, medium, (Si-O-C symmetric stretching)
Si-O-C ₂ H ₅	1175-1160, medium, (CH ₃ rocking) 1100-1075, strong, (Si-O-C asymmetric stretching) 970-940, medium, (Si-O-C symmetric stretching)
Si-O-aryl	970-920, strong, (Si-O stretching)
Si-O-Si	1130-1000, strong, (Si-O asymmetric stretching)
Si-OH	3690, weak, (free OH stretching) 3400-3200, medium, (bonded OH stretching) 1030, medium, (Si-OH bending) 950-830, medium, (Si-O stretching)
Si-halogen	1000-800, strong, (Si-F stretching) 650-460, strong, (Si-Cl stretching)
Si-NH ₂	3480-3400 (2 bands), medium, (N-H stretching) 1540, medium, (NH bending)
Si-NH-Si	3420-3390, medium, (NH stretching) 1170, strong, (NH bending) 950-910, strong, (Si-N-Si stretching)

5.3.5 IR Measurements

Various gas system components, oils, greases and lubricants have been investigated by FTIR spectroscopy at CERN. In this work two examples will be discussed.

Figure 47 illustrates the IR spectrum of the grease Molycote 111 (Dow Corning). The peak near 3000 cm⁻¹ indicates C-H bonds (stretching of CH₃) whereby Si-CH₃ groups are

represented by the peaks near 1260 cm^{-1} (CH_3 symmetric deformation) and 800 cm^{-1} (Si-C stretching and CH_3 rocking). The Si-O-Si group is displayed by the absorption band between $1130\text{-}1000\text{ cm}^{-1}$ due to asymmetric stretching. The chemical composition of the grease Molykote 111 is summarized in Table 13 and it shows that polymethylsiloxane is the main substance with a weight fraction of more than 70 %.

Figure 48 presents the IR spectrum of a sample prepared by hexane solubilization (see chapter 5.3.3) of substances present in a stainless steel pipe. The same absorption bands like for the Molykote 111 grease can be identified and it can be assumed that this pipe is polluted by a polymethylsiloxane.

Figure 49 shows the IR spectrum of hexamethyldisiloxane (HMDS) with a very sharp absorption peak near 1100 cm^{-1} due to strong Si-O-Si asymmetric stretching. The IR spectra displayed in Figure 47 and Figure 48 are similar to that one of HMDS. This proves the capability of FTIR spectroscopy to identify organosilicon compounds in gas system components.

Results:

These measurements proved the capability of the FTIR spectroscopy to identify organosilicon impurities in gas system components. Polymethylsiloxane has been classified to be the main substance of the impurities. However it has its limitations in the component geometry (complex structure, size, volume) and in certain cases a clear interpretation of a spectrum is difficult through overlapping effects. Furthermore this method is only qualitative, conclusions about VOC emission rates and gas phase concentrations are not possible.

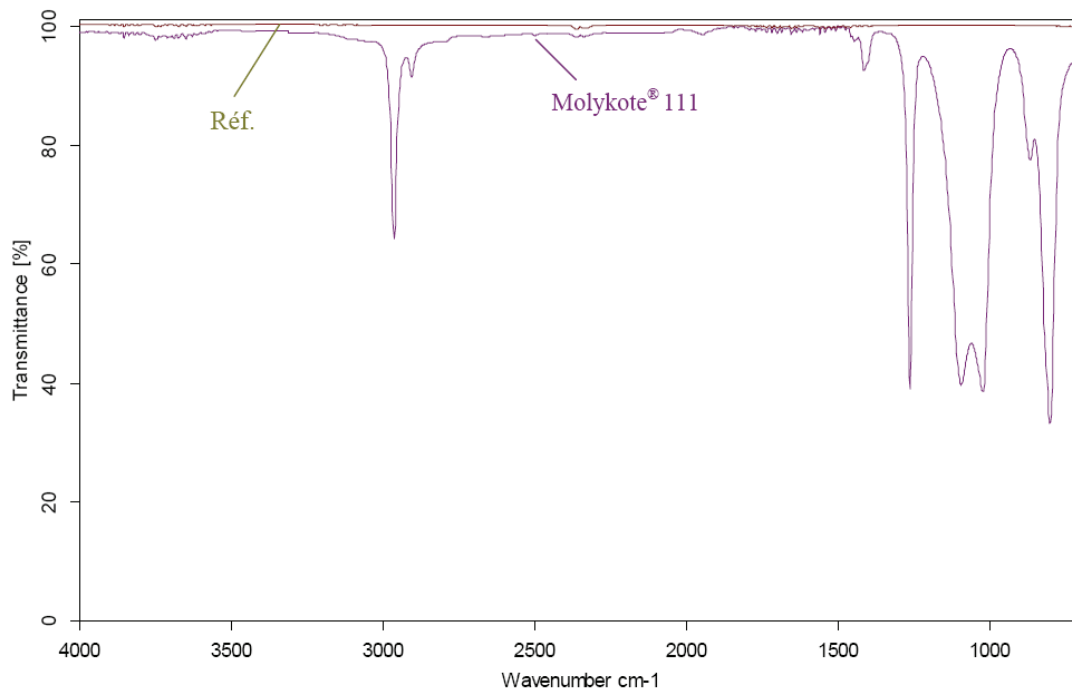


Figure 47: Infrared spectrum of the Dow Corning grease Molykote 111 [72]

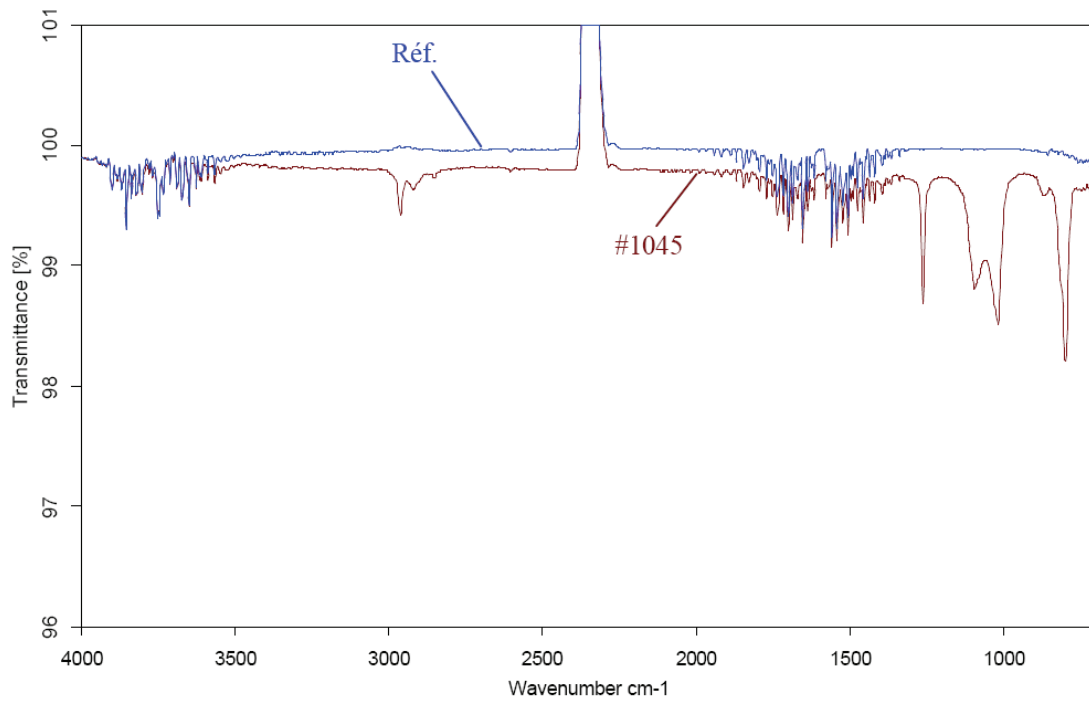


Figure 48: Infrared spectrum of a sample prepared by hexane solubilization of substances present in a stainless steel pipe (reference number #1045) [73]

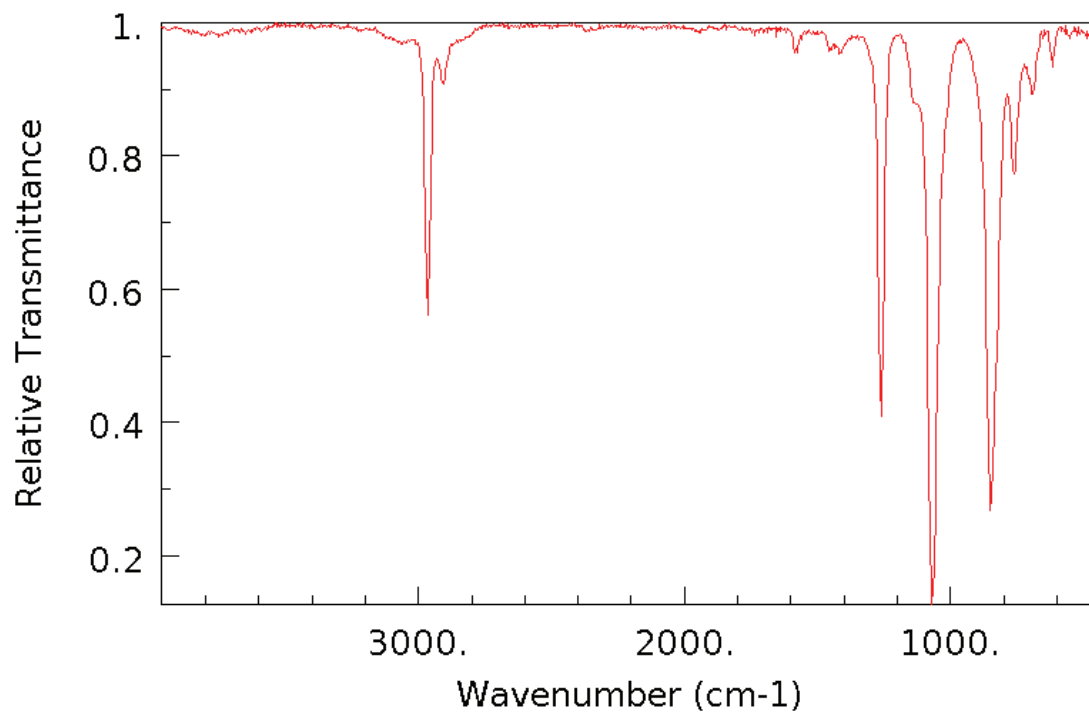


Figure 49: Infrared spectrum of hexamethyldisiloxane ($C_6H_{18}OSi_2$) [49]

Table 13: Chemical composition of the Dow Corning grease Molycote 111

Compound	Cas Number	Wt. %
Polydimethylsiloxane	63148-62-9	> 60
Silica, amorphous	7631-86-9	7 - 13
Dimethylsiloxane, hydroxy-terminated	70131-67-8	7 - 13

6 Systematic Component Validation Procedure

6.1 Optimization of the Aging Test Procedure

Aging tests are carried out with prototypes of straw proportional chambers which are connected in parallel (see Figure 50). For these tests a material or component sample is introduced into the clean and validated setup upstream of the straw prototype which is irradiated by a X-ray source. If wire deposits are formed a gas gain drop is observed in the irradiated area. The signal amplitude measurement accuracy in these tests is ± 1 percent. Ideally the tests should be performed with the active TRT gas mixture Xe-CO₂-O₂, but because of the high costs of xenon Ar-CO₂ is used instead. Figure 51 represents a comparison of aging test results with different mixtures: Ar-CO₂, Ar-CO₂-O₂ and Xe-CO₂-O₂. A non-clean rotameter was used as silicon source. The tests were performed at 10 times the nominal TRT gas flow rate (1.5 cm³/min) and at a current density of 100 nA/cm. It can be seen that the aging rate is the same for these gas mixtures, indicating that the plasma conditions near the wire are similar and therefore also the deposit formation process. This may look contradictorily first to the statement made in chapter 3.4.2 where the ratio of O₂ over the organosilicon precursor was pointed out as key parameter to control the deposition properties. But oxygen radicals will be present in all these gas mixtures through CO₂ dissociation in the avalanche plasma. Furthermore the impurity level is very low (< 10 ppb), thus the oxygen radical concentration in Ar-CO₂ will be still several orders of magnitudes higher than the impurity level.

In order to optimize the test conditions, special studies were carried out with a non clean rotameter as silicon source. Figure 52 shows the aging rate dependency versus the gas flow rate in the straw. The nominal gas flow in the TRT is 0.15 cm³/min per straw and the tests have been performed with a multiple of it at a current density of 100 nA/cm. The aging rate increases approximately linear with the gas flow up to the level of 8-10 times of the nominal flow where it reaches a maximum or saturates. Figure 53 illustrates the aging rate dependency versus the current density at 10 times the nominal gas flow rate. It can be seen that the aging rate increases linearly till about 110 nA where it reaches a maximum or saturates.

These experiments led to the recommendation to perform aging tests at 10 times the nominal gas flow rate and at a current density of 100 nA/cm. Thus maximum sensitivity to impurities will be guaranteed in shortest possible exposure times.

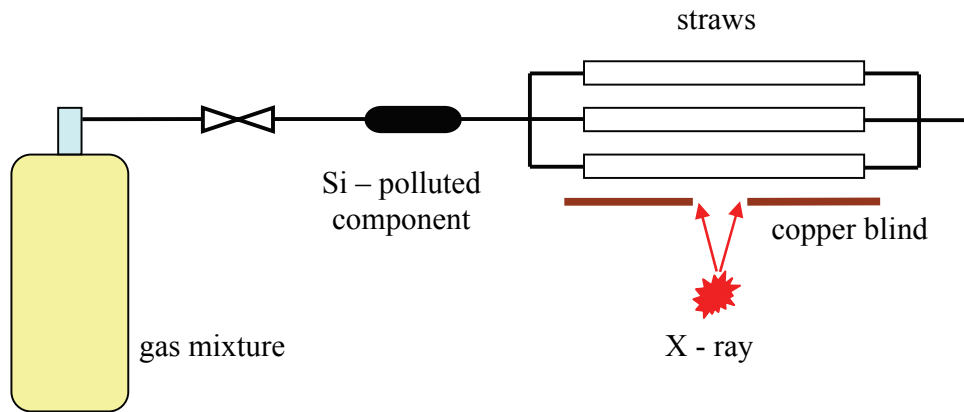


Figure 50: Aging test setup

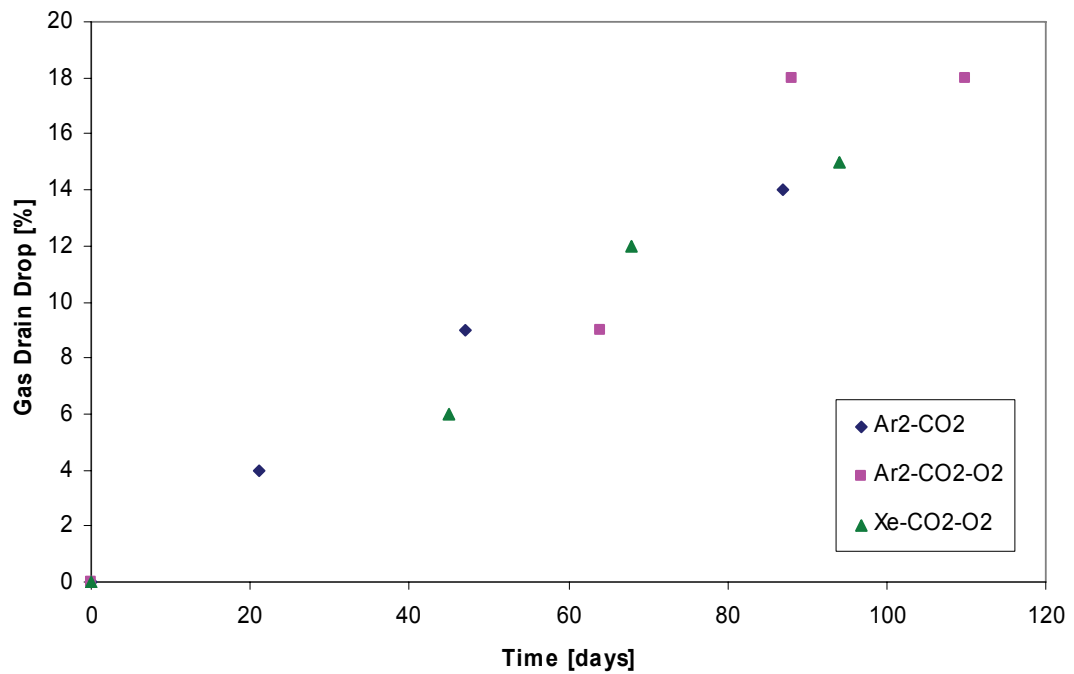


Figure 51: Aging rate dependency versus the gas mixtures: Ar-CO₂, Ar-CO₂-O₂, Xe-CO₂-O₂

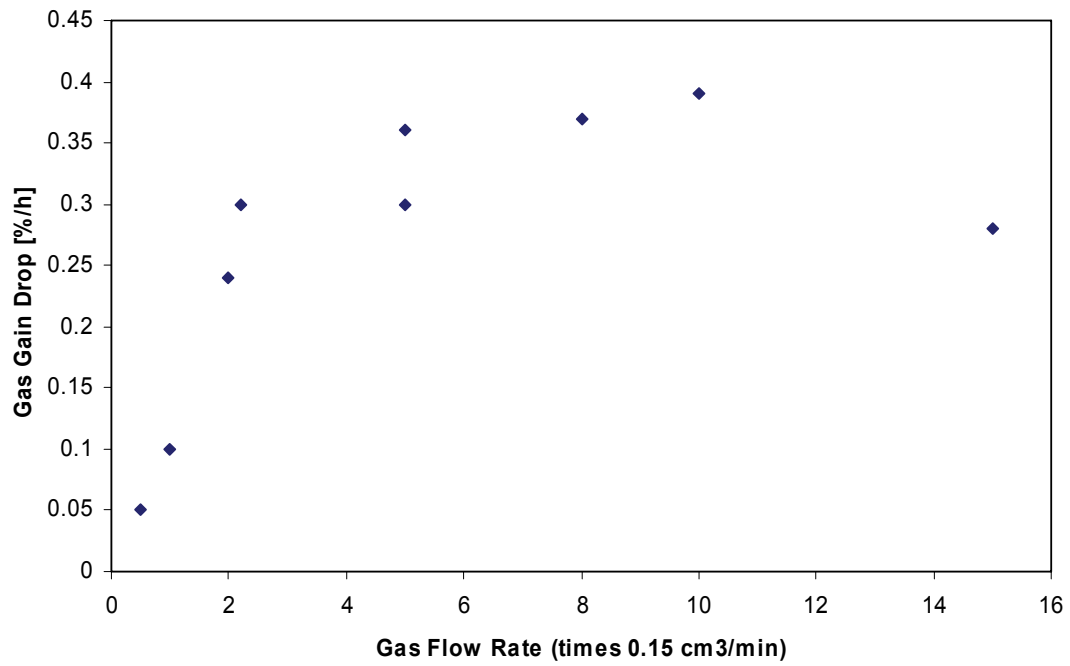


Figure 52: Aging rate dependency versus the gas flow rate in the straw (gas flow velocity)

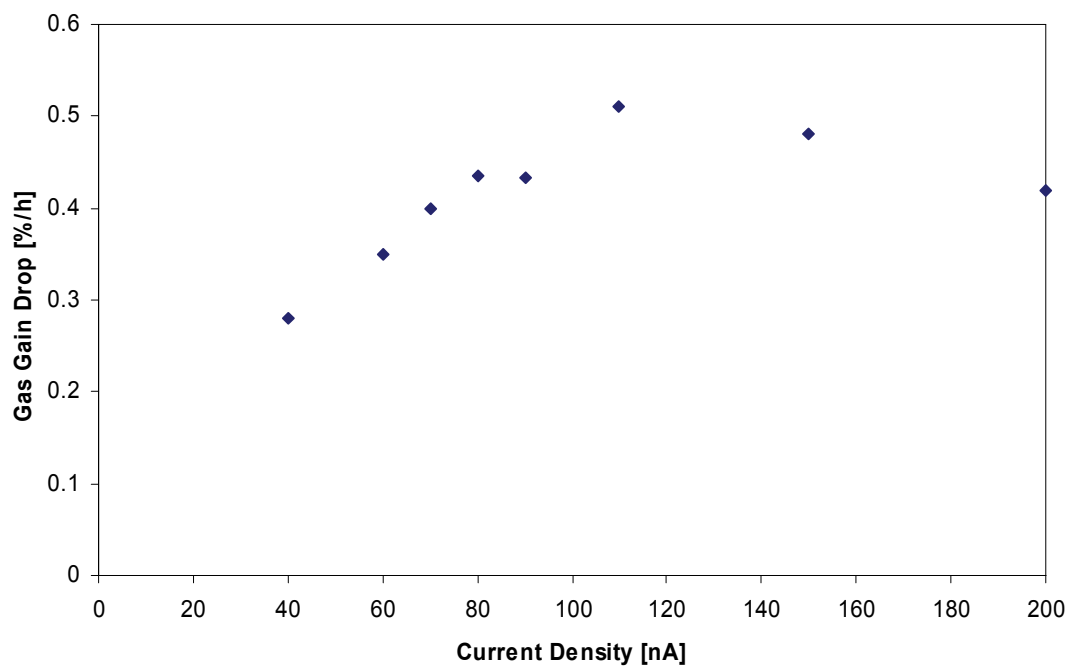


Figure 53: Aging rate dependency versus the current density per straw

6.2 Systematic Component Validation

A complex issue for the safe operation of gaseous detectors is the cleanliness of the gas supply system. Therefore components used to build the gas system have to be selected with care to avoid pollution of an initially clean gas mixture.

The TRT-consortium has consistently followed a strict validation policy for all components used in the gas system. A component is considered validated if, after performing an aging test with TRT straws, no aging is detected during ~200 hours of irradiation at 10 times the nominal gas flow rate and at a current density of 100 nA/cm. This test guarantees that the gas gain drop will be less than 2-3 % per year of TRT operation. An example of a validation test result with a rotameter which was rejected to use is shown in Figure 54. The gain drops by ~20% in 250 hours of irradiation, invalidating the use of this component in the TRT gas systems. Many other components, such as stainless steel pipes, electronic and mechanical flowmeters, valves, etc, have been inspected and validated in aging tests. Only components which have been validated as *clean* have been used for the assembly of the TRT gas system. A gas gain drop of 2-3% per year of TRT operation is certainly not enough to ensure the required 10 years lifetime, but for the case that aging appears the gas gain can be restored by operating the detector for a short period of time (~2 days) at LHC condition with the gas mixture Ar(70%)CO₂(26%)CF₄(4%).

This is possible because fluorine based radicals issued from the avalanche process are able to efficiently clean up aged wires. It has been found in a set of systematic measurements that about 30 cleaning days of the TRT modules can safely be performed with a CF₄ based gas mixture [24]. Thus one cleaning run per year, if needed, seems to be realistic. Typically a cleaning run would be performed during standard LHC operation, with controlled water content below 1000 ppm, and in gas flushing mode to avoid the pollution of the recirculation system.

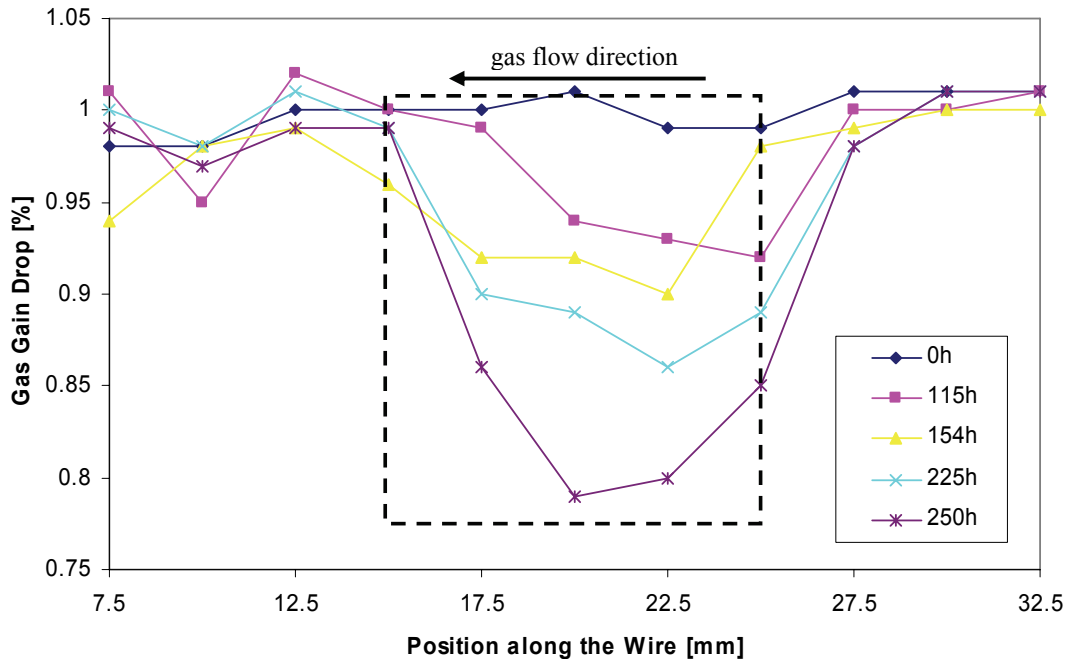


Figure 54: Aging test with a non-clean rotameter.

6.3 Principles and Guidelines

This section summarizes useful guidelines in order to avoid aging problems in wire chambers. The guidelines are based on experiments made in laboratory tests. Table 14 shows a list of *bad* and *good* materials or procedures, which were established in the context of aging studies [27]. This list relates to materials specifically considered for the TRT assembly and is therefore not complete. It should be noted that a clean gas system together with a supply of a very pure gas can reduce aging to small or negligible levels. Another approach is to place a filter upstream of the chamber, so only materials of the chamber itself can cause aging problems, and these can be more easily controlled.

Avoiding pollution during the assembly process requires the establishment of clean and safe methods for assembly and operation of the system (see chapter 6.3.1). These principles should be used to assemble, not only the final gas system, but also any system supplying gas during the production of modules at the various sites. Below the cleanliness specification for the TRT gas system components is listed:

General:

1. All pipes, fittings and components used in the gas systems have to be cleaned and degreased before installation. Cleaning must always happen before any assembly (even for tests). Cleaning has to be done in ultrasonic baths.

2. Gas system components must tolerate the presence of ozone in the system (100-200 ppm of O₃).
3. Some parts of the system will be exposed to CF₄ for a maximum of 30 days and the distribution system might be exposed to CF₄ disintegration products for the same period of time.

Components:

1. The components must be free from any traces of lubricant, particularly any silicon containing products.
2. Silicon containing O-rings, seals or joints must not be used.

Table 14: Recommendations for materials to be used in the TRT detector and gas systems

Materials		
Elastomers (Gas Seals)	preferred	EPDM, Viton, Teflon (not in contact with CF ₄)
	forbidden	any type of rubber, NBR, RTV
Metals	preferred	Stainless Steel, Copper, Brass
	forbidden	Al if there is a contact with the CF _n products.
Plastics	preferred	Very much recommended: ULTEM, PEEK+
	forbidden	
Thread Tightening	preferred	Teflon-Band (in absence of the CF _n products)
	forbidden	Any type Si-Joints
Glues	preferred	Araldite AW103, Tra-Bond 2115
	forbidden	Araldite AW106, RTV and similar products
Bubbler Oils	preferred	none, water or alcohol if needed
	forbidden	all Si containing and low pressure organic oils
Lubricants	preferred	to be avoided, use Krytox or Apiezon if needed
	forbidden	any other

6.3.1 Detector Assembly Procedure

Contamination during assembly can make all validation tests and cleanliness specification useless. As a general rule, the assembly area must be isolated from other manufacturing areas and clean room standards should be applied. Some equipment should be avoided or protected. Examples of contamination are tools with lubricated shafts, soldering or brazing equipment that requires heating of volatile fluxes, motors and vacuum pipes with outgassing oils. Another substantial source of contamination is the personnel. The people in the assembly need to be aware how sensitive the TRT is to pollution and that already little actions, like using once different O-rings because the established type is not available, can have a dramatic impact on the lifetime of the

detector. Therefore it is essential that the staff knows why something must be carried out in a certain manner and proper training is therefore needed. Examples of contamination are street clothing; hair, make-up, fingernail and fingerprints are source of oil and particularly many creams and cosmetics contain silicones. Therefore appropriate information and clear instructions will greatly reduce problems in the manufacturing.

The assembly process itself has to be well specified and stable. It should be rechecked periodically and only include proven improvements after careful observations of the process. A good assembly process includes cleanliness procedures of assembly components and its verification. Traceability is also an important feature, especially when building very large systems.

7 Concentration Measurements and Filter Development with a constant Si-Source

7.1 Constant Silicon Source

7.1.1 Introduction

In order to carry out concentration measurements and filter studies in a systematic way it is necessary to have a constant impurity source with an adjustable impurity level. Common silicon sources like polluted gas system components, silicon based oils, lubricants or greases have the disadvantage that:

- their outgassing rate is unknown and so is therefore also the resulting impurity concentration
- the outgassing rate might not be constant over the test period
- the concentration level is difficult to adjust

Therefore a constant silicon source has been developed on the basis of a capillary system, which enables us to produce gas mixtures with any demanded silicon concentration. Whereby hexamethyldisiloxane (HMDS) is used as silicon source. It is liquid and has a vapor pressure of about 100 mbar at 20°C.

7.1.2 HMDS as Representative for Real Impurities

For the development of a filter to remove organosilicon compounds from the working gas mixture it is essential that the used silicon source represents the real impurities in the TRT gas system. In chapter 5 polymethylsiloxane has been identified as the main substance of the impurities and as shown in Table 15 common materials used in gas systems consists of more than 75 – 85 % of methylsiloxane. The rest is an inorganic thickener that does not emit organosilicon compounds. Volatile silicon fluids have a vapor pressure of about 1 to 100 mbar at ambient temperature.

Therefore pure HMDS ($C_6H_{18}OSi_2$) has been chosen as impurity source. It is liquid with a vapor pressure of 100 mbar at 20 °C, has a moderate price and is easily available. The thermodynamic data of HMDS are summarized in chapter 4.2.

Table 15: Chemical composition of the grease Molycote 111 and the adhesive/sealant RTV 3145

Compound	Molycote 111 [Wt. %]	RTV 3145 [Wt. %]
Polydimethylsiloxane		> 60
Silica, amorphous		7 - 13
Dimethylsiloxane, hydroxy-terminated	> 60	7 - 13
Methyltrimethoxysilane	7 -13	
Trimethylated silica	15 -40	

7.1.3 Gas Flow through Capillaries

The relationship between linear pressure and flow as quantified by the Hagen-Poiseuille equation, for gas flow through a capillary is utilized in the design of the constant silicon source described in chapter 7.1.4. Capillaries with a few μm in diameter are specially adjusted for maintaining accurate gas flow rates in the range of $1 \times 10^{-4} - 100$ ml/min. Starting from very dilute gases four flow regimes are defined, depending on the Knudsen number and the Reynolds number [84]. The Knudsen number Kn is expressed as:

$$Kn = \frac{\lambda}{d}$$

Here λ is the mean free path and d the characteristic diameter. For example $\lambda = 60$ nm in air and 173 nm in helium at 1 bar. The Reynolds number Re can be calculated with the following equation:

$$Re = \frac{\rho u D}{\eta}$$

In the above equation ρ is the fluid density, u the flow velocity, η the viscosity and D the capillary diameter.

According to these numbers the flow regimes are divided into molecular, Knudsen, laminar and turbulent flow.

Molecular Flow:

The molecular flow regime describes the high dilute case where the mean free path is much larger than the characteristic dimensions of the system under consideration. In this regime the gas molecules are acting independent of each other and collide only with the walls of the system. Molecule – molecule collisions can be neglected. Typically, Kn is larger than 0,5.

Knudsen Flow:

This is the transition region where the mean free path of the molecules is similar to the dimensions of the system under consideration. The flow of the gas is governed by

viscosity as well as by molecular phenomena, this occurs at Knudsen numbers between 0,01 and 0,5.

Laminar Flow:

In this flow regime the gas can be characterized as a continuous, viscous and compressible medium. Laminar flow occurs at Knudsen numbers smaller than 0,01 and Reynolds numbers smaller than 2000. The inertial forces can be neglected compared to viscous forces.

Turbulent Flow:

Turbulent flow is a flow regime that is characterized by chaotic and stochastic property changes. Inertial forces play an important role. This flow regime occurs at Reynolds numbers between 2000 and 4000. The transition from laminar to turbulence is not at an exact Reynolds number and also depends on the geometry of the system.

To achieve the required flow rates the correct relationship between pressure ranges, capillary tube length and diameter must be determined. The pressure-flow relationship, in the laminar region, may be calculated by the Hagen-Poiseuille equation for cylindrical tubes for compressible media:

$$\dot{Q} = \frac{\pi R^4}{16\mu l} (P_2^2 - P_1^2)$$

Where \dot{Q} is the flow rate in [Pa m³/sec], P_2 the pressure at the inlet of the tube, P_1 the pressure at the outlet of the tube, R the tube radius, μ the dynamic viscosity and l the tube length. As it is desirable to have linear relation between pressure drop and flow, laminar flow must be maintained, i.e. the Reynolds number must not exceed 2000 and furthermore to avoid Knudsen flow the Knudsen number should be smaller than 0.01.

In order to calibrate the system 5 cm long capillaries with diameters of 2, 5 and 10 μm were investigated. The resultant flow over the applied pressure was measured using a soap bubble meter. In Figure 55, Figure 56 and Figure 57 the measured and calculated argon flow rate through capillaries of 2, 5 and 10 μm are illustrated respectively. For the 2 μm capillary the deviation between measurement and calculation is about 300 % over the pressure range. The accuracy of the 2 μm capillary is $\pm 1 \mu\text{m}$ and can be an explanation for the deviation as the radius has power 4 in the Hagen-Poiseuille equation. Therefore already slightly different radii have a strong influence in the resulting flow rates. The 5 and 10 μm capillaries have an accuracy of $\pm 2 \mu\text{m}$ and the deviation between the measured and calculated flow rates is about 40 and 70 % respectively. Generally, the results for measurements and calculations are getting closer with bigger capillaries because of the higher accuracy of the diameter. A further possible source of error is the diffusion of gas through the membrane in the soap bubble meter.

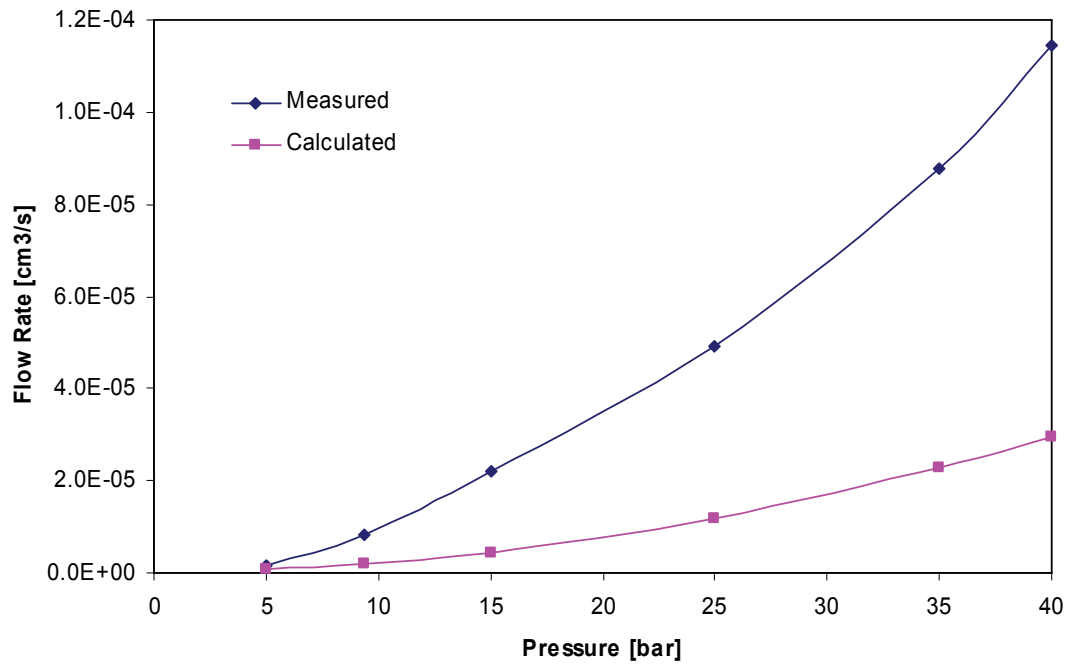


Figure 55: Measured and calculated argon flow rate through a 2 μm capillary as a function of the applied pressure

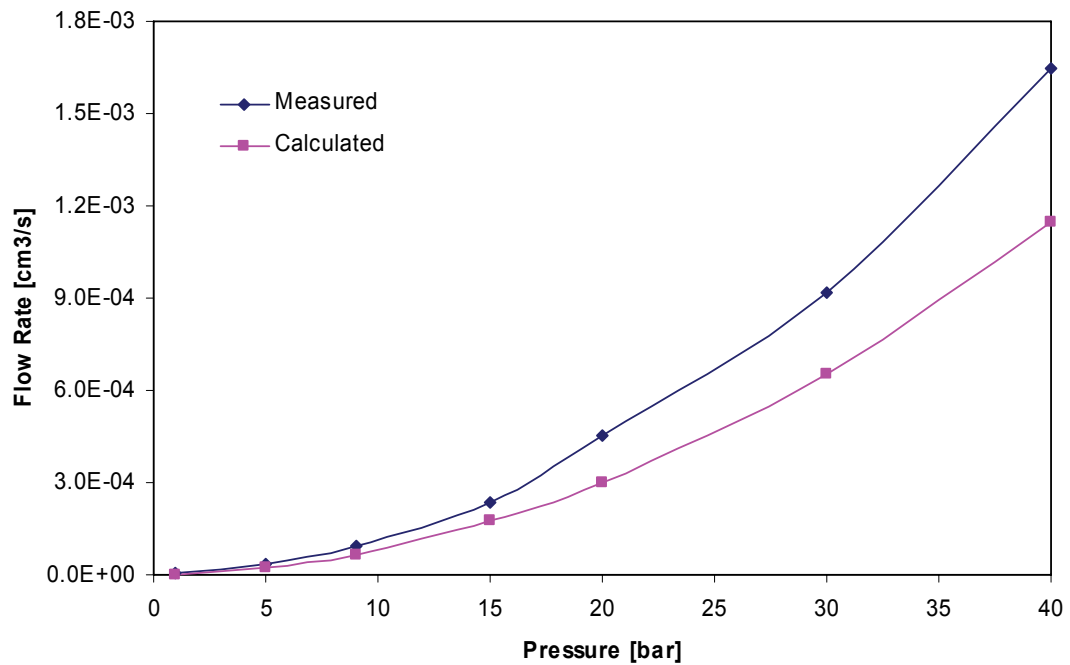


Figure 56: Measured and calculated argon flow rate through a 5 μm capillary as a function of the applied pressure

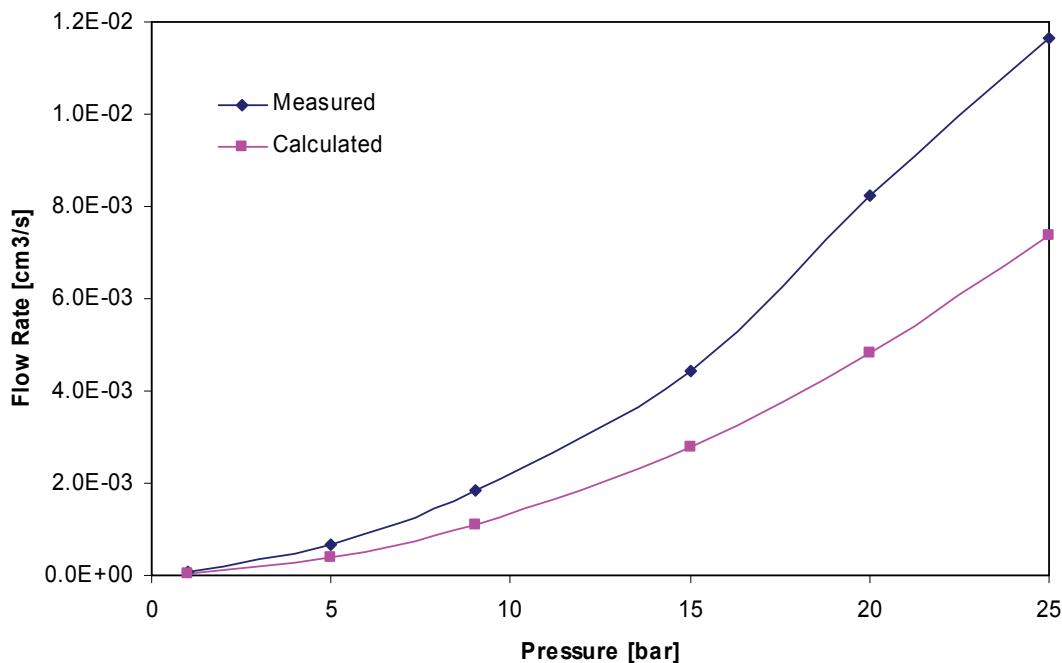


Figure 57: Measured and calculated argon flow rate through a 10 µm capillary as a function of the applied pressure

7.1.4 Test Setup with Constant Silicon Source

Figure 58 illustrates the test setup for concentration measurements and filter studies with a constant silicon source. To produce the required siloxane concentrations a very low gas flow of argon saturated with HMDS is fed via a capillary into the main gas line. The capillary is attached to a vessel with HMDS in liquid state that is pressurized by argon. A vapor-liquid equilibrium, depending on the temperature and pressure, is present in the vessel and the HDMS gas phase concentration can be calculated from its vapor pressure (see Figure 25). In order to achieve the required flow rates through the capillary the correct relationship between pressure ranges, capillary tube length and diameter must be determined. The pressure-flow relationship, in the laminar region, may be calculated by the Hagen-Poiseuille equation (see chapter 7.1.3). This system is highly flexible and allows the production of any demanded impurity concentration from ppt to ppm level. It is a low-cost alternative to mass flow metering systems and has the additional benefit of easy calibration to any required gas.

With the constant and known HDMS concentration in the main gas line filter studies and concentration measurements can be carried out. An irradiated straw prototype serves as HMDS detection instrument.

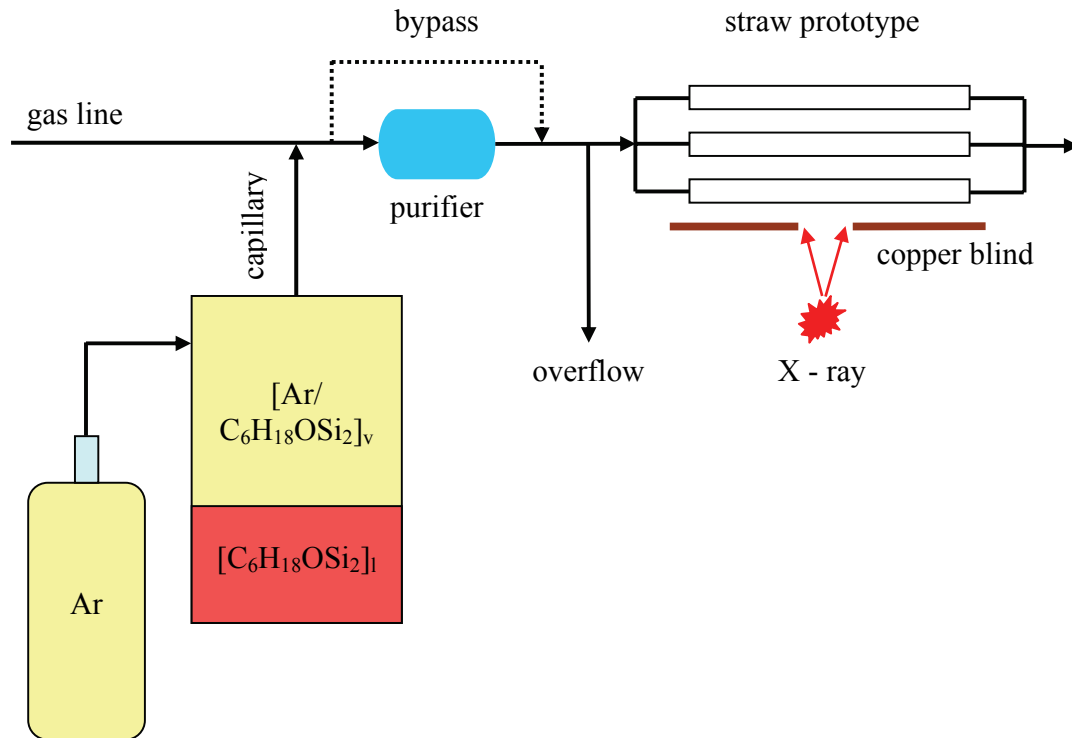


Figure 58: Illustration of a test setup with constant silicon source for concentration measurements and filter development studies

7.2 Concentration Measurements with the Constant Si Source

As described in chapter 6 a systematic component validation procedure has been carried out through aging tests with irradiated straw prototypes. These aging tests are qualitative and the only possible assertions are that a component is not, low, medium or highly polluted. Conclusions about the real impurity level are not possible. One purpose for the construction of the constant silicon source was to understand the relationship between aging rate and concentration level that would allow qualitative and quantitative considerations. Furthermore interesting questions like,

- What is the minimum detectable impurity level?
- What is the impurity level of common polluted gas system components?
- Is the aging rate linear versus the concentration level?

can be answered. The setup for the concentration measurements is shown in Figure 58, whereby the bypass is utilized for this kind of measurements. A capillary of 5 cm length and 2 μm diameter was used with an argon over-pressure of 1 bar in the vessel at 20 °C. The gas flow from the capillary has been fed into the main gas line to produce the desired

HMDS concentrations. Table 16 summarizes the resulting HMDS concentrations in the main gas line for different flow rates. In front of the prototype, the main gas line is split in such a way that only $1.5 \text{ cm}^3/\text{min}$ goes through each straw which corresponds to 10 times the nominal gas flow rate (as recommended in chapter 6.1). The tests have been performed at a current density of about 100 nA/cm . Figure 59 shows the aging rate dependency versus the HMDS concentration. It can be seen that the aging rate increases linear with the impurity level. The systematic accuracy of the concentration measurements is about $\pm 30 \%$. Comparing the results from Figure 59 with the aging test of a non-clean rotameter represented in Figure 54 it can be concluded that the impurity level produced by the rotameter is about 1 ppb. The rotameter has been classified as medium polluted by the aging test. Consequently, a medium polluted gas component can be expected to produce an impurity level of about 1 ppb.

In chapter 6.2 it has been defined that a component is considered validated if no amplitude drop is detected during ~ 200 hours of irradiation. The signal amplitude measurement accuracy in these tests is ± 1 percent. Therefore it can be assumed that the produced impurity level of validated gas system components is below 0.1 ppb because this concentration would result in a gas gain drop of about 2 % in 200 hours (see Figure 59). This information is of fundamental importance for the dimensioning and maintenance of filters.

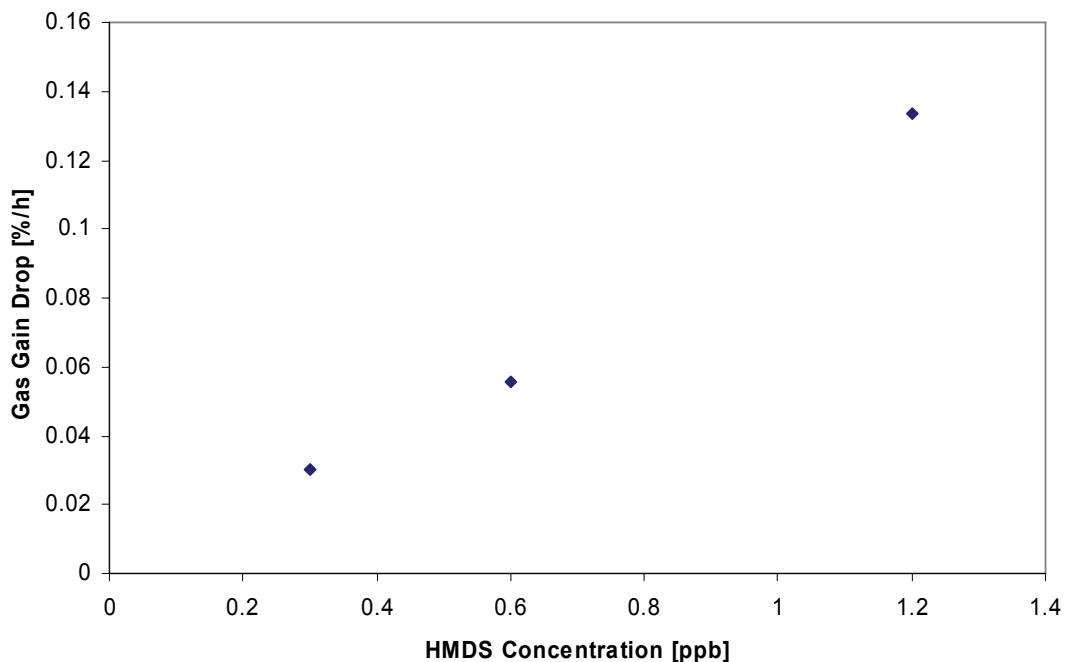


Figure 59: Aging rate at different impurity concentrations produced with a constant HMDS source.

Table 16: HMDS concentration levels in the main gas line for different flow rates (capillary of 5 cm length and 2 μm diameter, 1 bar argon over-pressure in vessel, 20 °C)

Over-Pressure [bar]	V _{main} [l/h]	C _{HMDS} [ppb]
1	20	0.3
1	10	0.6
1	5	1.2

7.3 Filter Studies

The removal of organosilicon impurities from the TRT working gas is of high importance to guarantee the required 10 years lifetime of the detector. Hence various experiments have been performed to investigate the capability of different gas purification principles. Chapter 7.3.1 describes experiments done with a catalytic converter and adsorption processes are examined in chapter 7.3.2 and 7.3.3.

Packed bed adsorption has been selected for the purification of the TRT working gas and therefore the adsorption capacity of several materials has been determined. As discussed earlier, the adsorption capacity of a material is crucially important in the design of adsorbers and cyclic separation processes. The adsorptive concentration in the flow at any given point in the bed is a function of time, resulting from the movement of the concentration front in the bed. The shape or width of the breakthrough curve designates the separation efficiency, whereby a sharp concentration front is desirable. However, through the limitations of the organosilicon detection by an irradiated straw prototype the shape of the breakthrough curve cannot be determined. Only the time of breakthrough can be indicated by a gas gain drop in the irradiated area of the straw prototype. Nevertheless the adsorption capacity of a material can be estimated from these measurements.

7.3.1 Catalytic Conversion of Objectionable Impurities Measured with the PTR-MS

The connection of a catalytic converter (platinum wool catalyst) in series between the outlet of a non-clean rotameter and the PTR-MS inlet clearly shows the potential of such a device for removing organic compounds in the carrier gas, as can be seen from the mass spectrum in Figure 62. A clean stainless steel tube was initially tested without the rotameter attached to determine the system background shown in Figure 60. Thereafter a non-clean rotameter has been attached and the mass spectrum shown in Figure 61 illustrates the presence of many high-mass peaks. Subsequently the catalytic converter has been introduced after the rotameter and the lack of masses seen at the high-mass end of the scale can be observed. Some peaks at high ion masses are still present in the mass spectrum in Figure 62 however their amplitude is slowly decreasing proofing their efficient oxidation in the catalytic converter. It has to be noted that these measurements

were made using synthetic air as carrier gas. The working temperature of the catalytic converter was set at 300 °C.

The principle of catalytic conversion is described in detail in chapter 4.3.2.

Results:

The successful removal of organosilicon compounds from a carrier gas by a catalytic converter has been demonstrated in Innsbruck, Austria. A disadvantage is that the working temperature of about 200 – 300 °C would require additional design features in the TRT gas system.

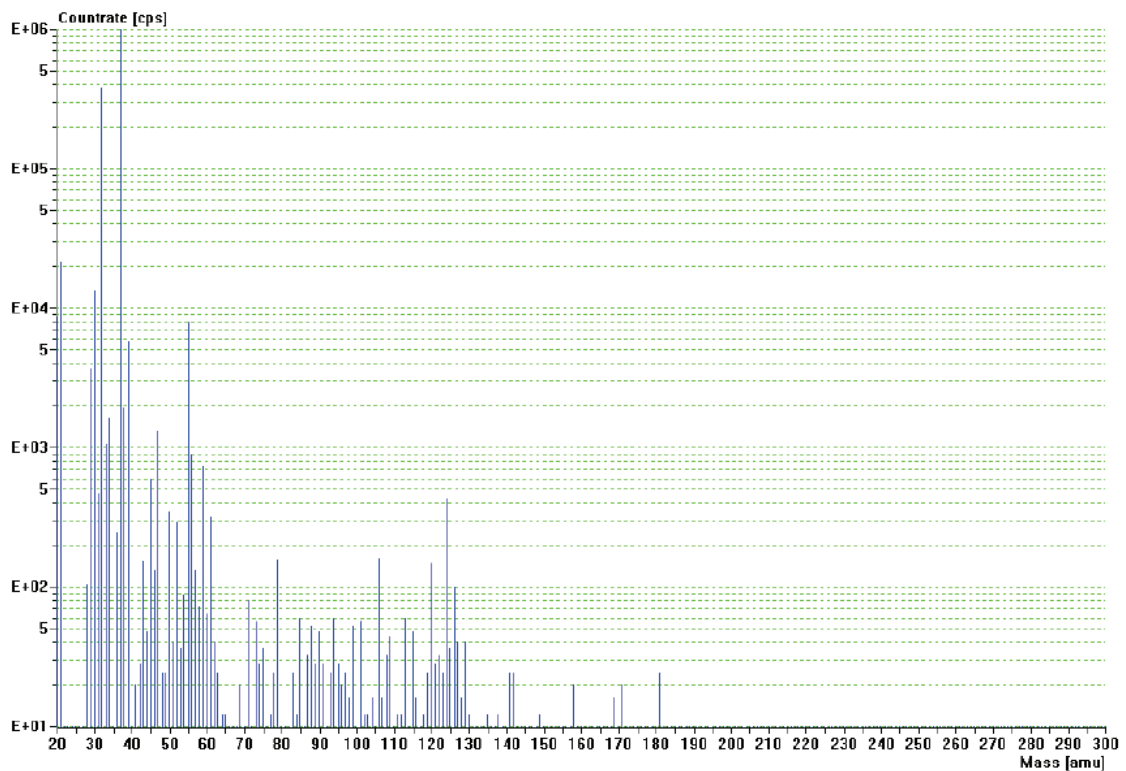


Figure 60: Mass spectrum of a stainless steel tube

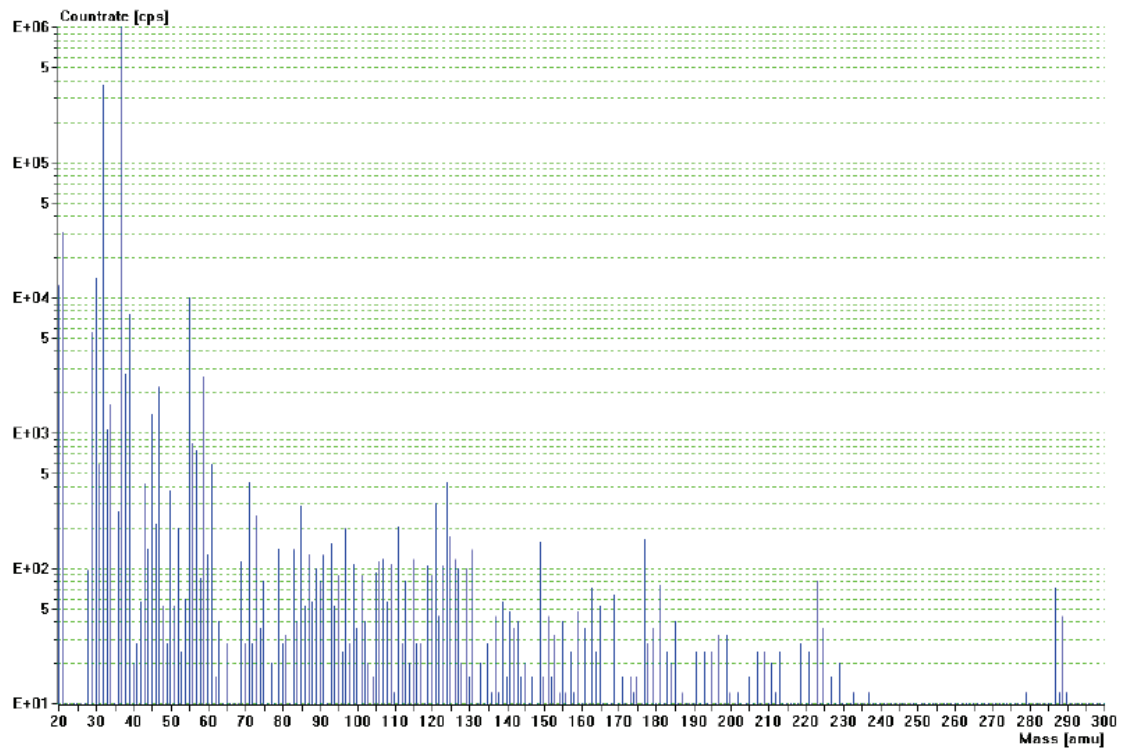


Figure 61: Mass spectrum of a non-clean rotameter

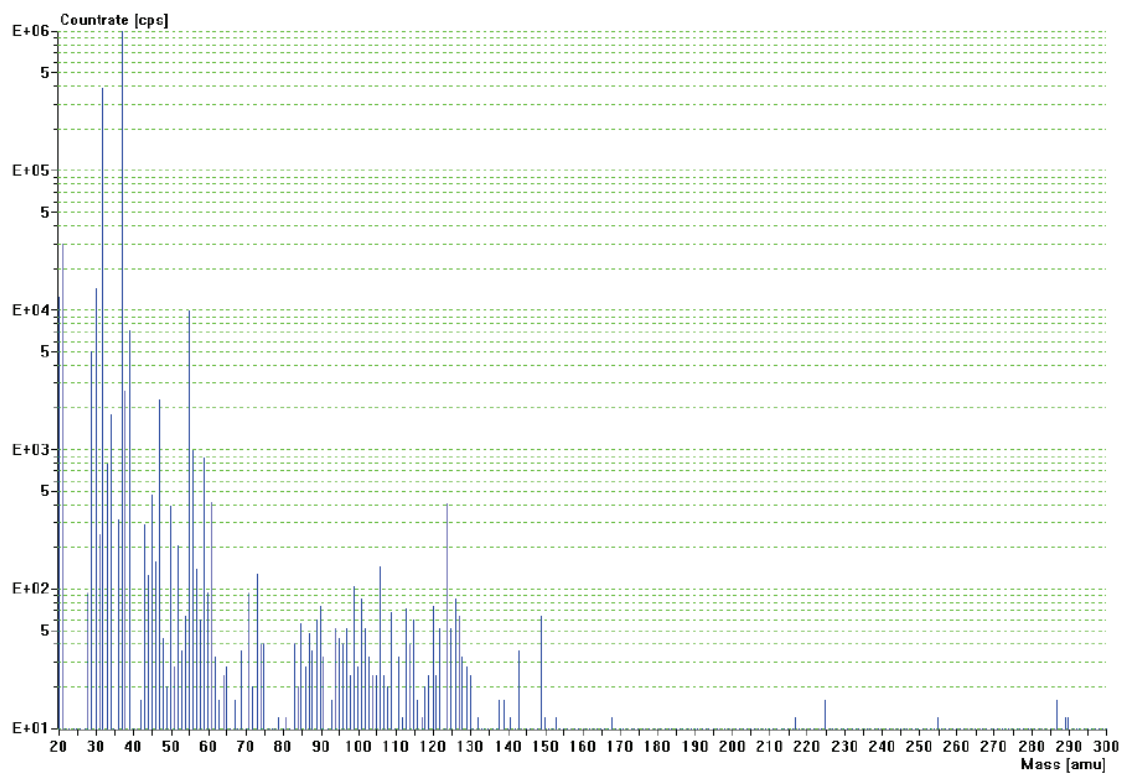


Figure 62: Mass spectrum with a catalytic converter connected in series between the rotameter outlet and the PTR-MS inlet

7.3.2 Adsorption Measurements with an Aeronex Standard Filter

The adsorption capacity of an AERONEX atmospheric gas purifier for HMDS has been examined at CERN. According their specifications, these purifiers remove gaseous contaminants like H₂O and non-methane hydrocarbons to levels as low as 1 ppb. Unlike older resin technologies, the new types should not contain hydrocarbons that outgas during normal or setup conditions. The purification material operates at ambient temperature so no additional power or heat is required. The gas separation process is based on adsorption of contaminants on a proprietary specialty zeolite mixture with the advantage that the material is regenerable. Flow rates and prices of the atmospheric gas purifier series are listed in Table 20 and some features are summarized below [86]:

- purifies CO₂, CDA (Air)
- removes H₂O and non-methane hydrocarbons
- < 1 ppb outlet purity
- specialty zeolite mixture
- operates at ambient temperature (-40 to 65 °C)
- does not release hydrocarbons
- no heat or power required
- regenerable

Experiment:

For the adsorption test the purifier type CE-35KF-A-4R has been connected in series between a constant HMDS source and an irradiated straw prototype. The experimental setup is illustrated in Figure 58. A detailed specification of the purifier can be found in Table 19 and the outline drawing is shown in Figure 64. The gas flow rate of Ar(70%)CO₂(30%) through the purifier was 5 l/h and has been split in front of the straw prototype in such a way that only 1.5 cm³/min goes through each straw which corresponds to 10 times the nominal gas flow rate (as recommended in chapter 6.1). The test was carried out at a current density of about 100 nA/cm. In Table 17 the operating parameters of the constant HMDS source are summarized. A 10 μm capillary with a length of 5 cm has been used. The argon over-pressure was 1 bar for the first 638 hours resulting in a HMDS concentration of 1 ppm in the main gas line and 10 bar the following 1246 hours causing 6.2 ppm. As no gas gain drop could be observed during 638 hours at 1 ppm, demonstrating that the gas after the purifier is free of HMDS traces, the concentration has been increased to accelerate the test. After a total of 1888 hours the first indications of a gas gain drop could be observed, whereas 60 hours later the amplitude drop was 15 % and the test has been stopped (see Figure 63). For calculating the adsorption capacity the moment with the first indications of an amplitude modification (i.e. 1888 hours) is significant. The adsorbent mass is unknown and need to be estimated from the outer dimensions of the purifier and by assuming an adsorbent density of about 500 kg/m³ which is an average value for common zeolite materials. From these estimations an adsorption capacity of 0.013 g_{HMDS}/g_{Adsorbent} can be determined (see Table 18).

Similar adsorption capacities of zeolite materials for volatile organic compound are mentioned in the literature. For instance in [87] where breakthrough curves are ascertained for a zeolite (Na-ZSM-5/180 - MFI structure) packed bed with a complex organic gas mixture. It consisted of methanol (MeOH), methylethylketon (MEK), p-xylol, toluol and n-pentan, each with a concentration of 1000 ppm in helium as carrier gas. If present the water concentration was 1425 ppm. Figure 65 shows the breakthrough curves obtained with and without the presence of water in the gas mixture. It can be seen that the breakthrough of the different compounds happens almost at the same time in the gas mixture without water. The breakthrough curve with water shows the hydrophobic property of Na-ZSM-5/180. Water is saturated first but it doesn't influence the adsorption characteristic of most of the other compounds. Only the adsorption capacity of methanol is slightly reduced. From these measurements an adsorption capacity of $0.01 \text{ g}_{\text{MeOH}}/\text{g}_{\text{Adsorbent}}$ and $0.03 \text{ g}_{\text{Xylol}}/\text{g}_{\text{Adsorbent}}$ can be determined. Taking into account that the molecular weight of HMDS (162 g/mol) is 5 times higher than that one of methanol (32 g/mol), a slightly earlier breakthrough for HMDS can be expected.

Results:

The successful adsorption of organosilicon compounds from a carrier gas by an AERONEX atmospheric gas purifier has been demonstrated. The adsorption capacity determined is $0.013 \text{ g}_{\text{HMDS}}/\text{g}_{\text{Adsorbent}}$.

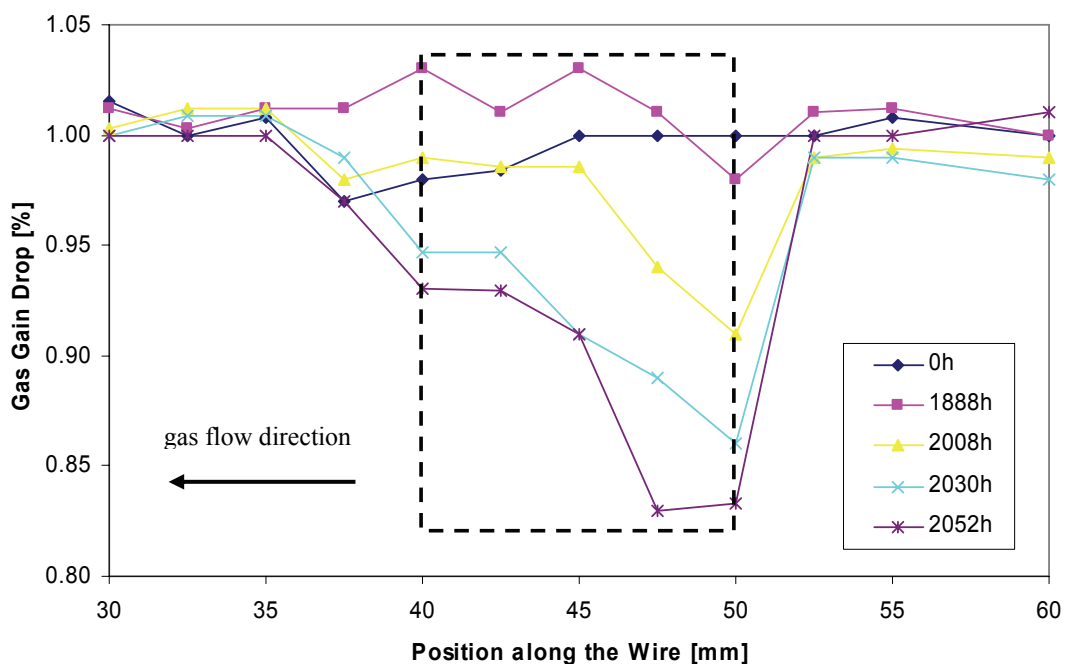


Figure 63: Aging test with an AERONEX standard filter connected in series between a constant HMDS source and an irradiated prototype

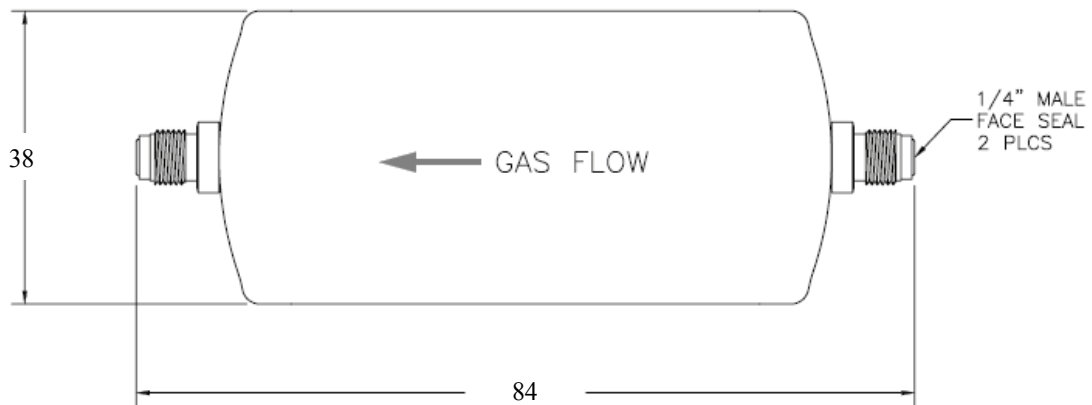


Figure 64: Outline drawing of the AERONEX purifier type CE-35KF-A-4R [86]

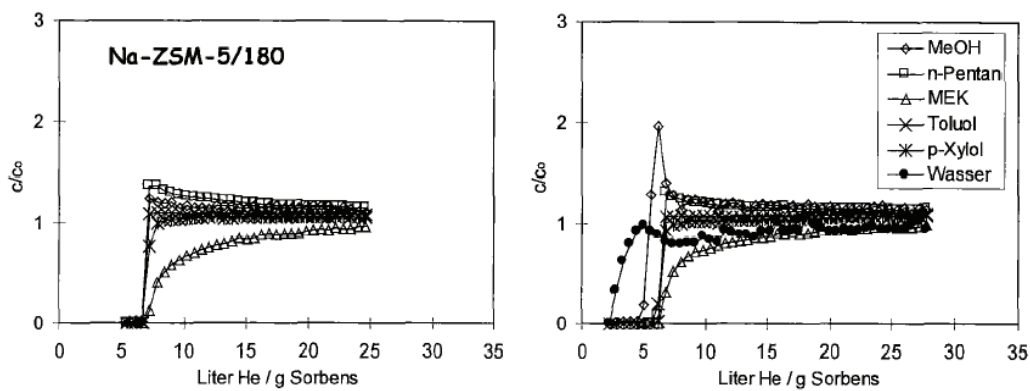


Figure 65: Breakthrough curves for a complex gas mixture with a zeolite Na-ZSM-5/180 packed bed adsorber – LEFT: mixture without water, RIGHT: mixture with water [87]

Table 17: Operating parameters of a constant HMDS source for adsorption measurements with an AERONEX purifier type CE-35KF-A-4R

HMDS Concentration [ppm]	2	6.3
Operating Time [h]	638	1246
Capillary Diameter [μm]	10	10
Capillary Length [cm]	5	5
Main Gas Flow [l/h]	5	5
Over-Pressure [bar]	1	10
Temperature [$^{\circ}\text{C}$]	20	20

Table 18: Adsorbent parameters for the AERONEX purifier type CE-35KF-A-4R

Outer Purifier Volume [cm ³]	95.3 ¹
Estimated Adsorbent Volume [cm ³]	48 ²
Adsorbent Density [kg/m ³]	500 ³
Adsorption Capacity [g _{HMDS} /g _{Adsorbent}]	0.013 ⁴

Table 19: Specification table for the AERONEX purifier type CE-35KF-A-4R [86]

Maximum Flow Rate [slpm]	1
Pressure Drop at 1 slpm [bar]	0.035
Max. Delta Pressure [bar]	13.8
Max. Housing Pressure [bar]	200
Outlet Filter [μm]	0.003
Length [mm]	84
Diameter [mm]	38
Weight [kg]	0.3

Table 20: Examples for flow rates and prices of AERONEX atmospheric gas purifiers [86]

Maximum Flow Rate [slpm]	Type	Price excl. Tax ⁵ [Eur]
1	CE-35KF-A-4R	830
60	CE-500KF-A-4R	2639
300	CE-2500KF-A-4R	4990
1000	CE-10MF-A-8Y	19800

7.3.3 Adsorption Measurements with Self-Made Filters

The adsorption capacity of organosilicon compounds for two porous materials has been investigated at CERN with self made packed bed adsorbents. A zeolite material type UY8 [89] and a catalyst named TIMIS [90] were examined. Ideally the tests should be performed at the expected impurity level of a few ppb (see chapter 5.2.2 and 7.2). Through the high adsorption capacity of the materials this concentration level would require either very little adsorbent volumes which are difficult to handle with the given instrumentation at CERN or very long test durations of several 1000 hours. Therefore a HMDS concentration of 1 ppm has been chosen for the experiments discussed in chapter 7.3.3.1 and 7.3.3.2.

¹ Volume calculated by the outer dimensions of the purifier given in Table 19.

² Estimated adsorbent volume for capacity calculation.

³ Average value for zeolites, the real density of the adsorbent is unknown.

⁴ Estimated value as the adsorbent mass is unknown.

⁵ Prices are from 2004.

7.3.3.1 Zeolite Packed Bed Adsorber

This test has been made to understand the adsorption properties of a self-made zeolite filter. The examined material is the zeolite UY8 received from the company Bad Köstritz in Germany [89] and the packed bed dimensions have been determined by applying the guideline given in chapter 4.4.8.

Self-Made Filter:

According the instrumentation in the laboratory an Ar(70%)CO₂(30) flow rate of 5 l/h has been chosen. A stainless steel pipe with an inner diameter of 6 mm is utilized as vessel for the adsorber bed. This results in a superficial velocity, v_{fo} of:

$$v_{fo} = 0.05 \frac{m}{s}$$

The product of the superficial velocity, v_{fo} , and the fluid density, ρ_f , for this case is:

$$v_{fo} \sqrt{\rho_f} = 0.064$$

This number is close to the lower border of the recommended value and adequate for this adsorption test. For a high adsorbent efficiency the ratio between the bed and particle diameter should be bigger than 10. Therefore the zeolite beads with their original diameter of 5-8 mm have been chopped up and classified at the University of Technology Vienna. 0.63 g zeolite material with a particle size between 0.4-0.5 mm has been used for this experiment. The price of this adsorbent is 10 Eur/kg. A compressed bed of polyethylene fibers with a height of about 1 cm at the inlet and outlet of the adsorber kept the zeolite material in the vessel and worked as a dust filter. The adsorber parameters are summarized in Table 21.

It needs to be mentioned that no thermal treatment of the zeolite material has been done! A thermal treatment could possibly increase the adsorption capacity.

Table 21: Parameters of the self-made zeolite packed bed adsorber

Adsorbent Type	UY8
Main Flow Rate [l/h]	5
Vessel Inner Diameter [mm]	6
Height of Bed [mm]	47.5
Adsorbent Mass [g]	0.63
Adsorbent Density [g/cm ³]	0.47
Particle Size [mm]	0.4-0.5
Adsorbent Price [Eur/kg]	10

Experiment:

For the adsorption test the self-made zeolite packed bed adsorber has been connected in series between a constant HMDS source and an irradiated straw prototype. The experimental setup is illustrated in Figure 58. The main gas flow of 5 l/h through the purifier has been split in front of the straw prototype in such a way that only 1.5 cm³/min goes through each straw which corresponds to 10 times the nominal gas flow rate (as recommended in chapter 6.1). The test was carried out at a current density of about 100 nA/cm. In Table 22 the operating parameters of the constant HMDS source are summarized. A 10 µm capillary with a length of 5 cm has been used. The argon over-pressure was 1 bar for the first 500 hours resulting in a HMDS concentration of 1 ppm in the main gas line and 5 bar the following 261 hours causing 3 ppm. As no gas gain drop could be observed during 500 hours at 1 ppm, demonstrating that the gas after the purifier is free of HMDS traces, the concentration has been increased to accelerate the test. No gas gain drop could be observed up to 761 hours, but 75 hours later the amplitude dropped by approximately 40 % and the test has been stopped (see Figure 66). Amplitude scans between 761 hours and 836 hours are missing. Therefore 761 hours are used as reference for calculating an adsorption capacity of 0.074 g_{HMDS}/g_{Adsorbent}.

Results:

The successful adsorption of organosilicon compounds from a carrier gas by a self-made zeolite packed bed adsorber has been demonstrated. The adsorption capacity determined for the zeolite type UY8 from the company Bad Köstritz is 0.074 g_{HMDS}/g_{Adsorbent}. A purifier for a gas flow rate of 1 slpm would require approximately 25 g adsorbent which would cost 0.25 Eur.

Table 22: Operating parameters of a constant HMDS source for adsorption measurements with a zeolite packed bed adsorber

HMDS Concentration [ppm]	1	3
Operating Time [h]	500	261
Capillary Diameter [µm]	10	10
Capillary Length [cm]	5	5
Over-Pressure [bar]	1	5
Temperature [°C]	20	20

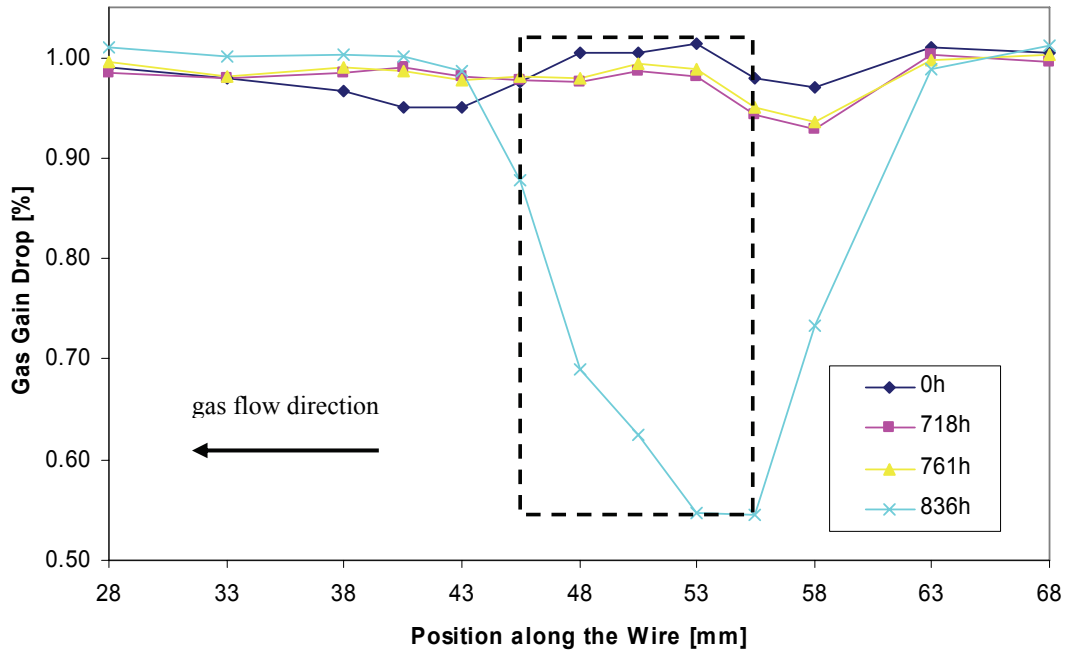


Figure 66: Aging test with a self-made zeolite filter connected in series between a constant HMDS source and an irradiated prototype

7.3.3.2 TIMIS Packed Bed Adsorber

This test has been made to understand the adsorption properties of a self-made adsorber with a catalyst named TIMIS as adsorbent [90]. The material consists of manganese oxide, copper oxide and nickel monoxide on the base of aluminum silicate. It has been received from the Moscow State University and its original purpose was the removal of ozone by catalytic processes from the TRT gas system. The packed bed dimensions have been determined by applying the guideline given in chapter 4.4.8.

Self-Made Filter:

According to the instrumentation in the laboratory an Ar(70%)CO₂(30) flow rate of 5 l/h has been chosen. A stainless steel pipe with an inner diameter of 6 mm is utilized as vessel for the adsorber bed. This results in a superficial velocity, v_{fo} of:

$$v_{fo} = 0.05 \frac{m}{s}$$

The product of the superficial velocity, v_{fo} , and the fluid density, ρ_f , for this case is:

$$v_{fo} \sqrt{\rho_f} = 0.064$$

This number is close to the lower border of the recommended value and adequate for this adsorption test. For a high adsorbent efficiency the ratio between the bed and particle diameter should be bigger than 10. In this experiment pellets with a diameter of 1 mm and a length of 2-6 mm are used and the guideline can not be applied directly. Therefore the adsorber length has been increased to about 4 times the minimum recommended length to avoid negative effects like axial dispersion or channeling. The minimum recommended adsorber height is defined as:

$$\frac{bed_height}{bed_diameter} \approx 5$$

3.41 g TIMIS material with a density of 0.93 g/cm³ has been used for this experiment. A compressed bed of polyethylene fibers with a height of approximately 1 cm at the inlet outlet of the adsorber kept the adsorbent in the vessel and worked as a dust filter. The adsorber parameters are summarized in Table 23.

It needs to be mentioned that no thermal treatment of the TIMIS material has been done! A thermal treatment could possibly increase the adsorption capacity.

Table 23: Parameters of the self-made TIMIS packed bed adsorber

Adsorbent Type	TIMIS
Main Flow Rate [l/h]	5
Vessel Inner Diameter [mm]	6
Height of Bed [mm]	130
Adsorbent Mass [g]	3.41
Adsorbent Density [g/cm ³]	0.93
Pellet Diameter [mm]	1.0
Pellet Length [mm]	2-6

Experiment:

For the adsorption test the self-made TIMIS packed bed adsorber has been connected in series between a constant HMDS source and an irradiated straw prototype. The experimental setup is illustrated in Figure 58. The main gas flow of 5 l/h through the purifier has been split in front of the straw prototype in such a way that only 1.5 cm³/min goes through each straw which corresponds to 10 times the nominal gas flow rate (as recommended in chapter 6.1). The test was carried out at a current density of about 100 nA/cm. In Table 24 the operating parameters of the constant HMDS source are summarized. A 10 µm capillary with a length of 5 cm has been used. The argon overpressure was 1 bar for the first 383 hours resulting in a HMDS concentration of 1 ppm in the main gas line and 5 bar the following 673 hours causing 3 ppm. As no gas gain drop could be observed during 383 hours at 1 ppm, demonstrating that the gas after the purifier is free of HMDS traces, the concentration has been increased to accelerate the test. First indications for an amplitude modification could be observed after 1056 hours, whereas 30 hours later the gas gain drop was already 15 % and the test has been stopped (see Figure

67). From this experimental data an adsorption capacity of $0.026 \text{ g}_{\text{HMDS}}/\text{g}_{\text{Adsorbent}}$ can be determined.

Results:

The successful adsorption of organosilicon compounds from a carrier gas by a self-made TIMIS packed bed adsorber has been demonstrated. The adsorption capacity determined for the TIMIS material from the Moscow State University is $0.026 \text{ g}_{\text{HMDS}}/\text{g}_{\text{Adsorbent}}$.

Table 24: Operating parameters of a constant HMDS source for adsorption measurements with a TIMIS packed bed adsorber

HMDS Concentration [ppm]	1	3
Operating Time [h]	383	673
Capillary Diameter [μm]	10	10
Capillary Length [cm]	5	5
Over-Pressure [bar]	1	5
Temperature [$^{\circ}\text{C}$]	20	20

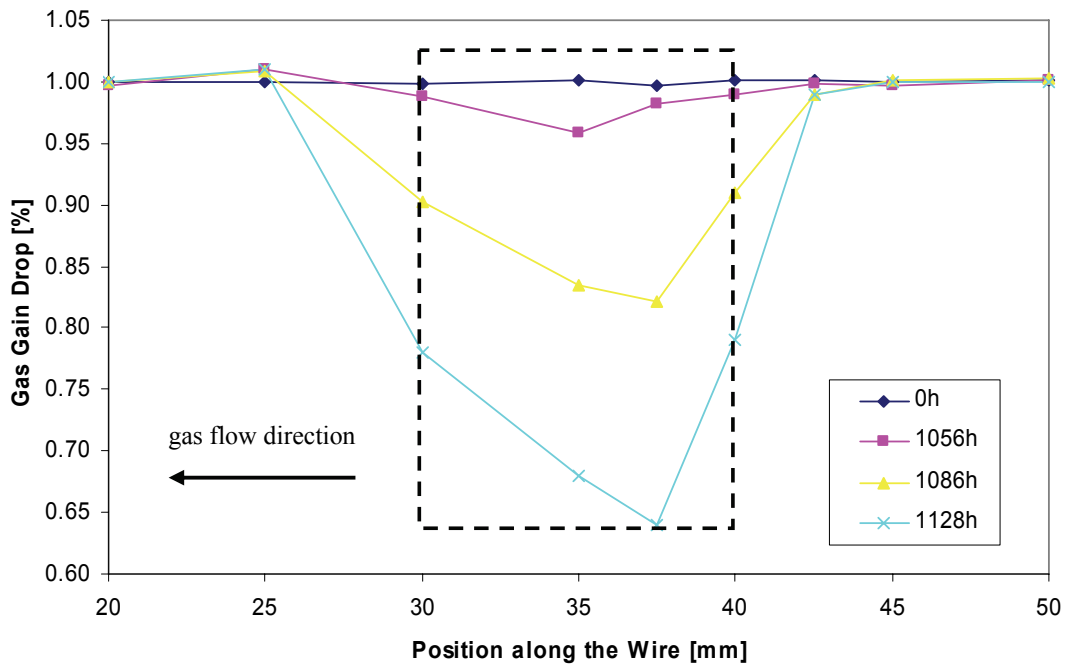


Figure 67: Aging test with a Self-Made TIMIS filter connected in series between a constant HMDS source and an irradiated prototype

7.3.4 Summary of the Adsorption Measurements

The results of the adsorption measurements performed in chapter 7.3.2 and 7.3.3 are summarized in Table 25. The highest adsorption capacity was determined for the zeolite

UY8 but also the TIMIS material which is originally used to remove ozone by catalytic processes shows a high adsorption capacity for organosilicon compounds. The outcome with the Aeronex standard filter needs to be considered with care because the real adsorbent mass is unknown. It has to be mentioned that the results for the zeolite ZSM-5 are taken from [87] and that the capacity is calculated for xylol.

Table 26 presents the parameters for a self-made purifier for the TRT active gas system. The packed bed dimensions have been determined by applying the guideline given in chapter 4.4.8. With a density of 470 kg/m^3 about 2.6 kg zeolite will be needed for the calculated volume. Taking into account a very conservative assumption for the impurity level in the TRT active gas system of approximately 10 ppb the purifier will have a lifetime of 101 years with negligible adsorbent costs of 26 Eur.

Regeneration is possible and has been examined at CERN but it will most likely not be performed as the adsorption capacity is very high and the price of the material is very low.

Table 25: Summary of the adsorption measurements

Adsorbent	Capacity [g _{HMDS} /g _{Adsorbent}]	Regeneration.	Comment
Zeolite UY8	0.074	OK	Particle Size 0.4-0.5 mm
TIMIS	0.026	OK	Pellets d = 1.0 mm, l = 2-4 mm
Aeronex Zeolite Mixture	0.013 ¹	OK	Standard Filter CE-35KF-A-4R
Zeolite ZSM-5 ²	0.03 ³	OK	Particle Size 0.25-0.5 mm

Table 26: Parameters of a zeolite UY8 purifier for the TRT gas system

Gas Flow [m ³ /h]	3
Impurity Level [ppb]	10
Bed Diameter [mm]	100
Bed Height [mm]	700
Bed Mass [kg]	2.6
Pressure Drop [mbar]	2.5 ⁴
Lifetime [years]	101
Adsorbent Price [Eur/kg]	10

¹ This value is calculated with an estimated adsorbent mass.

² This material was not examined at CERN the results are from [87]

³ This is the adsorption capacity for xylol.

⁴ Calculated pressure drop for the packed bed without dust filter at the outlet.

7.4 Maintenance

The adsorbers are designed to remove organosilicon trace impurities from the TRT active gas system. The efficiency of this adsorption unit can be affected by a number of process parameters which may be within the control of the operator. The purifiers will be designed for a lifetime of several years. If regeneration cycles are performed the mass transfer rate, and the equilibrium capacity will both decrease with the number of regenerations. The attainable lifetime of an adsorbent generally depends on the feed composition and the regeneration conditions.

It is normal for the pressure drop to increase by a factor of two to three over the lifetime of the purifier. This is due to the accumulation of normal dirt as well as the build up of coke on the bed. There will also be some powdering of the adsorbent due to bed movements as a result of temperature and pressure changes in the unit.

A simple test to determine the activity of a molecular sieve is described by [88] as follows: Take 10 g of an active molecular sieve. This may be a sample direct from the adsorber, or if the conditions are not known and it may have adsorbed moisture it should be heated at 200 °C for 2 hours. Then cool the sample to ambient temperature, add it to 10 ml of water with 20 °C and stir well. Heat will evolve. Measure the maximum temperature whereby a minimum temperature increase of 35 °C is recommended for the reuse of a molecular sieve.

8 Summary

The original gas mixture, Xe(70%)CF₄(20%)CO₂(10%), was found to etch the glass wire-joints inside the long barrel straws to the point of breakage by fluorine radicals. Therefore, this gas mixture was replaced by Xe(70%)CO₂(27%)O₂(3%) which provides acceptable operational stability and equivalent physics performance. Furthermore, it is less reactive, corrosive and material destroying. The original gas mixture however had the advantage that the CF₄ radicals effectively prevented the formation of hydrocarbon and SiO_x wire deposits. With the new gas mixture the TRT became much more sensitive to organosilicon impurities because oxygen radicals created in the gas avalanche can only prevent hydrocarbon wire deposits, but not silicon based ones. Even small concentrations of certain gaseous constituents can have very dramatic effects upon the rate of wire aging. These impurities result from outgassing processes of silicon based materials in contact with the gas.

Identification of Source and Composition of Impurities:

Different techniques were used to identify the source and the composition of the aging causing impurities in the TRT gas system. Surface analyses of aged wires were performed with scanning electron microscopy (SEM) and energy dispersive X-ray (EDX) spectroscopy. These analyses showed needle like deposits that consist of the chemical elements C, O and Si. Thus organosilicon deposits can be assumed whereby the carbon content of the deposit represents alkyl groups (most likely methyl groups). Conclusions about the gas phase impurity composition and concentration are not possible by SEM and EDX measurements. Therefore gas phase and chemical analyses have been performed.

Gas phase analyses were carried out with the proton-transfer-reaction mass spectrometer (PTR-MS) that was developed at the *University of Innsbruck - Institut für Ionenphysik* for online measurements of volatile organic trace components with concentrations as low as pptv up to a time response of 0.1 second. These measurements have clearly shown that organosilicon compounds, namely polymethylsiloxanes, are present in the gas phase. Additionally, Fourier transformed infrared spectroscopy (FTIR) measurements were applied to identify the presence of silicon based oils, lubricants or greases in components for the TRT gas system. Polymethylsiloxane was classified by this technique to be the main substance of the impurities.

The results of these analyses delivered the necessary information to obtain a rough model of the deposition mechanism and for developing procedures and methods for the prevention of wire aging.

Deposition Mechanism:

In the thin tube of plasma surrounding the anode wire, many complex physical and chemical phenomena are occurring simultaneously. The plasma chemical vapor deposition process involves the dissociation and/or chemical reaction of gaseous reactants

(organosilicon compounds) in the plasma environment, followed by the formation of a stable solid product. The deposition involves homogenous gas phase reactions, which occur in the gas phase, and/or heterogeneous chemical reactions that occur on/near the vicinity of the anode wire leading to the formation of SiO_x films. The creation of molecular fragments in the plasma is therefore a necessary precursor for wire aging whereby, next to heavy particle collisions or photon exposure, electron impact dissociation might be the dominating mechanism.

SiO_2 polymerization is a solely surface process. Heterogeneous reactions near the vicinity of the wire surface result in the adsorption of mobile atoms/monomers on the wire, which diffuse to the preferred sites to form germs and stable nuclei. Growth will occur by the addition of adsorbed monomers to sites with lowest free energy such as kinks and ledges to form crystallites. A thin crystal is formed upon coalescence. Heterogeneous reactions can lead to the formation of various structures, depending on precursor concentration and surface temperature, like epitaxial, polycrystalline, whiskers or amorphous. The deposit composition on the wire surface depends strongly on the O_2 content in the gas mixture, on the exposure time and on the current density. Higher O_2 concentrations, longer exposure times and higher current densities are leading to purer SiO_2 deposits. However, the surface reactions mechanisms forming the deposits are not fully understood.

Gas Purification:

There exist some different techniques (cryogenic distillation, catalytic conversion, adsorption on porous materials) of gas purification that can be employed for the removal of organosilicon compounds from the TRT gas system. The simplest and most appropriate has to be selected. Hence experiments have been performed to investigate the capability of the different gas purification principles.

From the results of these investigations, gas purification by adsorption on a porous material in a packed bed has been selected. It is the most suitable for the TRT gas system as the working temperature is ambient and no additional heat or power is required. The successful adsorption of organosilicon compounds from a carrier gas by an AERONEX standard filter, a self-made zeolite (type UY8) and TIMIS adsorber has been demonstrated. The adsorption capacity determined is $0.013 \text{ g}_{\text{HMDS}}/\text{g}_{\text{Adsorbent}}$ for the Aeronex filter, $0.074 \text{ g}_{\text{HMDS}}/\text{g}_{\text{Adsorbent}}$ for the zeolite adsorber and $0.026 \text{ g}_{\text{HMDS}}/\text{g}_{\text{Adsorbent}}$ for the TIMIS adsorber. According the guideline for packed bed dimensioning, about 2.6 kg zeolite material (type UY8) will be needed for a self-made purifier for the TRT active gas system. Taking into account a very conservative assumption for the impurity level of approximately 10 ppb the purifier will have a lifetime of 101 years with negligible adsorbent costs of 26 Eur. Although regeneration is possible it will most likely not be performed as the adsorption capacity is very high and the price of the material is very low.

Systematic Component Validation Procedure:

A complex issue for the safe operation of gaseous detectors is the cleanliness of the gas supply system. Therefore, components used to build the gas system have to be selected with care in order to avoid the pollution of an initially clean gas mixture. The TRT-consortium has consistently followed a strict validation policy for all components used in the gas system. A component is considered validated if, after performing an aging test

with TRT straws, no aging is detected during ~200 hours of irradiation at 10 times the nominal gas flow rate and at a current density of 100 nA/cm. This test guarantees that the gas gain drop will be less than 2-3 % per year. A gas gain drop of 2-3% per year of TRT operation is certainly not enough to ensure the required 10 years lifetime, but for the case that aging appears, the gas gain can be restored by operating the detector for a short period of time (~2 days/year) at LHC condition with the gas mixture Ar(70%)CO₂(26%)CF₄(4%). Tests have shown that two cleaning days per year with CF₄ can safely be performed.

Furthermore, a few useful guidelines for avoiding aging problems in wire chambers have been summarized.

Concentration Measurements:

In order to be able to perform quantitative concentration measurements and filter studies a constant impurity source with an adjustable impurity level was developed on the basis of a capillary system. This allows to produce gas mixtures with any demanded silicon concentration. Hexamethyldisiloxane (HMDS) has been found to be a good representative for the real impurities that might be expected in the TRT gas system. It is liquid and has a vapor pressure of about 100 mbar at 20°C. The capillary system is a low-cost alternative to mass flow metering systems and has the additional benefit of easy calibration to any required gas.

The concentrations measurements showed a linear relationship between aging rate and impurity concentration. Comparing the results from the concentration measurements with aging tests, it can be concluded that a component that is classified as medium polluted, by the aging test, will produce an impurity level of about 1 ppb. Furthermore, it can be assumed from the concentration measurements that the impurity level produced by a validated gas system component is below 0.1 ppb. This information is of fundamental importance for the dimensioning and maintenance of the filters.

9 Conclusions

Aging effects are largely due to wire deposits resulting from dissociation and deposition processes of organosilicone compounds in the thin tube of plasma surrounding the anode wire. The origin of the impurities are silicon based materials which can easily pollute an initially clean gas mixture through outgassing processes. The TRT has consistently followed a strict validation policy for all components used in the gas system. According to this policy, the impurity level in the active TRT gas system will be kept below 0.1 ppb. This does not eliminate wire aging completely but it minimizes the aging rate of the TRT to an level where the gas gain can be restored by flushing the detector with the gas mixture Ar(70%)CO₂(26%)CF₄(4%) during two days per year of LHC operation. Tests have shown that two cleaning days per year with CF₄ can safely be performed.

Through different analytical methods, polymethylsiloxane has been identified as the main substance of the aging causing impurities. Concentration measurements with a constant HMDS source demonstrated that a component that is classified as medium polluted, by an aging test, will produce an impurity level of about 1 ppb.

Considering that errors in the systematic component validation procedure and during the assembly of the TRT can occur, an absolutely clean gas system cannot be guaranteed. Therefore, a gas purification method has been developed on the principle of gas separation by adsorption processes in packed beds. The adsorption capacity of various materials has been investigated in breakthrough measurements. The highest determined adsorption capacity is 0.074 g_{HMDS}/g_{Adsorbent} for the zeolite material UY8 received from the company Bad Köstritz in Germany. According to the guideline for packed bed dimensioning, about 2.6 kg zeolite material will be needed for a self-made purifier for the purification of the TRT active gas system. Taking into account a very conservative assumption for the impurity level of approximately 10 ppb, the purifier will have a lifetime of 101 years with negligible adsorbent costs of 26 Eur. Regeneration is possible but it will most likely not be performed as the adsorption capacity is very high and the price of the material is very low.

Appendix A

Pressure Drop of Aeronex Standard Filters

Initially, the implementation of a purifier for the removal of organosilicon compounds was not foreseen in the design of the TRT gas system and its additional pressure drop could cause problems. To avoid changes of the instrumentation of the gas system the pressure drop of the purifier should be as low as possible (maximum 100 mbar). Below the pressure drop curves versus the gas flow rate of some Aeronex Standard Filters are illustrated. The purifier type CE-35KF-A-4R with a maximum flow rate of 1 slpm is shown in Figure 68, type CE-500KF-A-4R with a maximum flow rate of 60 slpm in Figure 69, type CE-2500KF-A-4R with a maximum flow rate of 300 slpm in Figure 70 and type CE-10MF-A-8Y with a maximum flow rate of 1000 slpm in Figure 71.

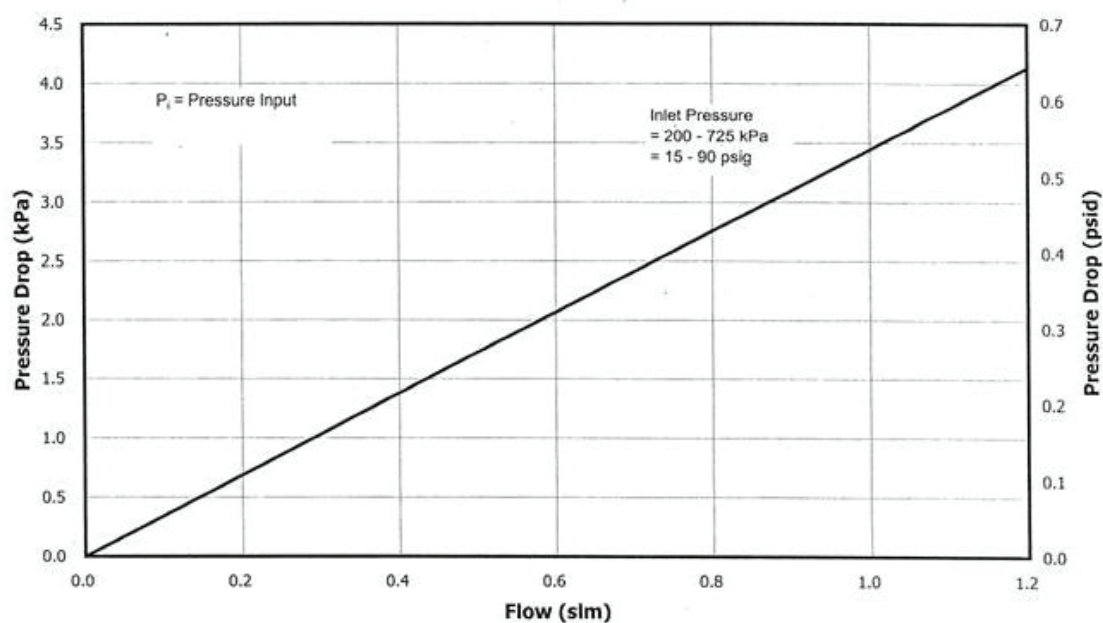


Figure 68: Press drop curve for the Aeronex Standard Filter type CE-35KF-A-4R with 1 slpm maximum flow rate [86]

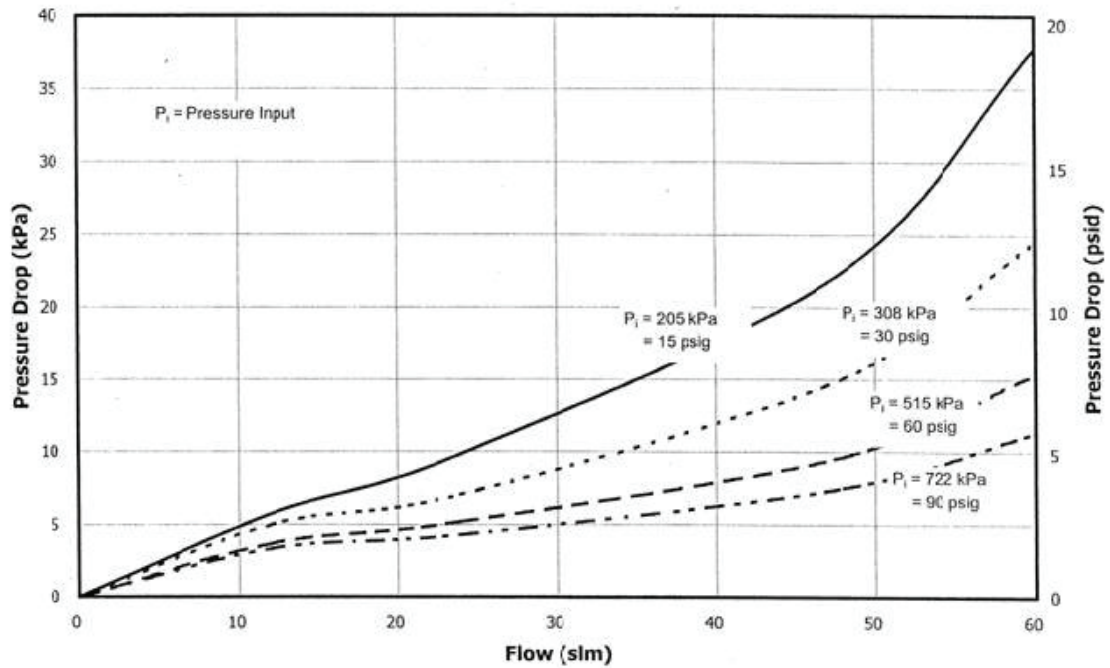


Figure 69: Press drop curve for the Aeronex Standard Filter type CE-500KF-A-4R with 60 slpm maximum flow rate [86]

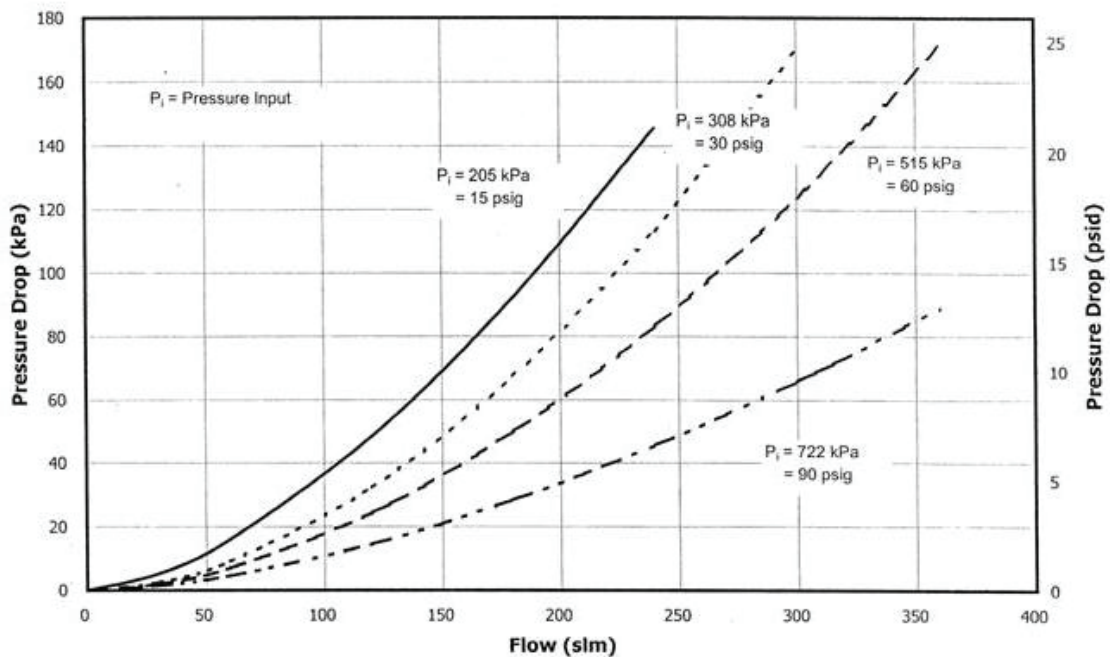


Figure 70: Press drop curve for the Aeronex Standard Filter type CE-2500KF-A-4R with 300 slpm maximum flow rate [86]

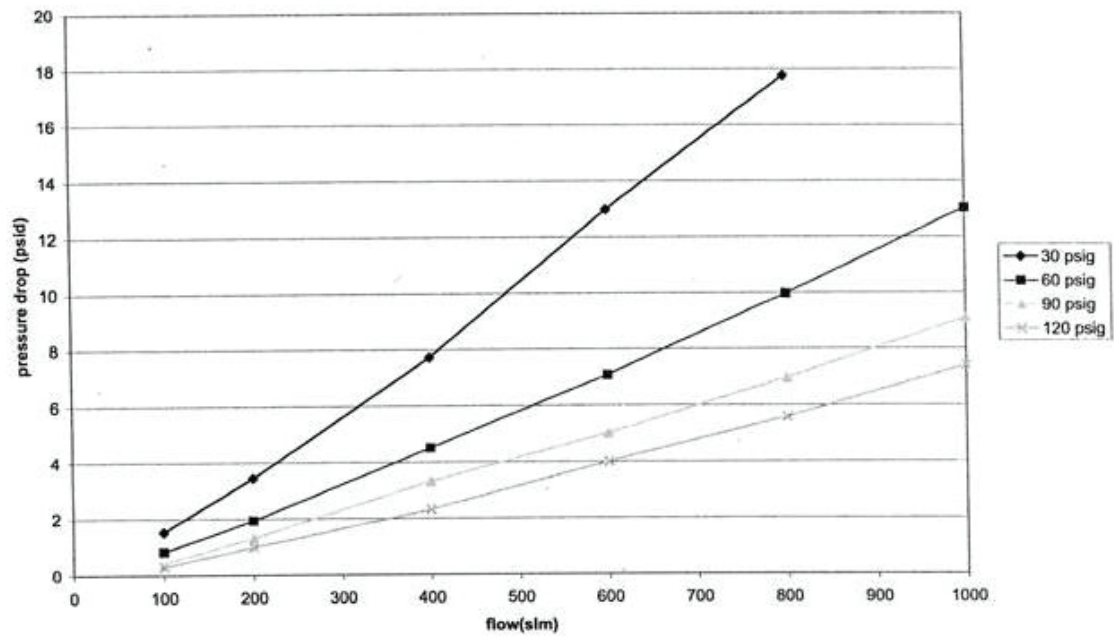


Figure 71: Press drop curve for the Aeronex Standard Filter type CE-10MF-A-8Y with 1000 slpm maximum flow rate [86]

Appendix B

Filter Assembly in the TRT active Gas System

Figure 72 shows a block diagram of the TRT gas system. A purifier with a volume of 10 liters consisting of 2 liters TIMIS catalyst and 8 liters charcoal is part of this system. Its original purpose was the neutralization of ozone by the TIMIS catalyst and the removal of radioactive substances with the charcoal. As demonstrated earlier the TIMIS catalyst has a relatively high adsorption capacity for organosilicon compounds. Taking into account a very conservative assumption for the impurity level in the TRT active gas system of approximately 10 ppb the 2 liter TIMIS catalyst will have a lifetime of approximately 20 years without regeneration. Also the charcoal will adsorb a certain amount of organosilicon compounds impurities the capacity is not known yet. Therefore the total lifetime of the purifier will be much higher than the 20 years for the TIMIS catalyst only. Figure 73 shows the piping and instrumentation diagram of the purification module. It consists of 2 columns to be able to perform regeneration without interrupting the main system. Regeneration has to be done with CO₂ at 230 °C with a gas flow of 40 l/h. The regeneration process needs approximately one day.

However any source of organosilicon impurities after the purifier will still cause aging in the TRT detector. Therefore the installation of zeolite purifiers behind the mixer module and in front of the UX distribution module are planned.

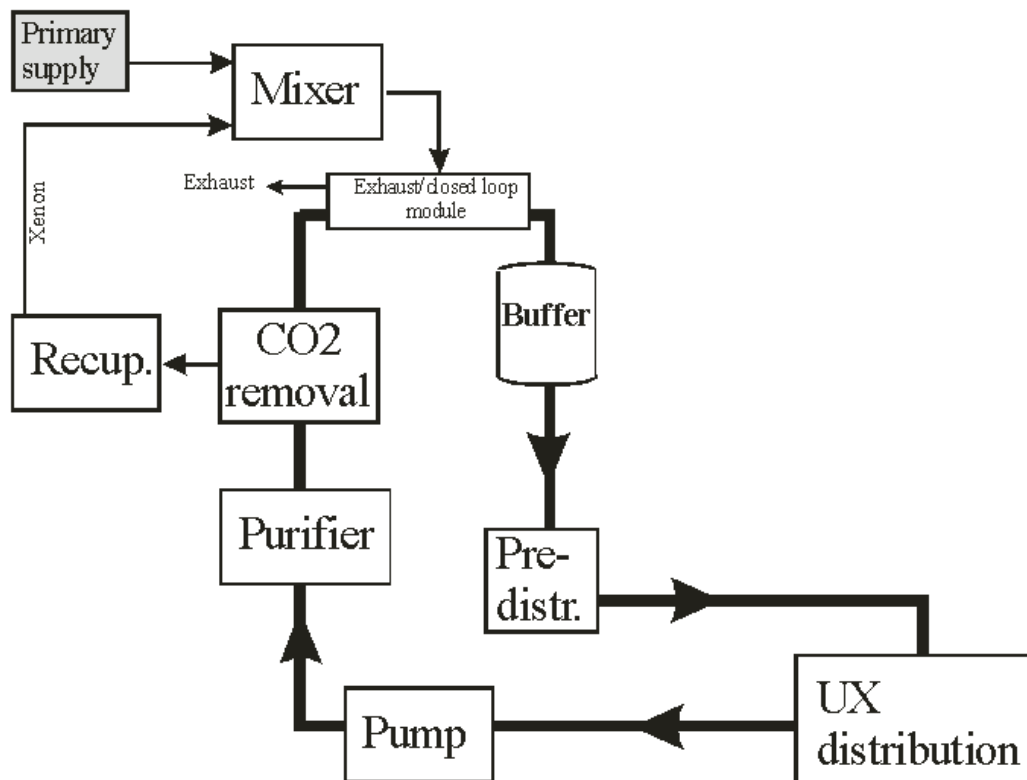


Figure 72: TRT active gas system overview [91]

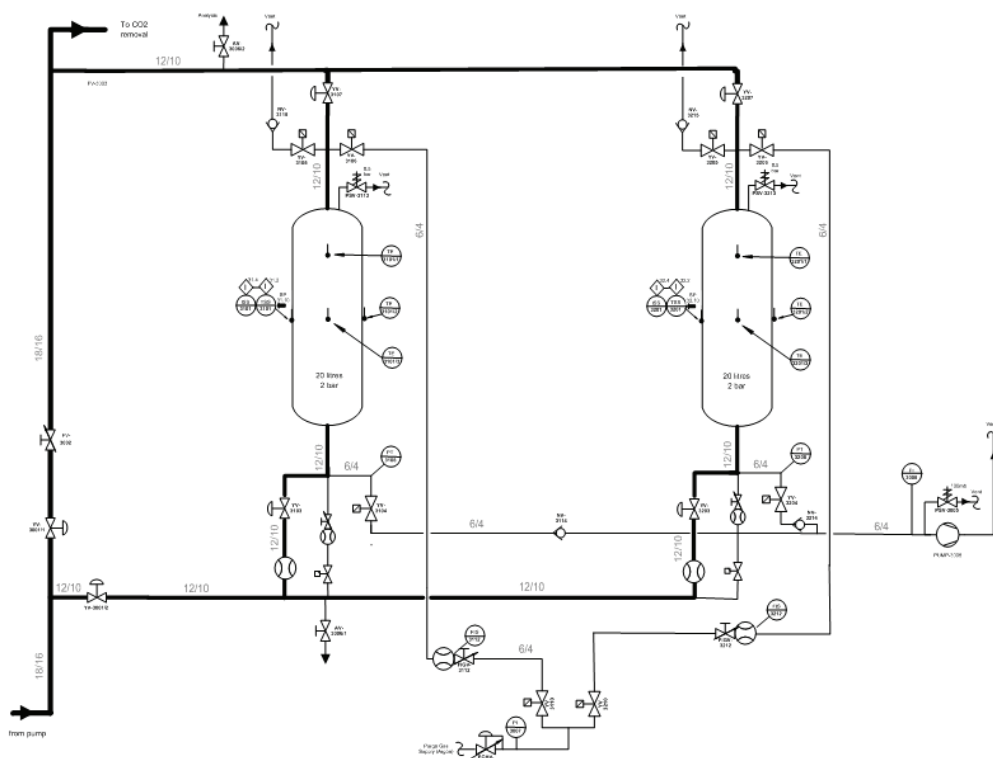


Figure 73: TRT active gas system – piping and instrumentation diagram of the purification module [91]

Appendix C

Aging Test Station

Figure 74 shows a typical straw prototype used for the aging tests. It consists of 3 TRT straws with a length of about 30 cm. The main gas flow entering the prototype is split in front of the straws in such a way that every straw has the same flow rate. Figure 75 illustrates the adjustment of the prototypes on the aging test station whereby 6 prototypes could be irradiated at the same time. This arrangement accelerated the systematic component validation procedure. Figure 76 presents an overview of the aging tests station. The gas supply for the individual prototypes can be seen on the left hand side of the picture and the X-ray tube on the right hand side. The pulse height measurements could be performed automatically and the results were read out with software written for the measurements.



Figure 74: Straw prototype with three TRT straws connected in parallel

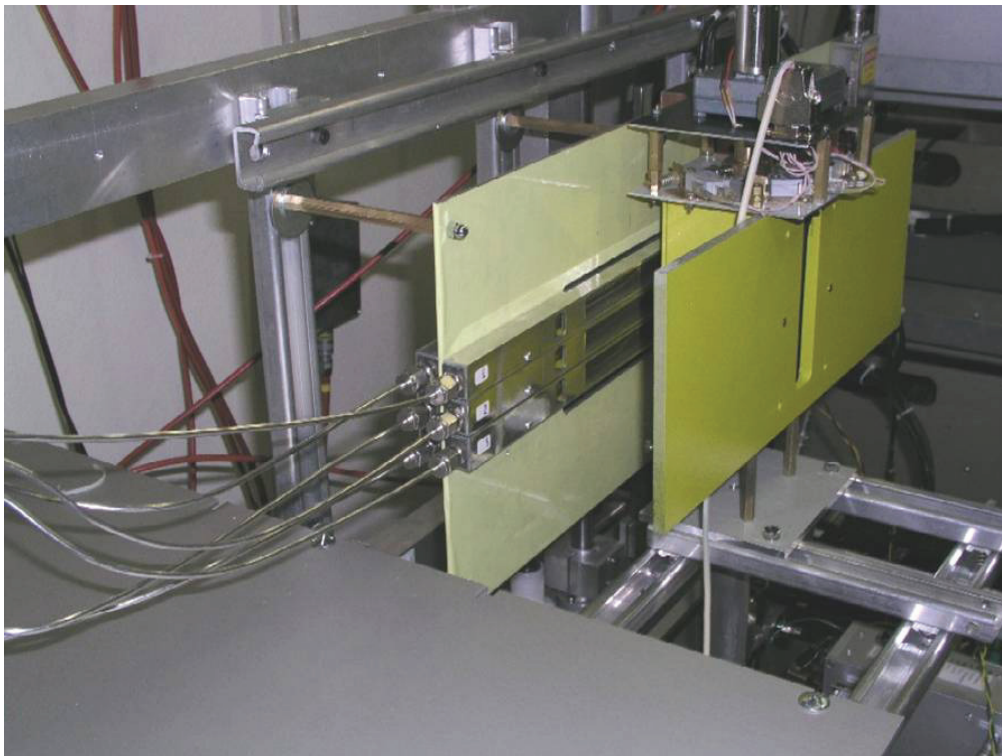


Figure 75: Straw prototype adjustment in the aging test station

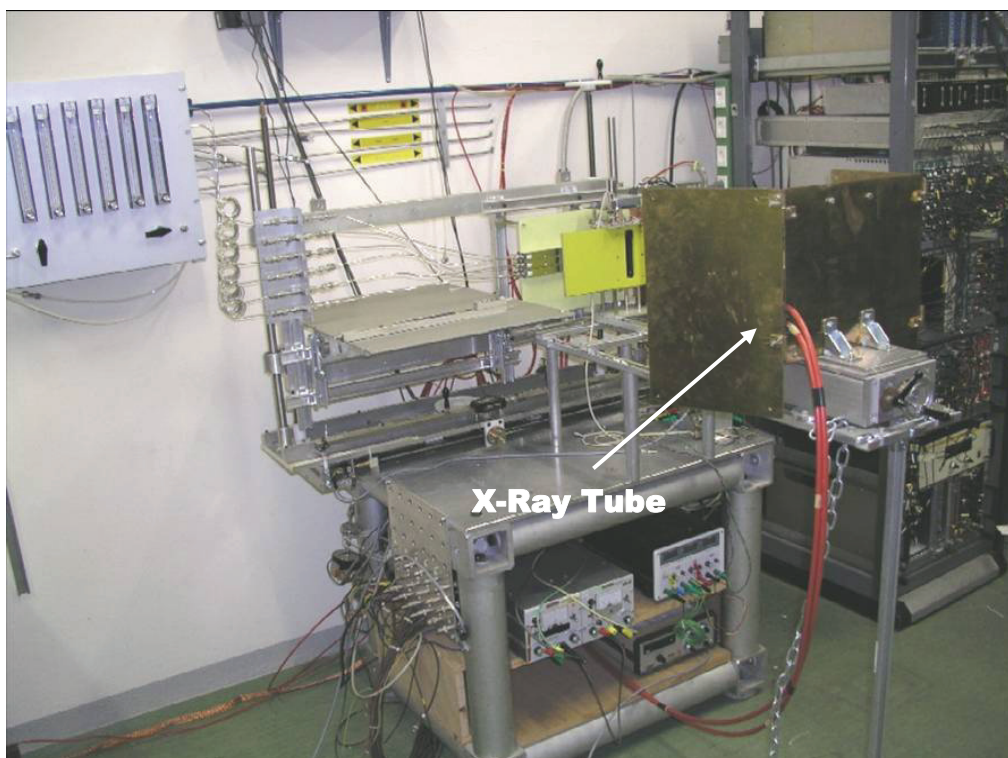


Figure 76: Aging Test Station

Bibliography

- [1] CERN, general information, <http://en.wikipedia.org/wiki/CERN>
- [2] CERN, accelerator complex, <http://public.web.cern.ch>
- [3] C. Williams, The ALICE TOF System, IV International Symposium on LHC Physics and Detectors, Fermilab, Batavia, 2003
- [4] M. Herrero, The Standard Model, Universidad Autonoma de Madrid - Departamento de Fisica Teorica, arXiv:hep-ph/9812242 v1 3, 1998
http://arxiv.org/PS_cache/hep-ph/pdf/9812/9812242.pdf
- [5] CMS Collaboration, Technical Design Report, CERN/LHCC/97-033, Geneva, 2000
- [6] ALICE Collaboration, Technical Design Report, CERN/LHCC/00-001, Geneva, 2000
- [7] TOTEM Collaboration, Technical Design Report, CERN/LHCC/04-002, Geneva, 2004
- [8] ATLAS Collaboration, Detector and Physics Design Report, CERN/LHCC/99-14, vol. 1, Geneva, 1999
- [9] ATLAS Collaboration, Detector and Physics Design Report, CERN/LHCC/99-15, vol. 2, Geneva, 1999
- [10] ATLAS Collaboration, Inner Detector Technical Design Report, CERN/LHCC 97-17, Geneva, 1997
- [11] T. Akesson et al., Status of design and construction of the TRT for the ATLAS experiment at the LHC, Nucl. Instr. and Meth A, vol. 522, pp. 131-145, 2004
- [12] V. Bondarenko et al., Kapton straw chambers for a transition radiation detector, Nucl. Instr. and Meth A, vol. 327, pp. 386-392, 1993
- [13] A. Romaniouk, Choice of materials for the construction of the transition radiation detector of ATLAS, ATLAS Internal Note, ATL-INDET-98-211, 1998
- [14] T. Akesson et al, Aging studies for the transition radiation tracker of ATLAS, Nucl. Instr. and Meth A, vol. 515, pp. 166-179, 2003
- [15] T. Akesson et al, Study of straw proportional tubes for a transition radiation tracker/detector at LHC, Nucl. Instr. and Meth A, vol. 361, pp. 440-456, 1995
- [16] ATLAS Collaboration, Specification for gold-plated tungsten wire, ATL-IT-ES-0012, Geneva, 2000
- [17] V. Razin, Self-Quenched Streamer Operating Mode for Gas Discharge Detectors, Instr. and Exp. Tech., vol. 44, pp. 425-443, 2001
- [18] T. Akesson et al, Operation of the ATLAS Transition Radiation Tracker under very high irradiation at the CERN LHC, Nucl. Instr. and Meth A, vol. 522, pp. 25-32, 2004
- [19] D. Clegg, Irradiation effects on polymers, Elsevier Applied Science, London, 1991
- [20] J. Wise, Chemistry of radiation damage to wire chambers, PhD Thesis, LBL-32500, UC-414, 1992

- [21] J. Va'vra, Review of wire-chamber ageing, Nucl. Instr. and Meth. A, vol. 252, pp. 547 – 563, 1986
- [22] J. A. Kadyak, Wire-chamber aging, Nucl. Instr. and Meth. A, vol. 300, pp. 436-451, 1991
- [23] ATLAS Collaboration, Inner Detector Technical Design Report, CERN/LHCC/97-17, vol. 2, Geneva, 1997
- [24] M. Capeans et al, Recent Aging Studies for the ATLAS Transition Radiation Tracker, TNS vol. 51, pp. 960-967, 2004
- [25] M. Capeans et al, Validation of the Wiring of Wheel 20ITJNRB000003 assembled at Dubna and the Validation of the Wiring of the 4-plane Wheel 20ITPNPA000006 assembled at PNPI, CERN ATL-IT-QC-0023, Geneva, 2003
- [26] P. Cwetanski, Acceptance Tests of the ATLAS Transition Radiation Tracker End-cap Wheels, Ph.D. Dissertation, University of Helsinki, 2006
- [27] A. Romaniouk, Specification for the TRT gas system component validation, ATLAS Internal Note, Active Gas FDR, CERN, Geneva, 2003
- [28] DESY, 2nd Aging Workshop, Hamburg, 2001
<http://www.desy.de/agingworkshop/>
- [29] L. Malter, Thin film field emission, Phys. Rev., vol. 50, pp. 48 - 58, 1936
- [30] M. Capeans et al, Aging and materials: Lessons for detectors and gas systems, Nucl. Instr. Meth. A, vol. 515, pp. 73-88, 2003
- [31] H. Wiedemann, Particle Accelerator Physics 1, Springer-Verlag Berlin, 2nd Edition, 2003
- [32] M. Deile et al, Tests of a Roman Pot Prototype for the TOTEM Experiment, arXiv:physics/0507080 v1, 2005
http://arxiv.org/PS_cache/physics/pdf/0507/0507080.pdf
- [33] M. Deile et al, Diffraction and Total Cross-Section at the Tevatron and the LHC, arXiv:hep-ex/0602021 v1, 2006
- [34] C. Grupen, Particle Detectors, Cambridge University Press, 1996
- [35] K. Kleinknecht, Detectors for Particle Radiation, Cambridge University Press, 2nd Edition, 1998
- [36] G. Knoll, Radiation Detection and Measurement, University of Michigan, 2nd Edition, 1989
- [37] F. Sauli, Drift and Diffusion of Electrons in Gases: A Compilation, CERN 84-08, Geneva, 1984
<http://doc.cern.ch/yellowrep/1984/1984-008/fulltext.pdf>
- [38] L. Ropelewski, Particle Detectors – Principles and Techniques, CERN Academic Training Program, BUL-TD-2005-079, Lecture 2, Geneva, 2005
http://cern.ch/ph-dep-dt2/lectures_PD_2005.htm
- [39] A. Von Engel, Handbuch der Physik, Springer-Verlag, Vol. 21, Berlin, 1956
- [40] R. Haubner, Chemical and Physical Vapor Deposition in der Technologie, Technische Universitaet Wien - Institut für Chemische Technologien und Analytik, Skriptum, 2004
- [41] W. Walter, Lehrbuch der Organischen Chemie, S. Hirzel Verlag Stuttgart, 21. Auflage, 1988
- [42] VDI – Wärmetlas, Springer Verlag Berlin, 8. Auflage, 1997

- [43] D. Hess, Plasma Chemistry in Wire Coating, University of California, Proceedings of Workshop on Radiation Damage to Wire Chambers, LBL-21170, pp. 15-23, 1986
- [44] N. Maeda et al, Dissociation processes in plasma enhanced chemical vapor deposition of SiO₂ films using tetraethoxysilane, American Vacuum Society, J. Vac. Sci. Technol. A 16(6-7)), 1998
- [45] T. Matsutani et al, Deposition of SiO₂ films by low-energy ion-beam induced chemical vapor deposition using hexamethyldisiloxane, Elsevier, Surface and Coatings Technology 177-178, pp. 365-368, 2004
- [46] R. Fisher et al, Deposition of SiO₂ films from novel alkoxyasilane/O₂ plasmas, American Vacuum Society, J. Vac. Sci. Technol. A 16(6-10), 1998
- [47] F. Leu et al, Diagnostics of a hexamethyldisiloxane/oxygen deposition plasma, Elsevier, Surface and Coatings Technology 174-175, pp. 928-932, 2003
- [48] M. Van de Sanden et al, Argon-oxygen plasma treatment of deposited organosilicon thin films, Elsevier, Thin Solid Films 449, pp. 40-51, 2004
- [49] NIST Chemistry Webbook, <http://webbook.nist.gov>
- [50] B. Cornils, Catalysis from A to Z, Wiley – VCH, Weinheim, 2003
- [51] R. Wijngaarden, Industrial Catalysis, Wiley – VCH, Weinheim, 1998
- [52] I. Chorkendorff, Concepts of Modern Catalysis and Kinetics, Wiley – VCH, Weinheim, 2003
- [53] A. Kohl, Gas Purification, McGraw-Hill Book Company, London, 1960
- [54] S. Gregg, Adsorption, Surface Area and Porosity, 2nd Edition, Academic Press, London, 1982
- [55] S. Brunauer et al, Adsorption of Gases in Multimolecular Layers, J. Am. Chem. Soc., vol. 60, pp. 309-319, 1938
- [56] G. Staudinger, Mechanische Verfahrenstechnik 1, Technische Universität Graz - Institut für Verfahrenstechnik, Skript, 1999
- [57] D. Ruthven, Principles of Adsorption and Adsorption Processes, Wiley – Interscience, New York, 1982
- [58] W. Kast, Adsorption aus der Gasphase, VCH Verlagsgesellschaft, Weinheim, 1988
- [59] A. Gupte, Die Struktur von Packungen aus Kugeln: Zufallskriterien und Testmethoden im Hinblick auf die Porenströmung, Chem. Ing. Tech., vol. 43, pp. 754-761, 1971
- [60] W. Kast, Principles of Pressure Drop in Randomly Packed Columns, Chem. Ing. Tech., vol. 36, pp. 464-468, 1964
- [61] Database of Zeolite Structures, <http://topaz.ethz.ch/IZA-SC/Introduction.htm>
- [62] Adsorption Isotherms, http://en.wikipedia.org/wiki/Adsorption#BET_Isotherm
- [63] W. Lindinger et al, Analysis of trace gases at ppb levels by proton transfer reaction mass spectrometry (PTR-MS), Plasma Sources Sci. Technol., vol. 6, pp. 111-117, 1997
- [64] W. Lindinger et al, Proton-transfer-reaction mass spectrometry (PTR-MS): online monitoring of volatile organic compounds at volume mixing ratios of a few pptv, Plasma Sources Sci. Technol., vol. 8, pp. 332-336, 1999

- [65] J. de Gouw et al, Sensitivity and specificity of atmospheric trace gas detection by proton-transfer-reaction mass spectrometry, *International Journal of Mass Spectrometry* 223-224, pp. 365-382, 2003
- [66] T. Karl et al, Trace gas monitoring at the Mauna Loa Baseline Observatory using Proton-Transfer-Reaction Mass Spectrometry, *International Journal of Mass Spectrometry* 223-224, pp. 527-538, 2003
- [67] A. Hansel et al, Improved detection limit of the Proton-Transfer-Reaction Mass-Spectrometry (PTR-MS): On-line monitoring of volatile organic compounds at mixing ratios of 10 pptv, *Rapid Communications in Mass-Spectrometry* 12, pp. 871-875, 1998
- [68] A. Hansel, Private Communication, University of Innsbruck - Institut für Ionenphysik, Technikerstrasse 25, 6020 Innsbruck
- [69] S. Ilie et al, Infrared Spectroscopy, CERN Technical Document, EDMS number: 410981, Geneva, 2005
<http://edms.cern.ch/file/394490/1/InfraredSpectroscopy.pdf>
- [70] C. Soares et al, Identification of Oils and Greases on Metallic Surfaces using FTIR; CERN Technical Document, EDMS number: 410969, Geneva, 2004
<http://edms.cern.ch/file/410969/1/oilsandgreases.pdf>
- [71] S. Ilie et al, Analyse de l'état de propreté des tubes en acier inoxydable par spectrophotométrie UV-Vis, CERN Technical Document, EDMS number: 410984, Geneva, 2003
<http://edms.cern.ch/file/410984/1/siliconeuvvis.pdf>
- [72] CERN Chemical Laboratory, Technical Document, N° MME-CEM : X-14/02.04, Geneva, 2004
- [73] CERN Chemical Laboratory, Technical Document, N° MME-CEM : X-09/02.04, Geneva, 2004
- [74] F. Settle et al, *Handbook of Instrumental Techniques for Analytical Chemistry*, New Jersey, 1997
- [75] S. Ilie, Private Communication, CERN Chemical Laboratory, Geneva, 2006
Sorin.Ilie@cern.ch
- [76] L. Smith et al, Infrared Spectra-Structure Correlations for Organosilicon Compounds, *Spectrochim. Acta*, vol. 16, pp. 87-105, 1960
- [77] L. Smith et al, Correlations of the SiH Stretching Frequency with Molecular Structure, *Spectrochim. Acta*, vol. 15, pp. 412-420, 1959
- [78] N. Kniseley et al, Observations on the Silicon-Hydrogen Vibrational Bands in Alkyl and Aryl Substituted Silanes, *Spectrochim. Acta*, vol. 15, pp. 651-655, 1959
- [79] N. Wright et al, Organosilicon Polymers. III. Infrared Spectra of the Methylpolysiloxanes, *J. Amer. Chem. Soc.*, vol. 69, pp. 803-809, 1947
- [80] R. Wilson et al, Preparation, Properties, and Infrared Spectra of 2,6-Disubstituted Phenoxysilanes, *J. Org. Chem.*, vol. 24, pp. 1717-1719, 1959
- [81] W. Young et al, Organosilicon Polymers. IV. Infrared Studies on Cyclic Disubstituted Siloxanes, *J. Amer. Chem. Soc.*, vol. 70, pp. 3758-3764, 1948
- [82] L. Smith et al, The Infrared Spectra of the Methyl Chlorosilanes, *J. Chem. Phys.*, vol. 21, pp. 1997-2004, 1953

- [83] R. Fessenden et al, The Infrared Spectra of Some Silazanes and Disilazanes, *J. Org. Chem.*, vol. 25, pp. 2191-2193, 1960
- [84] J. Lafferty, *Foundations of vacuum science and technology*, Wiley, New York, 1998
- [85] F. Sharipov et al, Gaseous mixture flow through a long tube at arbitrary Knudsen numbers, *American Vacuum Society, J. Vac. Sci. Technol. A* 20(3), 2002
- [86] Winder Technologies GmbH, Werbhollenstrasse 54, 4143 Dornbach, Switzerland
Peter.Winder@t-online.de
- [87] C. Meininhaus, *Hydrophobe Zeolithe zur selektiven Sorption von flüchtigen organischen Lösungsmitteldämpfen*, ETH – Zürich, Dissertation, 1998
- [88] ZEOCHEM AG, Seestrasse 108, 8707 Uetikon, Switzerland
Vonholzen.Werner@zeochem.ch
- [89] Chemiewerk Bad Köstritz GmbH, Heinrichshall 2, 07586 Bad Köstritz, Germany
A.Brandt@cwk-bk.de
- [90] Moscow State University - Faculty of Physics, Leninskie Gory, 119992 Moscow, Russia
Viktor.Kamarenko@cern.ch
- [91] S. Haider, ATLAS TRT Active Gas FDR, Presentation, CERN, Geneva, 2003

Nomenclature

Abbreviations

ALICE	A Large Ion Collider Experiment
ALPO	ALuminoPhOsphates
ATLAS	A Toroidal LHC ApparatuS
BET	Brunauer Emmet Teller
CDA	Carbon Dynamic Airbox
CERN	Conseil Européen pour la Recherche Nucléaire
CMS	Compact Muon Solenoid
CP	Charge-conjugation Parity
DC	Direct Current
DESY	Deutsche Elektronen –Synchrotron
DTGS	Deuterated TriGlycine Sulphate
EDX	Energy Dispersive X-ray
FTIR	Fourier Transformed Infrared Spectroscopy
HMDS	HexaMethylDiSiloxane
IR	InfraRed
ISOLDE	Isotope Sepaerator OnLine Device
LBL	Lawrence Berkeley Laboratory
LEP	Large Electron Positron collider
LHC	Large Hadron Collider
LHCb	Large Hadron Collider beauty
LINAC	LINear ACcelerator
MCT	Mercury Cadmium Telluride
MEK	MethylEthylKeton
MeOH	MethanOL
MTZ	Mass Transfer Zone
MWPC	Multi Wire Proportional Chamber
PD	Pixel Detector
PDMS	PolyDiMethylSiloxane
PECVD	Plasma Enhanced Chemical Vapor Deposition
PEEK	PolyEther Ether Keton
PEI	PolyEtherImide
PMDS	PentaMethylDiSiloxane
PS	Proton Synchrotron
PSB	Proton Synchrotron Booster
PTR-MS	Proton Transfer Reaction Mass Spectrometer
PVC	PolyVinylChloride
QGP	Quark Gluon Plasma
R	Reactant (organic)
RICH	Ring-Imaging CHerenkov detector

RP	Roman Pots
SCT	SemiConductor Tracker
SEM	Scanning Electron Microscope
SPS	Super Proton Synchrotron
SQS	Self-quenched streamer
SWPC	Single Wire Proportional Chamber
TMP	TetraMethylPentane
TMS	TriMethylSilane
TOTEM	TOTal and Elastic Measurement experiment
TRT	Transition Radiation Tracker
UA	Underground Area
UV	Ultra Violet
UX	Underground eXperimantal area
VOC	Volatile Organic Compound

Curriculum Vitae

Name: Gerald Sprachmann
 Date of Birth: 1st December 1974
 Nationality: Austria
 Address: Diex 152
 9103 Diex
 Austria
 Phone Private: +43 4231 8335
 Phone Private: +41 792460143
 Phone Work: +41 227671412
 Email: Gerald.Sprachmann@cern.ch

Education:

- 2003 – 2006: PhD at CERN within the “Austrian Doctoral Student Program” supervised by the University of Technology Vienna (Institut für Allgemeine Physik)
subject: “Aging and Gas Filtration Studies in the ATLAS Transition Radiation Tracker at CERN”
related research fields: gas purification, adsorption processes, porous materials, fixed bed reactors, plasma chemistry, gas analysis
- 2002 – 2003: Diploma thesis for the company “Austrian Energy & Environment” (AE&E) in cooperation with the University of Technology Graz
subject: “Dry Flue Gas Purification with Circulating Fluidized Bed Reactors”
related research fields: gas purification, adsorption processes, separation processes, mass transfer, fluidized bed reactors, solid waste management
- 1996 – 2003: Graz University of Technology
degree: Chemical Engineering
specialisation: Environmental Engineering (air pollution control)
- 1990 – 1995: Higher Technical College for Electronics in Klagenfurt
specialisation:
 - Electronic and Data Processing
 - High Frequency and Impulse Technology

Professional Experience:

- 2003 – 2006: PhD fellow at CERN, Geneva
The area of responsibility was the performance of the systematic validation of gas system components, the development of adsorption tests, filter development and assembling and the operation and maintenance of the laboratory.
- 2002 – 2003: Austrian Energy & Environment, Vienna
Maintenance of the pilot dry gas cleaning system for the removal of SO₂, HCl, HF, heavy metals, dioxins, furans and dust in the flue gas of an incineration plant in Vienna.
- 2001: Austrian Energy & Environment, Graz (part time)
Search for possible applications for fly ash as a resource material in the construction industry. Fundamental analysis of fly ash properties has been performed and possible uses have been outlined.
- 2000: Kretz – Technik, Zipf (three month)
Analysis of the power emissions of ultra sound instruments used in medicine. For human safety reasons the spatial power intensity profile produced by the ultra sound instrument has to be determined.
- 1999: AVL-List, Graz (four month)
Improvement of the precision of “Smoke Meters” used to measure the soot content in exhaust fumes. Therefore a systematic analysis of filter paper properties was performed and recommendations for filter paper manufactures have been summarized.

Languages:

German: mother tongue
English: bilingual
French: conversational
Spanish: basics

Language Courses:

- five French courses at CERN (CH)
- Czech course, four weeks, University of Pilsen (CZ)
- Portuguese course, five weeks, University of Coimbra (P)
- English course, five weeks, St. Kerians College in Kilkenny (IR)

Special Courses:

- Studied at the University of Strathclyde in Glasgow during the academic year 2001/2002. (Department of Chemical Engineering)
- Course for “Cross-Cultural Management” in China; University of Beijing and Fudan University in Shanghai

Conferences:

2005: Nuclear Science Symposium & Medical Imaging Conference
topic of presentation: “Aging Effects in Straw Proportional Chambers and Gas Filtration Studies”, Oct. 2005, San Juan (Puerto Rico)

Publications:

1. G. Sprachmann et al, *Aging Effects in Straw Proportional Chambers and Gas Filtration Studies*, Transaction on Nuclear Science, 2006
2. P. Cwetanski et al, *Acceptance Tests and Criteria of the ATLAS Transition Radiation Tracker*, Transaction on Nuclear Science, vol. 52, pp. 2911-2916, 2005
3. M. Capeans et al, *Recent Aging Studies for the ATLAS Transition Radiation Tracker*, Transaction on Nuclear Science, vol. 51, pp. 960-967, 2004
4. G. Sprachmann, *Parameterstudie an der TURBOSORP[®] Pilotanlage zur trockenen Rauchgasreinigung nach Muellverbrennungen*, Diploma Thesis, University of Technology Graz, 2003